



저작자표시-비영리-변경금지 2.0 대한민국

이용자는 아래의 조건을 따르는 경우에 한하여 자유롭게

- 이 저작물을 복제, 배포, 전송, 전시, 공연 및 방송할 수 있습니다.

다음과 같은 조건을 따라야 합니다:



저작자표시. 귀하는 원저작자를 표시하여야 합니다.



비영리. 귀하는 이 저작물을 영리 목적으로 이용할 수 없습니다.



변경금지. 귀하는 이 저작물을 개작, 변형 또는 가공할 수 없습니다.

- 귀하는, 이 저작물의 재이용이나 배포의 경우, 이 저작물에 적용된 이용허락조건을 명확하게 나타내어야 합니다.
- 저작권자로부터 별도의 허가를 받으면 이러한 조건들은 적용되지 않습니다.

저작권법에 따른 이용자의 권리는 위의 내용에 의하여 영향을 받지 않습니다.

이것은 [이용허락규약\(Legal Code\)](#)을 이해하기 쉽게 요약한 것입니다.

[Disclaimer](#)

Ph.D. Dissertation of Engineering

Continuous observation of
vegetation phenology and solar-
induced chlorophyll fluorescence
using near-surface remote
sensing systems

근접 표면 원격 센싱 시스템들을 이용한 지속적
식물 계절 및 태양 유도 엽록소 형광물질 관측

December 2021

Graduate School of Seoul National University
Interdisciplinary Program in
Landscape Architecture

Jongmin Kim

Continuous observation of vegetation phenology and solar- induced chlorophyll fluorescence using near-surface remote sensing systems

Advisor: Youngryel Ryu

A dissertation submitted in partial fulfillment of
the requirements for the Degree of Doctor of
Philosophy in Interdisciplinary Program in
Landscape Architecture in
Seoul National University

December 2021

Jongmin Kim

Approved by Thesis Committee

Chair	_____	(Seal)
Vice Chair	_____	(Seal)
Examiner	_____	(Seal)
Examiner	_____	(Seal)
Examiner	_____	(Seal)

Abstract

Continuous observation of vegetation phenology and solar–induced chlorophyll fluorescence using near–surface remote sensing systems

Jongmin Kim

Interdisciplinary Program in Landscape Architecture in

Seoul National University

Graduate School of Seoul National University

Supervised by Professor Youngryel Ryu

Monitoring phenology, physiological and structural changes in vegetation is essential to understanding feedbacks of vegetation between terrestrial ecosystems and the atmosphere by influencing the albedo, carbon flux, water flux and energy. To this end, normalized difference vegetation index (NDVI) and solar induced chlorophyll fluorescence (SIF) from satellite remote sensing have been widely used. However, there are still limitations in satellite remote sensing as 1) satellite imagery could not capture fine scale spatial resolution of SIF signals, 2) satellite products are strongly influenced by condition of atmosphere (e.g. clouds), thus it is challenge to know physiological and structural changes in vegetation on cloudy days and 3) satellite imagery captured a mixed signal from over– and understory, thus it is difficult to study the difference between overstory and understory phenology separately. Therefore, in order to more accurately understand the signals observed from the satellite, further studies using near–surface remote sensing system to collect ground–based observed data are needed.

The main purpose of this dissertation is continuous

observation of vegetation phenology and SIF using near-surface remote sensing system. To achieve the main goal, I set three chapters as 1) developing low-cost filter-based near-surface remote sensing system to monitor SIF continuously, 2) monitoring SIF in a temperate evergreen needleleaf forest continuously, and 3) understanding the relationships between phenology from in-situ multi-layer canopies and satellite products.

In **Chapter 2**, I developed the filter-based smart surface sensing system (4S-SIF) to overcome technical challenges of monitoring SIF in the field as well as to decrease sensor cost for more comprehensive spatial sampling. I verified the satisfactory spectral performance of the band pass filters and confirmed that digital numbers (DN) from 4S-SIF exhibited linear relationships with the DN from the hyperspectral spectroradiometer in each band ($R^2 > 0.99$). In addition, we confirmed that 4S-SIF shows relatively low variation of dark current value at various temperatures. Furthermore, the SIF signal from 4S-SIF represents a strong linear relationship with QEpro-SIF either changing the physiological mechanisms of the plant using DCMU (3-(3,4-dichlorophenyl)-1,1-dimethylurea) treatment. I believe that 4S-SIF will be a useful tool for collecting in-situ data across multiple spatial and temporal scales.

Satellite-based SIF provides us with new opportunities to understand the physiological and structural dynamics of vegetation from canopy to global scales. However, the relationships between SIF and gross primary productivity (GPP) are not fully understood, which is mainly due to the challenges of decoupling structural and physiological factors that control the relationships. In **Chapter 3**, I reported the results of continuous observations of canopy-level SIF, GPP, absorbed photosynthetically active radiation (APAR), and

chlorophyll: carotenoid index (CCI) in a temperate evergreen needleleaf forest. To understand the mechanisms underlying the relationship between GPP and SIF, I investigated the relationships of light use efficiency (LUE_p), chlorophyll fluorescence yield (Φ_F), and the fraction of emitted SIF photons escaping from the canopy (f_{esc}) separately. I found a strongly non-linear relationship between GPP and SIF at diurnal and seasonal time scales ($R^2 = 0.91$ with a hyperbolic regression function, daily). GPP saturated with APAR, while SIF did not. In addition, there were differential responses of LUE_p and Φ_F to air temperature. While LUE_p reached saturation at high air temperatures, Φ_F did not saturate. I also found that the canopy-level chlorophyll: carotenoid index was strongly correlated to canopy-level Φ_F ($R^2 = 0.84$) implying that Φ_F could be more closely related to pigment pool changes rather than LUE_p . In addition, I found that the f_{esc} contributed to a stronger SIF-GPP relationship by partially capturing the response of LUE_p to diffuse light. These findings can help refine physiological and structural links between canopy-level SIF and GPP in evergreen needleleaf forest.

We do not fully understand what satellite NDVI derived leaf-out and full leaf dates actually observes because deciduous broadleaf forest consists of multi-layer canopies typically and mixed signal from multi-layer canopies could affect satellite observation. Ultimately, we have the following question: What phenology do we actually see from space compared to ground observations on multi-layer canopy phenology? In **Chapter 4**, I reported the results of 8 years of continuous observations of multi-layer phenology and climate variables in a deciduous broadleaf forest, South Korea. Multi-channel spectrometers installed above and below overstory

canopy allowed us to monitor over- and understory canopy phenology separately, continuously. I evaluated the widely used phenology detection methods, curvature change rate and threshold with NDVI observed above top of the canopy and compared leaf-out and full leaf dates from both methods to in-situ observed multi-layer phenology. First, I found that NDVI from the above canopy had a strong linear relationship with satellites NDVI ($R^2=0.95$ for MODIS products and $R^2= 0.85$ for Landsat8). Second, leaf-out dates extracted by the curvature change rate method and 10% threshold were well matched with understory leaf-out dates. Third, the full-leaf dates extracted by the curvature change rate method and 90% threshold were similar to overstory full-leaf dates. Furthermore, I found that overstory leaf-out dates were closely correlated to accumulated growing degree days (AGDD) while understory leaf-out dates were related to AGDD and also sensitive to the number of chill days (NCD). These results suggest that satellite-based leaf-out and full leaf dates represent understory and overstory signals in the deciduous forest site, which requires caution when using satellite based phenology data into future prediction as overstory and understory canopy show different sensitivities to AGDD and NCD.

Keyword: phenology, normalized difference vegetation index (NDVI), gross primary productivity (GPP), solar induced chlorophyll fluorescence (SIF), near-surface remote sensing, satellite, multi-layer canopy, canopy structure, canopy function

Student Number : 2017-39375

Table of Contents

Abstract	i
Table of Contents.....	v
Chapter 1. Introduction.....	2
1. Background.....	2
2. Purpose	5
Chapter 2. Monitoring sun-induced chlorophyll fluorescence using a filter-based near-surface remote sensing system	9
1. Introduction.....	9
2. Instrument design and technical specifications of the filter-based smart surface sensing system (4S-SIF)	12
2.1 Ultra-narrow band pass filter	14
2.2 Calibration of 4S-SIF.....	15
2.3 Temperature response of 4S-SIF	16
2.4 Evaluate SIF quality from installed 4S-SIF sensor in the field	17
3. Results.....	19
4. Discussion	22
Chapter 3. Solar-induced chlorophyll fluorescence is non-linearly related to canopy photosynthesis in a temperate evergreen needleleaf forest during fall transition.....	27
1 Introduction.....	27
2 Materials and Methods	31
2.1 <i>Study site</i>	31
2.2 <i>Leaf-level fluorescence measurement</i>	32
2.3 <i>Canopy-level SIF and spectral reflectance measurements</i>	34
2.4 <i>SIF retrieval</i>	37
2.5 <i>Canopy-level photosynthesis estimates</i>	38
2.6 <i>Meteorological variables and APAR</i>	39

2.7	<i>Statistical analysis</i>	4 0
3	Results.....	4 1
4	Discussion	4 8
4.1	<i>Non-linear relationships between SIF and GPP....</i>	4 9
4.2	<i>Role of fesc in the SIF-GPP relationship.....</i>	5 3
4.3	<i>Implications of non-linear SIF-GPP relationships in temperate ENF.....</i>	5 4
5.	Conclusion	5 7
Chapter 4. Monitoring spring phenology of a multi-layer canopy in a deciduous broadleaf forest: What signal do satellites actually see? 6		
5		
1	Introduction.....	6 5
2	Materials and Methods	6 9
2.1	Study site	6 9
2.2	Multi-layer spectral reflectance and transmittance measurement.....	6 9
2.3	Phenometrics detection.....	7 2
2.4	In-situ multi-layer phenology	7 3
2.5	Satellite remote sensing data.....	7 5
2.6	Meteorological variables	7 5
3	Results.....	7 6
4	Discussion	8 2
4.1	<i>How do satellite-based leaf-out and full-leaf dates differ from in-situ multi-layer phenology?.....</i>	8 3
4.2	<i>Are the 10 % and 90 % thresholds from satellite-based NDVI always well matched with the leaf-out and full-leaf dates calculated by the curvature change rate?.....</i>	8 6
4.3	<i>What are the implications of the difference between satellite-based and multi-layer phenology?.....</i>	8 7

4.4	<i>Limitations and Implications for future studies.....</i>	8 9
Conclusion		9 1
Appendix A.	Image-based multi-layer phenology monitoring..	9 3
Appendix B.	Simulation of spring phenology detection	9 4
Appendix C.	Comparison between leaf-out dates from MODIS NDVI and LED NDVI.....	9 5
Chapter 5.	Conclusion.....	1 1 5
Abstract in Korean.....		1 1 6

List of Figures

Figure 1) Image of 4S–SIF instrument complete with diffuser, ultra–narrow band pass filter, collimating lens and silicon photodiode.....	1 4
Figure 2) Evaluation of photodiodes at each band against a QEpro spectroradiometer across a wide range of solar radiation condition on 9 days.....	1 5
Figure 3) Dark current from 4S–SIF under various temperature. 4S–SIF showed consistent dark current value at various temperature and relative humidity.	1 7
Figure 4) Daily variation of PAR and observed SIF using QEpro and 4S–SIF during rooftop experiment. PAR was relatively consistent, but SIF was changed after DCMU and harvest.....	2 0
Figure 5) Daily variation of SIF yield and NDVI. SIF yield observed by 4S–SIF and QEpro showed clear change after DCMU treatment. On the other hands, NDVI was consistent around 0.6. Error bars indicate 95% CI.....	2 1
Figure 6) Scatter plots between 10–minute interval 4S–Sif and QEpro SIF. R ² and rRMSE represent toe coefficient of determination and the relative RMSE (RMSE/mean) of fitted linear regressions, respectively.	2 2
Figure 7) Seasonal variation in field–measured GPP, SIF, APAR and air temperature values (a–d), and LUEP , ΦF , fesc and CCI (e–h). For GPP, SIF, APAR and air temperature, grey circles indicate half–hourly data, whereas black circles represent daily mean values. For LUEP , ΦF , fesc and CCI, empty circle and black filled circle indicate clear and cloudy days. LUEP is light use efficiency of canopy photosynthesis (ratio of GPP to APAR), ΦF is canopy fluorescence yield (ratio of SIF and fesc to APAR), CCI is chlorophyll: carotenoid index, and fesc is the canopy escape fraction which is that the fraction of emitted SIF photons from all leaves in the canopy. Refer Eq. 1 to 3 for definitions of all terms.....	4 2
Figure 8) Relationship between SIF and GPP over APAR. The color of filled circles are half–hourly data with APAR, whereas black and white triangles represent daily means on cloudy and clear days, respectively.	

The hyperbolic regression line is the dashed red line, and R^2 represents the coefficient of determination.	4 3
Figure 9) The scatter plot of half hourly GPP and APAR (a), SIF and APAR (b) over the air temperature (both clear and cloudy days). Color map represents air temperature.	4 4
Figure 10) Relationships between air temperature and (a) daily mean canopy fluorescence yield (ΦF) and (b) light use efficiency of canopy photosynthesis ($LUEP$).	4 5
Figure 11) Seasonal correlations between $LUEP$ and (a) $fesc$, (b) ΦF , and (c) $fesc \times \Phi F$. Triangles indicate daily mean values (blue = cloudy days, red = clear days). The dashed black line is the non-linear regression line for all data; separate non-linear regressions for cloudy and clear days are shown in blue and red, respectively. Black vertical arrows denote difference between clear and cloudy days. R^2 represent the coefficient of determination. Black R^2 is for all data, red R^2 is for clear days and blue R^2 is for cloudy days and.....	4 6
Figure 12) Seasonal correlation between chlorophyll: carotenoid index (CCI) and ΦF at the canopy level. All points are daily mean values. R^2 represent the coefficient of determination. Color map represents air temperature.	4 7
Figure 13) Leaf-level quenching yield data from active fluorometer system. Daily mean leaf-level quantum yield of chlorophyll fluorescence (ΦF_{leaf}) (a), quantum yield of photochemistry ($\Phi PS(II)$) (b), quantum yield of sustained NPQ ($\Phi sNPQ$) (c) and quantum yield of reversible NPQ ($\Phi rNPQ$) (d) from late summer to winter.....	4 8
Figure 14) Experimental design at the deciduous broadleaf forest. White box represent LED-sensors at 22 m and 10 m. The percentage of leaf area density data is from (Song et al., 2015).	7 0
Figure 15) Inter-annual and seasonal variation in field-measured daily multi-layer NDVI, 1-transmittance, air temperature and satellite products (Landsat8 and MODIS; MO(Y)D09GQ)	7 7
Figure 16) Scatter plot between MODIS and Landsat8-based NDVI and NDVI from LED 22 m. For satellite NDVI, we used Landsat8 (30 m, spatial resolution), MOD09 (250 m), MYD09 (250 m) and MCD43A4 (500 m) products. The linear regression line was calculated by the	

relationship between satellite NDVI from whole products and NDVI observed by LED 22 m.	7 8
Figure 17) Annual leaf-out dates from understory, overstory, LED 22m with different phenology algorithm	7 9
Figure 18) Annual full-leaf dates from understory, overstory, LED 22m with different phenology algorithm	8 0
Figure 19) The bias (a) and R^2 (b) between observed leaf-out dates and full-leaf dates of multi-layer canopy and leaf-out dates and leaf-out dates calculated over the threshold changes	8 1
Figure 20) Relationships between leaf-out dates of over-, understory, and accumulated growing degree days (AGDD) (a) and number of accumulated chill days (NCD) (b). To avoid overlapping point between overstory and understory leaf-out dates, we used different size of the symbols.....	8 2

List of Tables

Chapter 3

Table 1) Quantum yields estimated using the MONI-PAM system	3 3
--	-----

Publications

Please note that some part of this dissertation proposal was written as stand-alone paper (see below), and therefore there are some repetition in the methods and results. Portions of this dissertation have been reprinted with permission, from previously published materials. Chapters 2 have been reprinted from *Remote Sensing of Environment*, Elsevier.

1. Kim, J., Ryu, Y., Dechant, B., Lee, H., Kim, H. S., Kornfeld, A., & Berry, J. A. (2021). Solar-induced chlorophyll fluorescence is non-linearly related to canopy photosynthesis in a temperate evergreen needleleaf forest during the fall transition. *Remote Sensing of Environment*, 258, 112362.

Acknowledgments

Publication included in this dissertation was conducted with support of the Korea Environment Industry & Technology Institute (KEITI) through its Urban Ecological Health Promotion Technology Development Project, funded by the Korea Ministry of Environment (MOE) (2019002760002).

Chapter 1. Introduction

1. Background

Recent advances in satellite remote sensing provides us with new opportunities to understand the dynamics of carbon flux interaction between terrestrial vegetation and atmosphere at regional and global scales (Ryu et al., 2019). Satellite products have been widely used to monitoring spring phenology which is important for plant functioning and ecosystem services and their biophysical and biogeochemical feedbacks to the climate system (Bonan, 2008; Jeong et al., 2014; Keenan et al., 2014; Richardson et al., 2013a). In addition, recent remotely sensed solar induced chlorophyll fluorescence (SIF) has advanced our ability to estimate gross primary production (GPP) (Frankenberg et al., 2011; Joiner et al., 2013; Joiner et al., 2014; Sun et al., 2018; Sun et al., 2017; Zhang et al., 2016) and photosynthetic capacity (Zhang et al., 2014; Zhang et al., 2018). Satellite-based SIF is also used as detector of seasonal vegetation phenology (Jeong et al., 2017; Lu et al., 2018; Walther et al., 2016).

To monitor phenology and SIF, satellite remote sensing has been widely used. Satellite has the advantage that we could see the vegetation changes in large area without visiting the site (Richardson et al., 2013b), thus it is currently being used as the most useful tool to see vegetation changes since the 1970s (Piao et al., 2019). However, there are still inherent limitations in satellite products compared to near-surface remote sensing, especially in Asia region as follows. First, satellite data could not capture fine scale spatial signals. In Asia, the land cover size is relatively small, thus, it is challenge to know detail dynamics of physiological and structural changes in vegetation by using low spatial resolution satellite

products (Riitters et al., 2000). Although high spatial satellites are launched, in current stage of SIF, the spatial resolution is 7 by 3.5 km by TROPospheric Monitoring Instrument (TROPOMI) (Köhler et al., 2018), 0.05 ° spatial resolution by GOME-2 and OCC-2. Second, satellite products could be affected by cloud strongly. In the East Asian, there are monsoon climate region, which are characterized by significant fluctuations in weather events, such as dry periods, heat waves and rainy and cloudy days (Lee et al., 2015). Therefore, satellite data showed large data gaps in summer season and it is hard to demonstrate detail mechanisms in spectral information and vegetation physiological relationship (e.g. SIF-GPP relationship) in cloudy days. Thirds, satellite could not distinguish understory and overstory separately. When we see the forest from the space by using satellite, the image contains a mixed signal of over- and understory. The seasonal pattern of NDVI observed from the satellite could be changed when two or more species are overlapped (Badeck et al., 2004). This phenomenon could directly affect the leaf-out and full-leaf dates extracted from the satellite imagery. Thus, we still need more research on the ground-based phenology and SIF to evaluate and better understand satellite-based results.

Substantial efforts have been made to monitor ground-based phenology and SIF, however, current continuous field observation is still sparse and challenges. The first reason is that the commercially available products are still expensive. The disadvantage of near-surface remote sensing system compared to satellite products is that it has a limited field of view (Richardson, 2009). To overcome this disadvantage, it is essential to develop an inexpensive system. By using the low-cost system, we can install the system in multi-points and collect data observe from large area. Second, the

spectroradiometer-based near-surface remote sensing systems have challenges of sensor calibration and maintenance in the field in order to meet the strict requirements necessary for high-quality data. The function of spectroradiometer can be influenced by environmental factors, which is difficult to control constant in the field (Pacheco-Labrador and Martín, 2015; Wang et al., 2015). Therefore, uncontrolled temperature can trigger changing radiometric magnitude, signal to noise ratio and spectral features (Hueni and Bialek, 2017; Pacheco-Labrador et al., 2019). These changing performance of sensor can make a difficulty to collect the high-quality data (Damm et al., 2011). Third, the spectroradiometer is difficult to use initially without background knowledge and experience. In order for more observations to be made in various regions and ecosystem, it should be easy for the user to use. Thus, we need to develop a ground-based remote sensing system, which is relatively inexpensive, flexible to environmental condition and easy to handle in the field.

Further efforts are needed to characterize the SIF-GPP relationship in ground-based with respect to the relative roles of canopy structure and leaf physiology. Both GPP and SIF are driven by absorbed solar radiation (Porcar-Castell et al., 2014), but they differ in a few important respects. Whereas GPP is related to gas exchange between leaves and the atmosphere, SIF is an optical signal in the near-infrared (NIR) region, where light is strongly scattered in vegetation canopies (Zeng et al., 2019). This scattering results in a decrease in the signal at the top of the canopy (Yang and van der Tol, 2018), while there is no equivalent mechanism in GPP. It is therefore necessary to investigate the relationships of LUE_p , Φ_F , and f_{esc} separately to understand the mechanisms underlying the

relationship between GPP and SIF. Compared to crops and deciduous forests, however, ENF have unique characteristics with respect to canopy structure and physiology.

The diverse environmental conditions coexist in the most forest as multi-layer canopy structure form complex time and space at the same space. Previous studies have highlighted the influence of multi-layer canopy structure on forest turbulence characteristics, hydrological cycles, radiation regimes and photosynthetic capacity in leaf-level (Baldocchi et al., 2002; Song and Ryu, 2015). In these various environmental conditions, the leaf-out period of understory and overstory are also different. For example, understory species showed earlier leaf-out dates compared to overstory due to maximize annual mass gain and survival in habitats of deciduous broadleaf forest (Seiwa, 1999; Tomita and Seiwa, 2004). However, in signal from satellite products, the image contains a mixed signal of over- and understory. The mixed signal could affect the seasonal pattern of NDVI observed from the satellite (Badeck et al., 2004) and it can directly affect the phenology extracted from the satellite imagery. Ultimately, the following questions remain: What phenology do we actually see from space compared to ground observations on multi-layer canopy phenology?

2. Purpose

The main purpose of this dissertation is to investigate the difference between the satellite-based and the field-based results through continuous observation of vegetation phenology and SIF using near-surface remote sensing system. To achieve the main goal, the following steps are necessary. 1) developing low-cost filter-based near-surface remote sensing system to monitor vegetation

phenology and SIF continuously, 2) continuously monitoring SIF in a temperate evergreen needleleaf forest, and 3) understanding the relationships between phenology from multi-layer canopies and satellite products.

In Chapter 2, I present the filter-based smart surface sensing system (4S-SIF) to overcome technical challenges of monitoring SIF in the field as well as to decrease sensor cost for more comprehensive spatial sampling. To monitor SIF, I combined ultra-narrow band pass filters and photodiode detectors to observe electro-magnetic radiation at specific wavelengths (760nm, 756nm and 770nm). I verified the satisfactory spectral performance of the band pass filters and confirmed that digital numbers (DN) from 4S-SIF exhibited linear relationships with the DN from the hyperspectral spectroradiometer. In this chapter, I 1) described the 4S-SIF 2) tested its performances in the lab with other commercial hyperspectral spectroradiometer to varying light intensities as well as sensitivity to temperature and humidity. After then, 3) I evaluated SIF quality from installed 4S-SIF sensor in the field with reference instruments.

In Chapter 3, we report the results of continuous observations of canopy-level SIF, GPP, absorbed photosynthetically active radiation (APAR), and chlorophyll: carotenoid index (CCI) in a temperate evergreen needleleaf forest. To understand the mechanisms underlying the relationship between GPP and SIF, we investigated the relationships of light use efficiency (LUE_p), chlorophyll fluorescence yield (Φ_F), and the fraction of emitted SIF photons escaping from the canopy (f_{esc}) separately. In this chapter, my objective was to investigate the SIF-GPP relationship in a temperate ENF over the transition period between summer and

winter. I formulated the following two hypotheses: H1) The seasonal SIF–GPP relationship is linear in temperate ENF, as seasonal dynamics in LUE_p are captured by Φ_F . H2) f_{esc} does not affect the SIF–GPP relationship due to its seasonal stability.

In Chapter 4, I monitored multi–layer phenology and climate variables continuously in a deciduous broadleaf forest, South Korea during 8 years. Multi–channel spectrometers installed above and below overstory canopy allowed us to monitor over– and understory canopy phenology separately, continuously. I evaluated the widely used phenology detection methods, curvature change rate and threshold with NDVI observed above top of the canopy and compared leaf–out and full leaf dates from both methods to in–situ observed multi–layer phenology. My detail research questions were: 1) What is the difference between extracted leaf–out and full–leaf dates according to different phenological phase detection methods? 2) How do satellite–based leaf–out and full–leaf dates differ from in–situ multi–layer phenology? 3) What should be caution when understanding the relationship between satellite–based spring phenology and climate changes?

Chapter 2. Monitoring sun-induced chlorophyll fluorescence using a filter-based near-surface remote sensing system

1. Introduction

Recent advances in satellite remote sensing of sun-induced chlorophyll fluorescence (SIF) provides us with new opportunities to understand the structural and physiological dynamics of vegetation at regional and global scales. The remotely sensed SIF has advanced our ability to estimate gross primary production (GPP) (Frankenberg et al., 2011; Joiner et al., 2013; Joiner et al., 2014; Sun et al., 2018; Sun et al., 2017; Zhang et al., 2016b) and photosynthetic capacity (Zhang et al., 2014; Zhang et al., 2018a). Satellite-based SIF is also used as detector of seasonal vegetation phenology (Jeong et al., 2017; Lu et al., 2018; Walther et al., 2016), indicator of drought stress in tropical rainforest and evergreen needleleaf forest (Yang et al., 2018a; Zuromski et al., 2018) and used for understanding turbulent fluxes (e.g. Alemohammad et al. (2017)). However, there are cases where the ground-based SIF presents contradictory results compare to satellite observation. For example, the correlation between SIF and GPP was reported to be low in evergreen needleleaf forest, cornfield, cropland and mixed forest because environmental condition affect the SIF-GPP relationships (Cheng et al., 2013; Nichol et al., 2019; Paul-Limoges et al., 2018). SIF was less responsive to drought than GPP in Mediterranean pine forest (Wohlfahrt et al., 2018). In addition, SIF showed a strong linear relationship with absorbed photosynthetically active radiation (APAR) than GPP in soybean and rice paddy site (Miao et al., 2018; Yang et al., 2018b).

Thus, we still need more research on the ground-based SIF to evaluate and better understand satellite-based SIF and its relationship to GPP.

Several studies have been presented to monitor ground-based SIF. Recently, commercial hyperspectral spectroradiometer-based systems have been introduced and used to observe ground-based SIF. For example, there are SFLUOR box, Fluospec, FAME, Photospec, Flox and SIFspec (Campbell et al., 2019; Cogliati et al., 2015; Du et al., 2019; Grossmann et al., 2018; Gu et al., 2018; Yang et al., 2018c). Although not configured as a system, numerous efforts have been made to observe ground-based SIF using a commercial hyperspectral spectroradiometer. (Cheng et al., 2013; DAMM et al., 2010b; Daumard et al., 2010; Goulas et al., 2017; Julitta et al., 2016; Liu and Liu, 2018; Meroni and Colombo, 2006; Rossini et al., 2010; Wieneke et al., 2018; Zhou et al., 2016).

Substantial efforts have been made to monitor ground-based SIF, however, current continuous field observation is still sparse and challenges. The first reason is that the commercially available spectroradiometer that has high performance for observing SIF are relatively expensive. The expensive sensors have limitations for installation in various location (Richardson, 2009). Therefore, in order to expand the observation, it is necessary to develop a low-cost ground-based SIF sensor. Second, the spectroradiometer-based systems have challenges of sensor calibration and maintenance in the field in order to meet the strict requirements necessary for high-quality SIF retrieval. The function of spectroradiometer can be influenced by environmental factors, which is difficult to control constant in the field (Pacheco-Labrador and Martín, 2015; Wang et al., 2015). For example, temperature could affect dimensional

modifications of the spectroradiometer optical and mechanical components (Pacheco–Labrador et al., 2019). Therefore, uncontrolled temperature can trigger changing radiometric magnitude, signal to noise ratio and spectral features (Hueni and Bialek, 2017; Pacheco–Labrador et al., 2019). These changing performance of sensor can influence SIF retrieval strongly (Damm et al., 2011). Third, the spectroradiometer is difficult to use initially without background knowledge and experience. In order for more observations to be made in various regions and ecosystem, it should be easy for the user to use. Thus, we need to develop a ground–based SIF system, which is relatively inexpensive, flexible to environmental condition and easy to handle in the field.

Using a photodiode can be used to monitoring the canopy functional changing. The variation of plant physiology can be estimated using observed reflectance at certain wavelength bands, such as photochemical reflectance index (PRI) (Gamon et al., 1997). To select the desired specific wavelength band, a system combining a photodiode and a filter has been devised (Garrity et al., 2010; Pontauiller et al., 2003; Pontauiller and Genty, 1996). These systems are used to monitor function of vegetation for deciduous, evergreen and crop species, and have proven to work continuously well (Gamon et al., 2015; Magney et al., 2016; Soudani et al., 2012). The combination of photodiode and filters have the potential to be used to extract SIF more easily because the Fraunhofer line depth (FLD) method can extract SIF using only two or three flux measurements, inside and outside an O2A absorption line (Meroni et al., 2009; Plascyk, 1975). In other words, SIF can be extracted by observing only a specific narrow wavelength band (e.g., 756 and 760 nm). Although combined filters and photodiodes already was presented to

extract SIF in leaf-level scale (Kebabian et al., 1999; Louis et al., 2005; Moya et al., 2004), a system useful for continuously monitoring canopy SIF in the field has not yet been devised.

Here, we present the filter-based smart surface sensing system (4S-SIF) to overcome technical challenges of monitoring SiF in the field as well as to decrease sensor cost for more comprehensive spatial sampling. To monitor SIF, we combined ultra-narrow band pass filters and photodiode detectors to observe electromagnetic radiation at specific wavelengths (760nm, 756nm and 770nm). In this paper, we 1) describe the 4S-SIF 2) tested its performances in the lab with other commercial hyperspectral spectroradiometer to varying light intensities as well as sensitivity to temperature and humidity. After then, 3) we evaluate SIF quality from installed 4S-SIF sensor in the field with reference instruments.

2. Instrument design and technical specifications of the filter-based smart surface sensing system (4S-SIF)

The fundamental structure of 4S-SIF is based on Kim et al. (2019). 4S-SIF consists of a Raspberry pi microcomputer (Raspberry Pi b3 module, Raspberry Pi Foundation, Cambridge, UK), customized printed circuit board (PCB) and 3D printing structure (Figure 1). We covered the top of the sensor with diffuser (White diffusing glass, Edmund optics, USA) to measure bi-hemispherical irradiance. Below the diffuser, we put the ultra-narrow band pass filters to select light for each specific wavelength respectively (755nm, 761nm and 770nm; Table 1). After then we put the collimating lens to 1) configure illumination to increase the signal and 2) only to gather the photons that came in parallel from ultra-narrow band pass filter because changes in angle of incidence to band pass

filter could make wavelength shift (Renhorn et al., 2016; Rienstra, 1998). The 3D printing structure was made of PET material and it supported the diffuser, filters, collimating lens and PCB for outdoor use. To measure up- and downwelling signal, we used two sensors in one pair (Figure 1).

To quantify electro-magnetic radiation at specific wavelengths, we developed the customized PCB. The key components of PCB are 16-bit micro controller unit (STM32F373C8T6, STMicroelectronics, Switzerland), linear amplifiers (TLV6001IDBVT, Texas Instruments, USA), silicon photodiode (S2386-18K, Hamamatsu Photonics, Japan) and transceivers (SP3485CN-L, MaxLinear, USA). The photons coming from the bi-hemispherical direction and it scattered in the diffuser and pass through the ultra-narrow band pass filter and the collimating lens (LA1540-ML, Thorlab, USA). Therefore, only the photons corresponding to a specific wavelength band reaches the silicon photodiode and when the silicon photodiode detect the photon, it forms the voltage. The amplifier amplify the voltage and the micro controller convert the analog signal into a 16-bit digital number (DN) values. The DN values are sent to the Raspberry pi via transceivers. We built the python code in microcomputer to controls the workflow chain automatically. We set up the microcomputer to save upwelling- and downwelling DN values every 10 seconds. The stored data was easily shared over the internet. The list and price of parts explained in Appendix A. One pair of 4S-SIF cost is around \$5,000 (as of July. 2019)

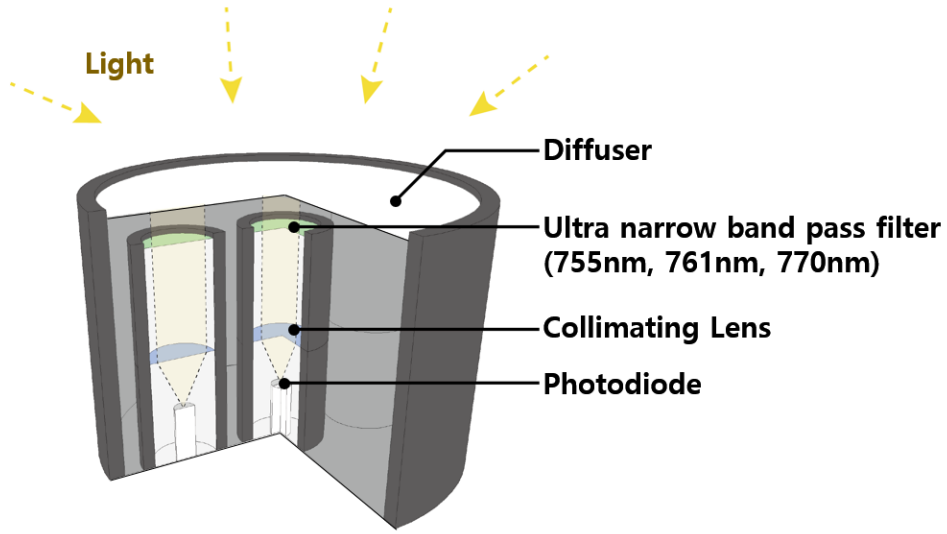


Figure 1) Image of 4S-SIF instrument complete with diffuser, ultra-narrow band pass filter, collimating lens and silicon photodiode.

2.1 Ultra-narrow band pass filter

Accurate specification of customized ultra-narrow band pass filter is one of the important factors in extracting SIF by FLD method (Damm et al., 2011; Meroni et al., 2009). To verify the performance of the filters, we used light source (HL-2000-CAL, Ocean Optics, USA) and hyperspectral spectroradiometer (QEpro, Ocean Optics, USA). We lined up the light source, filters and fiber connected to the hyper-spectral radiometer in the dark room and then measure the spectral transmitted light curve. These filters exhibited around 1nm full width half maximum (FWHM) and the peak sensitivity were 755.4, 760.6 and 770 nm, respectively (Table 1).

2.2 Calibration of 4S–SIF

To calibrate the 4S–SIF sensors, we installed the 4S–SIF sensor located in Cheorwon rice paddy site (38.2013 N; 127.2507 E). In this site, we have been collected SIF using QEpro spectroradiometer (QEpro spectroradiometer, Ocean Optics, USA) from 2016 (Yang et al., 2018b). We collected data during day of year (DOY) 234 to 242, cloudy and sunny days are included during this period. To avoid the influence of external environmental factors, the commercial spectroradiometer was kept in a temperature–controlled enclosure (Electronic enclosure, EIC SOLUTION, USA). We compared the voltages produced by the silicon photodiodes to the spectral irradiance observed from QEpro spectroradiometer across a wide range of radiation intensities. The both sensors were placed the zenith. To match the spectral resolution between QEpro and 4S–SIF, we applied transmittance of filter to QEpro spectral data and then compared between them. Digital numbers from 4S–SIF presented strong linear relationship with spectral irradiance values from the spectroradiometer in each bands (Figure 2). We also found that the linear relationships were tightly consistent over the roof top experiment.

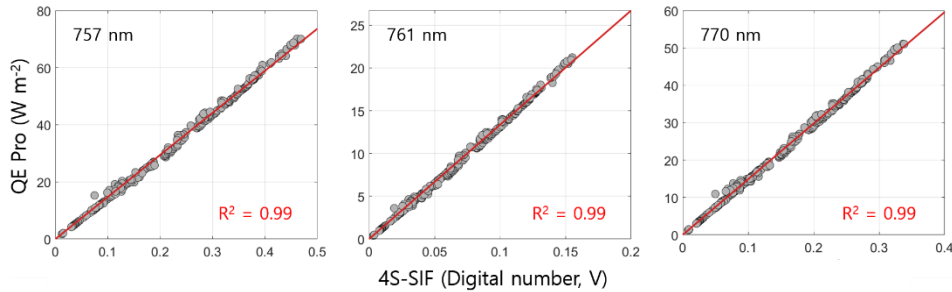


Figure 2) Evaluation of photodiodes at each band against a QEpro spectroradiometer across a wide range of solar radiation condition on 9 days.

2.3 Temperature response of 4S–SIF

To confirm stability of 4S–SIF in outdoor environment condition, we exposed 4S–SIF to various temperature and humidity conditions. We put the 4S–SIF with HMP 155 humidity and temperature probe (HMP 155, VAISALA, Finland) into temperature control box (Electronic enclosure, EIC SOLUTION, USA) together. We changed the temperature at 0 to 40 Celsius degree and the relative humidity was 20 to 100 %. We measured the humidity and temperature using HMP 155 probe every 1min interval. In case of 4S–SIF, we blocked all of the light and then measured the dark current value at 10 second intervals. We repeat this experiment two times. The each bands from 4S–SIF showed consistent dark current value over the variation of temperature and humidity (Figure 3). The dark current of 760nm was formed in a large range compare to other bands because we used twice as much resistance. This performance can be deduced that 4S–SIF produces consistently stable values when it exposed to the external environment.

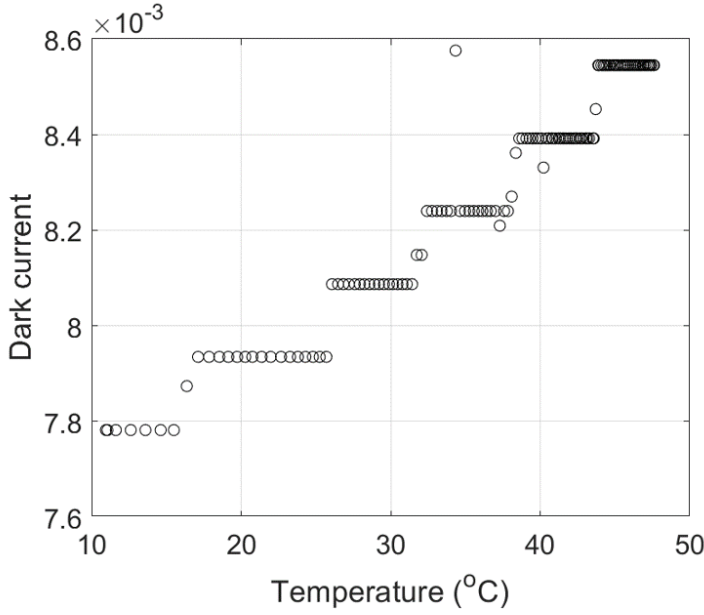


Figure 3) Dark current from 4S-SIF under various temperature. 4S-SIF showed consistent dark current value at various temperature and relative humidity.

2.4 Evaluate SIF quality from installed 4S-SIF sensor in the field

We experimented to test 4S-SIF actually detects SIF with changing the physiological mechanism of the plants. The experimental sites are a building rooftop at Seoul National University (SNU), located in the west-central portion of Korean peninsula. We planted strawberry 1.8m x 1.8m x 0.4m planter that had been filled with a mixed soil between organic and perlite (Lee et al., 2015). This small plot was built in open space to avoid shadows from canopies and buildings. We installed the QEpro spectroradiometer and 4S-SIF on horizontal booms 0.8m above the strawberry canopy. We build new system, which is combined servomotor with optical fiber, to measure upwelling and downwelling irradiance using one optical fiber and spectroradiometer. We moved the optical fiber

regularly using servomotor to observe the upwelling and downwelling irradiance of a single fiber with one spectroradiometer. We set a sufficient interval time for the upward and downward observation time to prevent the signal from mixing. The integration time of the spectroradiometer was set to 0.2 seconds in the upward direction and 0.6 seconds in the downward direction. We observed up and downward signal once within one minute. We kept the spectroradiometer in temperature-controlled enclosure (Electronic enclosure, EIC SOLUTION, USA) at 23 degree as variations in temperature and humidity could influence the performance of the CCD array in the spectroradiometer. To match the field of view between QEpro spectroradiometer and 4S-SIF, we put the cosine correct to end of fiber optics. We calculated the footprint according to the calculation method of the previous study and found that more than 50% of the signals of both sensors are affected by straw berry (Marcolla and Cescatti, 2017).

Data were collected from 10 October to 26 October (DOY: 288 to 299) in 2019. We planted the strawberry before October and we treat water around 7L every day in the morning. The strawberry was treated on DOY 293 in the early morning by herbicide 3-(3', 4'-dichlorophenyl)-1, 1-dimethylurea (DCMU) diluted to 10^{-4} M in 1% ethanol with water. DCMU is known to bind selectively to photosystem II and block its reoxidation by the plastoquinone pool (Van Rensen, 1989). Therefore, the DCMU treatment trigger that strawberry cannot perform the linear photosynthetic electron transport (Ruban et al., 1992) and the resulting excess energy causes an increase of chlorophyll fluorescence emission (Maxwell and Johnson, 2000). Binding DCMU to PS II does not change the leaf pigment composition in the short-term, thus we can assume the

spectral reflectance is not affected by herbicide treatment during rooftop experiment (Rossini et al., 2015). We harvested whole strawberry at DOY 299.

To extract SIF from QEpro and 4S-SIF, we used the FLD method (Meroni et al., 2009; Mohammed et al., 2019; Plascyk, 1975). For accurate comparison 4S-SIF, we applied the transmittance of each filter to the observed spectral data from QEpro. The data obtained every 1 minute were averaged by 10 minute. To reduce random noise, we first average the spectral data and then apply the FLD method to extract SIF (Zarco-Tejada et al., 2018). We remove that if the SIF extracted by 4S-SIF and QEpro is less than zero. 4S-SIF stored the data every 2 seconds, and the SIF was extracted by averaging at 1 minute intervals as in QEpro. PAR and NDVI were measured using 4S-LED, which is described in detail in previous studies (Kim et al., 2019). We collected PAR and NDVI with 1min interval. To calculate SIF yield, we divide observed SIF by PAR. In all graphs the error bar represents mean \pm 95% confidence interval (CI).

3. Results

SIF observed from the two sensors showed a similar pattern during rooftop experiment (Figure 4). Observed SIF using 4S-SIF and QEpro was changed according to DCMU treatment and harvesting. Incoming PAR was not significantly different during the experiment except DOY 297. On DOY 297, the day was fully cloudy, indicating that the PAR value and the SIF value observed by 4S-SIF and QEpro were relatively low. The SIF was found to increases approximately 2-times after DCMU treatment (After DOY 293), and after harvesting, it was confirmed that the SIF value did not appear (After

DOY 299).

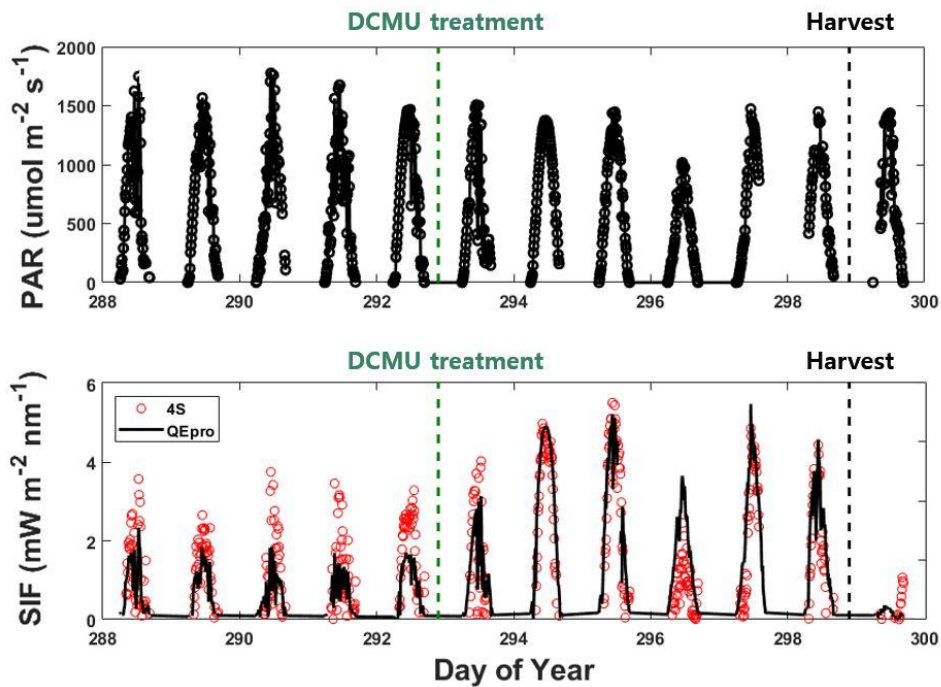


Figure 4) Daily variation of PAR and observed SIF using QEpro and 4S-SIF during rooftop experiment. PAR was relatively consistent, but SIF was changed after DCMU and harvest.

Observed SIF yield apparently noticed that the degree of response changed after the DCMU treatment (Figure 5). There was no significant change on the day when we treat DCMU. However, we found that the SIF yield value increased 210% from the day after. The size difference of the SIF yield observed in 4S-SIF and QEpro was slightly different, but it could be confirmed that the variation was similar pattern. After harvest, SIF yield value was close to zero.

The NDVI value observed at 4S-LED was consistent regardless of DCMU treatment. The degree of change during the day was small compared to the SIF yield. The degree of change during the day was small compared to the SIF yield. The value of NDVI was 0.6 before harvest and 0.33 after harvesting.

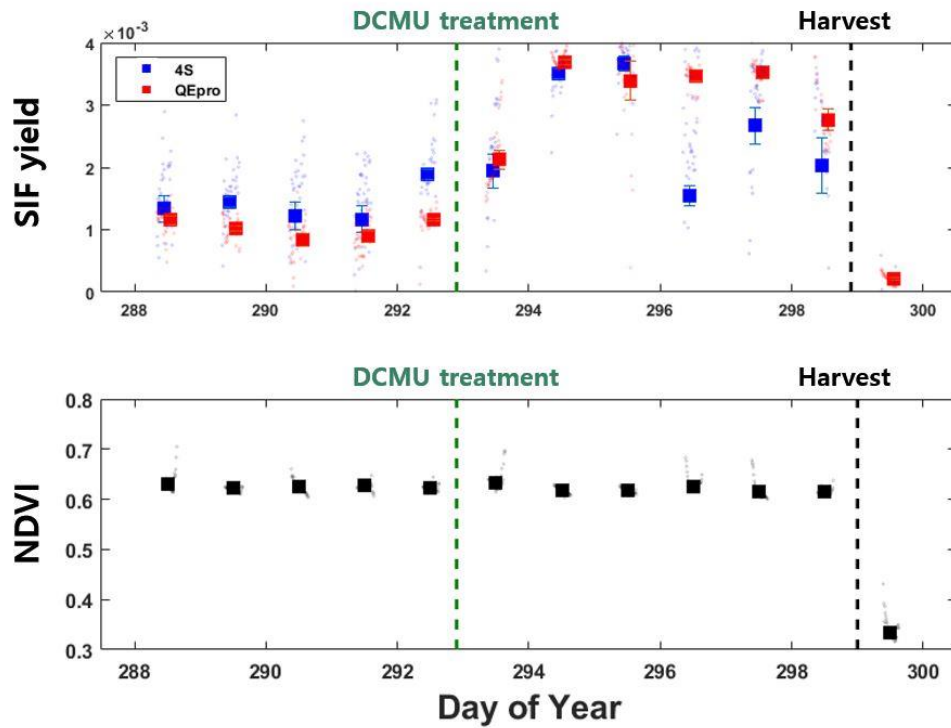


Figure 5) Daily variation of SIF yield and NDVI. SIF yield observed by 4S–SIF and QEpro showed clear change after DCMU treatment. On the other hands, NDVI was consistent around 0.6. Error bars indicate 95% CI.

A strong linear relationship was found between QEpro SIF and 4S–SIF over the experimental period ($R^2 = 0.69$, $rRMSE = 40\%$, Figure 6). The daily comparison between QEpro SIF and 4S–SIF confirmed that R^2 is relatively high ($R^2 = 0.88$).

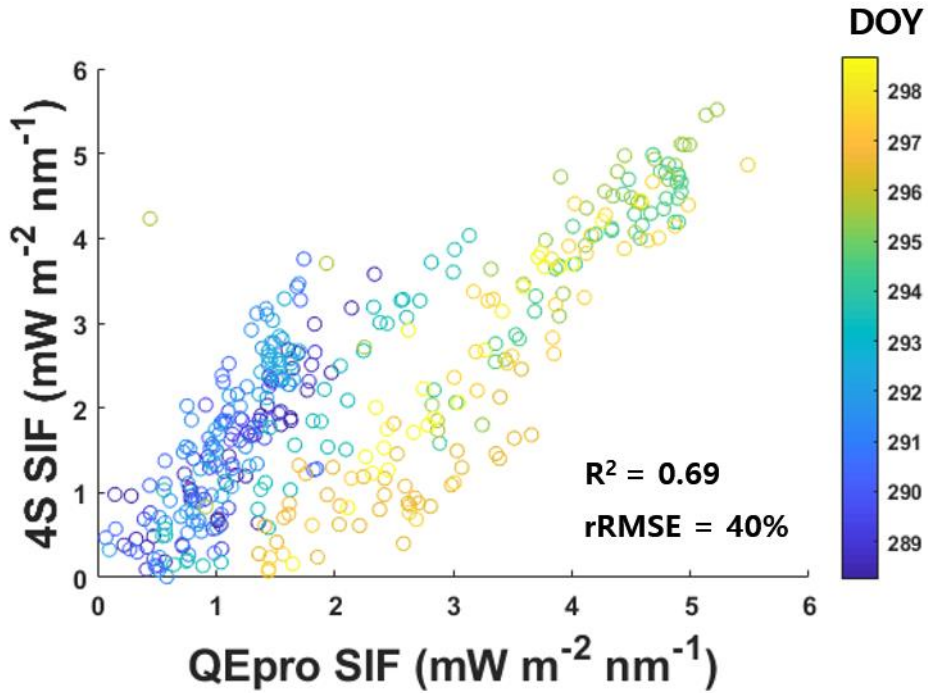


Figure 6) Scatter plots between 10-minute interval 4S-Sif and QEpro SIF. R^2 and rRMSE represent the coefficient of determination and the relative RMSE (RMSE/mean) of fitted linear regressions, respectively.

4. Discussion

4S-SIF showed reasonable performance compared to commercial spectroradiometer with low cost. A strong linear relationship was found between QEpro SIF and 4S-SIF over the experimental period ($R^2 = 0.69$, rRMSE = 40%, Figure 6). The R^2 between SIF observed by two sensors on a diurnal scale was high as 0.88. We found that there was difference between the QEpro SIF and 4S-SIF slopes before and after DCMU treatment. We think that heterogeneous strawberry plot or heterogeneity of the portions other than the footprint of the strawberry plot affects the sensor signal and makes a difference (Appendix A). Heterogeneous strawberry may

be heterogeneous in response to DCMU treatment, which explains why the relationship slopes of QE_{pro} SIF and 4S-SIF change after and before DCMU treatment. Even if the sensor observes bi-hemispheric irradiance, we think heterogeneous plot could lead to different magnitude between both sensors because the distance between the sensor and the plants is short. Thus, the effect of the plant is more than 50 %.

4S-SIF is relatively less influenced by temperature and humidity to measure electro-magnetic radiation. We confirmed that 4S-SIF showed consistent over the variation of temperature and humidity (Figure 3). Although using hyperspectral spectrometer provides us with possibility to compare SIF extracted from O2A, O2B and various retrieval method, the systems based on hyperspectral spectrometer have challenges of sensor maintenance in the field because uncontrolled temperature and humidity could affect the charge-coupled device (CCD). First, CCD could be influenced by temperature. The dark current, which could affect the signal to noise ratio (SNR), increases non-linearly with increasing temperature of the CCD (Howell, 1989; Yang et al., 2018c). Since the high SNR is a key factor in SIF retrieval accuracy (Damm et al., 2011), it is important to keep high SNR. In addition, the uncontrolled dark current can affect the reliability of the extracted SIF because the dark current affects the calibration factor (Yang et al., 2018c). Second, relatively high humidity could lead to weird signal from CCD. The CCD present a relatively high SNR when exposed to low temperatures. However, if the temperature is lowered, water vapor may affect the CCD due to the temperature difference from the outside. Therefore, too high humidity should be avoided when we use spectroradiometer. For this reason, the spectroradiometer was used in the field while stored in a

temperature-controlled enclosure. 4S-SIF, on the other hand, is relatively less affected by temperature and humidity, requiring less additional processing.

4S-SIF is easy-to-use compare to previous SIF monitoring systems. Substantial efforts have been made to monitor ground-based SIF by combining additional structures with the commercial hyper-spectrometer. For example, the automatic moving robotic arm allowed collecting daily cycles of spectral data at different location (DAMM et al., 2010b). The white reference panel was moved automatically or manually to observe incoming light (Daumard et al., 2010; Rossini et al., 2010). To measure incoming and outgoing light by using one spectrometer, shutter-based system (Miao et al., 2018; Yang et al., 2018c; Yang et al., 2015) and switch-based system was presented (Yang et al., 2018b). A system using a multiplexer to control multiple optical fibers has been devised (Cogliati et al., 2015). To collect information of multi view angle with incoming and outgoing light, combination of rotating glass prism and servo motor is used (Grossmann et al., 2018). To collect precise interpretation of the SIF signal, a system, which could synchronize sampling of spectral irradiance and environmental variables, is developed (Gu et al., 2018). Although ground-based SIF observations have been made using many systems and structures, firstly such system are difficult to use without background knowledge on system structure or spectroradiometer. Second, most observational methods use the hyper-spectrometer with optical fiber, which has the potential to cause light degradation over wavelength. Optical fiber is a useful tool for transmitting light, but depending on the degree of bending or damage, the intensity of the transmitted light varies from wavelength to wavelength (Boechat et al., 1991; Gloge, 1972). In contrast, the

4S-SIF is simple to use and free of fiber, making it easy to install and less sensitive to wavelength shift.

Chapter 3. Solar-induced chlorophyll fluorescence is non-linearly related to canopy photosynthesis in a temperate evergreen needleleaf forest during fall transition

1 Introduction

Recent advances in remote sensing of solar-induced chlorophyll fluorescence (SIF) open new opportunities to explore the physiological dynamics of vegetation from leaf to global scales (Frankenberg and Berry, 2018; Mohammed et al., 2019; Ryu et al., 2019). SIF is an optical signal emitted by excited chlorophyll *a* molecules (Baker, 2008; Meroni et al., 2009; Mohammed et al., 2019) and it is closely related to photosynthetic activity as light absorbed by chlorophyll in leaves is used for photochemistry, non-photochemical quenching (NPQ) and fluorescence (Baker, 2008; Müller et al., 2001; Maxwell and Johnson, 2000; Porcar-Castell et al., 2014). Consequently, studies have investigated the relationship between SIF and gross primary productivity (GPP) at the canopy scale based on ground observations of various ecosystems, including crops (Damm et al., 2010a; Goulas et al., 2017; Li et al., 2020; Miao et al., 2018; Yang et al., 2018b) and deciduous forests (Gu et al., 2018; Yang et al., 2017; Yang et al., 2015). However, few studies have characterized the relationship between SIF and GPP in evergreen needleleaf forest (ENF), despite their considerable contribution to both carbon fixation and stocks at the global scale (Jiang and Ryu, 2016; Liang et al., 2016; Pan et al., 2011; Thurner et al., 2014).

Further efforts are needed to characterize the SIF–GPP relationship in ENF with respect to the relative roles of canopy structure and leaf physiology. Both GPP and SIF are driven by absorbed solar radiation (Porcar–Castell et al., 2014), but they differ in a few important respects. Whereas GPP is related to gas exchange between leaves and the atmosphere, SIF is an optical signal in the near–infrared (NIR) region, where light is strongly scattered in vegetation canopies (Zeng et al., 2019). This scattering results in a decrease in the signal at the top of the canopy (Yang and van der Tol, 2018), while there is no equivalent mechanism in GPP. This difference is evident in the formulae used to describe the two processes. The light use efficiency formula (Monteith, 1972) describes GPP, as follows:

$$\text{GPP} = \text{APAR} \times \text{LUE}_p \quad (\text{Eq. 1})$$

where GPP is explained by variations in total absorbed photosynthetically active radiation (APAR) and light use efficiency of the canopy (LUE_p). By contrast, SIF can be described as follows (Damm et al., 2015; Guanter et al., 2014):

$$\text{SIF} = \text{APAR} \times \Phi_F \times f_{esc} \quad (\text{Eq. 2})$$

where Φ_F is the chlorophyll fluorescence yield from absorbed sunlight, and f_{esc} is the canopy escape fraction which is that the fraction of emitted SIF photons from all leaves in the canopy (Fournier et al., 2012; Zeng et al., 2019). Dechant et al. (2020) reported that the SIF–GPP relationship in crops was dominated by the strongly seasonal f_{esc} rather than the more temporally stable Φ_F , indicating that f_{esc} is central to understanding SIF–GPP relationships. It is therefore necessary to investigate the relationships of LUE_p , Φ_F , and f_{esc} separately to understand the mechanisms underlying the

relationship between GPP and SIF. Compared to crops and deciduous forests, however, ENF have unique characteristics with respect to canopy structure and physiology, which we describe in more detail below.

f_{esc} is generally expected to show little seasonal variation in ENF due to relatively closed and stable canopy architecture. In particular, the main characteristics of overstory canopy structure, such as leaf area index (LAI), leaf angle distribution, and leaf clumping exhibit only minor seasonal variations in ENF (Lee et al., 2019; Liu et al., 2012; Ryu et al., 2014). These unique canopy structure characteristics have direct implications for f_{esc} , which can be estimated as follows (Zeng et al., 2019):

$$f_{esc} = \frac{NIR_v}{fPAR} \quad (\text{Eq. 3})$$

where NIR_v is the product of the normalized difference vegetation index (NDVI) \times NIR reflectance (Badgley et al., 2017), and $fPAR$ is the ratio of APAR to incoming PAR. Zeng et al. (2019) demonstrated the good performance of Eq. 3 with extensive radiative transfer simulations. In ENF, there is little seasonal variation in NIR reflectance, despite the growth of new needles in the spring and leaf senescence in the fall (Kobayashi et al., 2018; Nagai et al., 2012; Ryu et al., 2014). Similarly, $fPAR$ does not exhibit strong seasonal variation in most ENFs (Majasalmi et al., 2015), although smaller changes may result from understory vegetation and needle phenology (Majasalmi et al., 2017; Ryu et al., 2014; Serbin et al., 2013).

In contrast to the stable canopy structure, ENF shows strong seasonal variation in physiology, which is reflected in the dynamics of Φ_F (Porcar-Castell, 2011). Seasonal variation of leaf-level Φ_F has been observed in accordance with the quantum yield of

photochemistry ($\Phi_{\text{PS(II)}}$), which has a unique seasonal pattern in ENF (Porcar-Castell, 2011). To protect their leaves from cold temperatures during winter, some trees in ENF activate a mechanism which adjusts leaf pigment pools and dissipates excess energy by increasing the carotenoid / chlorophyll ratio (Míguez et al., 2015; Wong and Gamon, 2015). Therefore, the chlorophyll: carotenoid index (CCI) (Gamon et al., 2016) showed strong seasonal variation in ENF as closely tracking seasonal changes in carotenoid /chlorophyll ratio (Springer et al., 2017; Wong et al., 2019; Wong et al., 2020). The quantum yield of sustained NPQ (Φ_{sNPQ}), which is associated with sustained accumulation of zeaxanthin, is dominant during the winter, when $\Phi_{\text{PS(II)}}$ is strongly reduced (Demmig-Adams and Adams III, 2006; Raczka et al., 2019; Verhoeven, 2014). When environmental conditions such as temperature and photoperiod are suitable for photosynthesis, ENF trees deactivate their protection mechanism, i.e., they undergo a de-hardening process, which declines Φ_{sNPQ} rapidly (Míguez et al., 2015; Porcar-Castell, 2011; Raczka et al., 2019). During the growing season, trees in ENF partition absorbed energy primarily through $\Phi_{\text{PS(II)}}$ and the quantum yield of reversible NPQ (Φ_{rNPQ}), which is related to the xanthophyll cycle (Demmig-Adams and Adams III, 1996; Flexas et al., 2002; Jahns and Holzwarth, 2012). Although the relationship between canopy-level Φ_{F} and LUE_{P} is not fully understood, Φ_{F} might show strong linear relationship with LUE_{P} , owing to the stability of the canopy structure and the linear canopy-level SIF-GPP relationship reported by Magney et al. (2019).

Here, our objective was to investigate the SIF-GPP

relationship in a temperate ENF over the transition period between summer and winter. Based on the above reasoning, we formulated the following two hypotheses:

H1) The seasonal SIF–GPP relationship is linear in temperate ENF, as seasonal dynamics in LUE_p are captured by Φ_F .

H2) f_{esc} does not affect the SIF–GPP relationship due to its seasonal stability.

We used continuous measurements of SIF, GPP, APAR, hyperspectral reflectance (400 – 900 nm), and relevant meteorological variables to assess relationships among LUE_p , Φ_F , f_{esc} . In addition, we monitored leaf–level physiological changes using active fluorometers during spring transition. We examined the relationship between GPP and SIF at half–hourly and daily intervals, and assessed how the relationship was affected by sky conditions.

2 Materials and Methods

2.1 Study site

Field data collection was conducted on Taehwa Mountain, Gyeonggi Province, South Korea (37.30482 N, 127.317489 E, elevation 178 m; Figure. S1). Annual precipitation is 953 ± 107 mm (mean \pm standard deviation), and the mean annual temperature is 12.7°C , ranging from -17.8°C to 33.9°C (Lee et al., 2019). The mean annual GPP is approximately $1,751\text{ g C m}^{-2}\text{ yr}^{-1}$ (Lee et al., 2019). The dominant overstory species is Korean pine (*Pinus koraiensis* Siebold et Zucc.) and the stand density is approximately 400 trees ha^{-1} . The peak growing season LAI is approximately $5\text{ m}^2\text{ m}^{-2}$ (Lee et al., 2019), mean tree diameter at breast height is $29.1 \pm 5.1\text{ cm}$, and mean canopy height is approximately 20 m. Korean

pine occupies more than 90% of the total basal area of the forest (Park et al., 2018). Korean azalea (*Rhododendron yedoense* f. *poukhanense* (H. Lév.) M. Sugim. ex T. Yamaz.) and East Asian sumac (*Toxicodendron trichocarpum* (Miq.) O. Kuntze) are the dominant understory species. Two towers accessible on foot are present at the site; the towers are 40 and 20 m tall, and are separated by 40 m. We visited the field site every 1–2 weeks over the course of the measurement period.

2.2 Leaf-level fluorescence measurement

We used a pulse-amplitude-modulation (PAM) system (MONI-PAM; Walz, Effeltrich, Germany) to measure the quantum yields of Φ_{SNPQ} , Φ_{rNPQ} , $\Phi_{\text{PS(II)}}$, chlorophyll fluorescence (Φ_{Fleaf}), and basal thermal energy dissipation (Φ_{D}) at the leaf level between DOY 25–250 in 2019. To avoid confusion of symbols, we defined that Φ_{F} is for canopy-level and Φ_{Fleaf} is for the leaf-level (Appendix E). The MONI-PAM system uses the PAM technique, in which the active fluorometer system uses weak modulated light to measure fluorescence emitted from leaf samples. We installed three fluorometers on top of the 20 m tower, and attached each leaf clip to 7 – 10 sunlit needles from the tips of adjacent branches near the top of the canopy. We endeavored to create a flat mat of needles when clipping needles into the sensor. Sensor heads were oriented southward to avoid leaf shadow effects, and clips were positioned as close to horizontal as possible. Sensors collected steady-state fluorescence yield (F_{s}), maximal fluorescence yield (F'_{m}), incoming PAR, and temperature data at 30-minute intervals. After sunset, we collected F_{s} and F'_{m} at 2-hour intervals between 22:00 and 4:00.

We assumed that nighttime F_s and F'_m corresponded to minimal (F_o) and maximal fluorescence (F_m) values, respectively (Zhang et al., 2019). We used formulae from previous studies to calculate quantum yields; an overview of these formulae and corresponding references is provided in Table 1.

Table 1 Quantum yields estimated using the MONI-PAM system

Parameter (quantum yield)	Variab les	Formula	Reference
Photochemistry	$\Phi_{PS(II)}$	$\frac{(F'_m - F)}{F'_m}$	Genty et al. (1989)
Sustained NPQ	Φ_{sNPQ}	$\frac{F}{F_m} - \frac{F}{F_{mR}}$	Porcar-Castell et al. (2011)
Reversible NPQ	Φ_{rNPQ}	$\frac{F}{F'_m} - \frac{F}{F_{mR}}$	Porcar-Castell et al. (2011)
Basal thermal energy dissipation	Φ_D	$\frac{F}{F_{mR}} - \Phi_F$	—
Chlorophyll fluorescence	$\Phi_{F_{leaf}}$	$0.1 \times \frac{F_o}{F_{mR}}$	Zhang et al. (2019)

NPQ, non-photochemical quenching

F_{mR} is summer night reference measured for our needles in the absence of sustained NPQ (Zhang et al., 2019). According to as equation 24 in Porcar-Castell (2011), MONI-PAM based seasonal variation of $\Phi_{F_{leaf}}$ could be estimated as Table 1 based on the assumption of maximum fluorescence yield of 10% for PSII at the F_m state (Barber et al., 1989; Zhang et al., 2019). To calculate Φ_{sNPQ} ,

Φ_{Fleaf} , and Φ_{D} , we used the constant F_{mR} which was measured on a summer night (DOY 255) at a time of low Φ_{sNPQ} and maximum $\Phi_{\text{PS(II)}}$ (Porcar-Castell, 2011; Zhang et al., 2019).

Strong winds caused leaves to detach from sensors, complicating continuous data collection. We manually checked F_{s} -values from each fluorometer head to identify outliers and excluded data when F_{s} -values were extremely low (< 100). We have confirmed that the F -values always exceed 100 when the leaf was attached. In addition, we installed a micro-camera to monitor if leaves were unclipped from the fluorometer head. When unclipping was observed, we promptly returned to the site to reattach sensors.

2.3 Canopy-level SIF and spectral reflectance measurements

We measured far-red SIF (760 nm) and spectral reflectance (400–900 nm) using QE Pro and Jaz spectroradiometers (Ocean Insight, Dunedin, FL, USA) installed at the top of the 40 m tower (approximately 20 m above the canopy). The Jaz spectroradiometer covers a spectral range of 350–1,020 nm at a resolution of 1 nm, whereas the QE Pro covers a spectral range of 730–790 nm with a resolution of 0.17 nm, a sampling interval of 0.07 nm, and a signal-to-noise ratio of approximately 1,000 (Yang et al., 2018b). We enclosed both spectroradiometers in a temperature-controlled box at 25° C. In addition, we installed a nitrogen gas tank to reduce the humidity in the temperature-controlled box in July, 2018. We injected nitrogen gas into the box with less than 10cc per min using a gas regulator. We collected spectral data during the transition from summer to winter from day of year (DOY) 250 to DOY 365 in 2018.

We developed a custom-made rotating prism system, similar

to that of Berry and Kornfeld (2019), for collecting spectral data with the QE Pro spectroradiometer. The system consisted of a microcontroller (Arduino Nano; Arduino, NY, USA), a 12.5-mm aluminum and MgF₂-coated N-BK7 right angle prism (Edmund Optics, Barrington, NJ, USA), two cosine correctors to measure bi-hemispheric irradiance (CC-3; Ocean Insight), a servomotor (HS311; HITEC, Seoul, South Korea), an achromatic collimating lens (74-ACR; Ocean Insight), and a 400- μ m core fiber optic cable (Ocean Insight). We used different fixed integration time between upward-facing (0.5 seconds) and downward-facing measurements (3.5 seconds). We conducted additional test to support that our fixed integration time method did not affect our SIF estimates significantly (Figure. S3 - S5). To avoid saturation in QE Pro data, we selected the integration time value when photosynthetically active radiation (PAR) was peak in summer. Prism orientation was controlled by a motor that rotated the prism between a pair of fixed angles corresponding to upward and downward light measurements. We included a buffer time of 5 seconds between data collection and motor rotation, to avoid overlap in the measurement of the upward and downward signals. We obtained three scans at 30-second intervals at each prism orientation, and calculated the average of the three scans. Data were recorded between 05:00 and 20:00, and we corrected each pair of readings for dark current and charge-coupled device (CCD) non-linearity. For dark current correction, we averaged dark current values using permanently dark detector pixels, which were always blocked inside the sensor. We subtracted the mean dark current value from the raw values of all other pixels. In addition, we verified that the relationship between the permanently dark detector pixel values and dark current observed by blocking

light at the end of fiber optics was consistent over the whole day. In addition, the dark current did not show clear spectral variation over the pixels. We set the temperature of the thermoelectric cooler (TEC) of the QE Pro spectroradiometer at -20°C , and we confirmed that there was small variation in actual TEC temperature during the measurement period ($-18.5 \pm 0.76^{\circ}\text{C}$). We modified a custom-written software package (Yang et al., 2018c) based on Omni Driver (Ocean Insight) development kits to facilitate automatic data collection. A laptop, which is connected to microcontroller and QE pro spectroradiometer, controlled the automated and synchronized workflow chain to collect data from the QE Pro and operate the servomotor via the microcontroller.

To measure spectral reflectance at visible to near infrared, we used two Jaz spectroradiometers with two fiber optics with cosine correctors. We collected the data from both spectroradiometers simultaneously and then we calculated bi-hemispheric reflectance (Schaepman-Strub et al., 2006). We collected the spectral data continuously at every 1 min from 05:00 h to 20:00 h local time using custom-written software in Java script.

To assure a high quality of radiometric calibration of the data we collected, we applied several strategies. First, we conducted the radiometric calibration of Jaz and QE Pro using a HL-2000-CAL Light Source (Ocean Insight) in the field at about monthly intervals. When we used the light source, we shielded the both the light source and the cosine corrector from direct sunlight to avoid stray light effects. Second, we confirmed that our radiometric calibrations were consistent by comparing the QE Pro and Jaz data. The relationship between radiometric calibrated irradiance data within the overlapping spectral region (730–780 nm) of the two instruments was consistent

over the entire measurement period ($R^2 > 0.98$, $RMSE < 0.01$, slope = 1.01; Figure. S2). In addition, we conducted a wavelength calibration using a calibration light source (HG-1; Ocean Insight).

2.4 *SIF retrieval*

We used the Singular Vector Decomposition (SVD) method to extract the SIF signal from calibrated downward measurements obtained by the QE Pro instrument (Guanter et al., 2012; Guanter et al., 2013; Yang et al., 2018b; Zhao et al., 2014), averaging spectral data for 30 minutes prior before SIF retrieval to reduce random noise. To minimize atmospheric effects, we used a solar Fraunhofer line retrieval window of 745–759 nm, which has minimal atmospheric interference (Guanter et al., 2013). In addition, according to Chang et al. (2020), bi-hemispherical SIF measurement with narrower fitting window showed reasonable pattern compared to incoming PAR. We then extracted the first four singular vectors to reconstruct spectrum-training data on a daily basis. Next, we used a second-order polynomial to fit surface reflectance based on the detailed evaluations of Guanter et al. (2013). Finally, although daily offset values only showed small variation across the season, we adjusted the daily offset value (i.e., the daily value without SIF) by forcing a value of zero for mean late night and early morning SIF. To quantify retrieval quality, we checked the rRMSE value between observed upwelling irradiance and reconstructive upwelling irradiance from SVD method. We removed the SIF value when rRMSE was larger than 25 % as done by a previous study (Yang et al., 2018b). We also verified the performance of our retrieval method using the data-driven simulations from ((Yang et al., 2018b); Figure. A1). Mean daily SIF was calculated as the average of all half-hourly values

collected during the period when the solar zenith angle was $< 70^\circ$.

To calculate Φ_F , we divided observed SIF by $\text{NIR}_v \times \text{PAR}$, which is an estimate of the product of APAR times f_{esc} as shown in Eq. 2.

2.5 Canopy-level photosynthesis estimates

We estimated GPP by measuring CO_2 flux above the canopy using an eddy covariance (EC) system. A three-dimensional sonic anemometer (CSAT-3; Campbell Science, Logan, UT, USA) and an open-path infrared gas analyzer (LI-7500A; LICOR, Lincoln, NE, USA) were installed at a height of 1 m on top of the 40 m tower, and data were processed using the 10-step KoFlux standardized data processing protocol (Kang et al., 2018). We used a variety of correction processes to convert raw data into high-quality flux data, including planar fit tilt correction (Wilczak et al., 2001), density fluctuation compensation (Webb et al., 1980), and frequency response correction (Fratini et al., 2012; Horst and Lenschow, 2009); all corrections were applied using LICOR EddyPro software. Data quality control procedures included removing outliers, filling data gaps using a marginal distribution sampling method (Reichstein et al., 2005), and applying nighttime CO_2 flux corrections. Quality control procedures were performed in MATLAB (MathWorks Inc., Natick, MA, USA). Between 34.5% and 42.2% of CO_2 flux data were retained after quality control. We used friction velocity (u^*) filtering (FVF; (Falge et al., 2001; Gu et al., 2005) and van Gorsel filtering (VGF) (van Gorsel et al., 2009; van Gorsel et al., 2008; van Gorsel et al., 2007) to correct CO_2 flux in estimates of GPP and ecosystem respiration (RE); these methods account for nighttime advection in

mountainous terrain. We determined that the u^* threshold values ranged between 0.30–0.35, based on the scatterplot of nighttime CO_2 flux versus nighttime u^* . Finally, we used mean GPP values derived from FVF and VGF partition to calculate mean daily GPP using half-hourly values collected during the period when the solar zenith angle was $< 70^\circ$.

2.6 *Meteorological variables and APAR*

We measured air temperature (HMP–35; Vaisala, Helsinki, Finland) and PAR (L180; LICOR) at the top of the tower. We assumed that the fraction of diffuse PAR is very closely related to the clearness index. Clearness index is the ratio of PAR above the canopy to the PAR at top of atmosphere (TOA). To calculate clearness index, we estimated PAR at TOA using the function of latitude, longitude and solar zenith angle (Cruse et al., 2015; Lee et al., 2015) and we used observed PAR value at the top of flux tower in the field. We defined cloudy days as days with a mean clearness index of < 0.5 (Yang et al., 2018b; Yang et al., 2015). In addition, we confirmed that 0.5 is around the median value in our site.

We used low-cost spectral sensors (Smart Surface Sensing System, 4S, (Kim et al., 2019)) to measure (1) incoming PAR above the canopy, (2) PAR reflected by the canopy, and (3) PAR transmitted through the canopy. To measure transmitted light, we installed three sensors approximately 8 m apart at a height of 1 m and they were not affected by surrounding understory vegetation. Incoming PAR was measured using a single sensor at the top of the 20 m tower. We calculated APAR by subtracting PAR reflected and transmitted by the canopy from incoming PAR (Yang et al., 2018b). We calibrated the 4S sensors before installation and after observation

(DOY 69 in 2019). To avoid using data collected in low-light conditions, we only used data collected during the period when the solar zenith angle was $< 70^\circ$. Data were collected at 8 points per one second and averaged every half hour.

2.7 Statistical analysis

We used the median absolute deviation (MAD) method in MATLAB to exclude extreme outliers from the GPP and SIF datasets (Rousseeuw and Croux, 1993). We removed all outliers larger or smaller than 3-MAD within a 1-day window, as well as all negative values.

To analyze LUE_p , Φ_F , and f_{esc} , we calculated the values for each term using Equations (1) and (2). We calculated LUE_p as GPP divided by APAR, and estimated f_{esc} using Equation (3). Zeng et al. (2019) demonstrated that the NIR_v -based approach explains variation in f_{esc} across different simulated canopy structures, soil brightness levels, and sun-sensor-canopy geometries. We estimated Φ_F as the observed SIF divided by the product of the observed PAR \times estimated f_{esc} . Our methods for estimating f_{esc} and Φ_F were identical to those of (Dechant et al., 2020).

To calculate NDVI, we used 670 nm for red reflectance (r670) and 800 nm for NIR reflectance (r800) (Tucker, 1979), and used reflectance of 532 nm (r532) and 630 nm (r630) to calculate the chlorophyll: carotenoid index (CCI; (Gamon et al., 2016; Springer et al., 2017)) as following equations:

$$\text{NDVI} = \frac{\text{r800}-\text{r670}}{\text{r800}+\text{r670}} \quad (\text{Eq. 4})$$

$$\text{CCI} = \frac{\text{r532}-\text{r630}}{\text{r532}+\text{r630}} \quad (\text{Eq. 5})$$

We averaged two neighboring channels to reduce noise when

extracting the wavelengths.

To quantify the non-linear relationship between GPP-SIF and $\text{LUE}_p - \Phi_F$, we fitted a hyperbolic regression function (Motulsky and Christopoulos, 2004) as follows:

$$\text{GPP} = \text{GPP}_{\max} \times \frac{\text{SIF}}{\text{SIF} + \alpha} \quad (\text{Eq. 6})$$

Where α represents $f_{\text{esc}} \times \Phi_F \times \text{coefficient in radiance unit}$, and GPP_{\max} represents the point where photosynthetic activity in the canopy becomes asymptotically saturated under high-light conditions; we used the maximum observed value of GPP. This function has previously been used to investigate SIF-GPP relationships in cropland and temperate forests (Damm et al., 2015). SigmaPlot was used for curve fitting (Systat Software Inc., San Rafael, CA, USA), and we evaluated relationships between variables using the coefficient of determination (R^2), root mean square error (RMSE), and relative RMSE (rRMSE; RMSE divided by the mean value).

3 Results

We observed decreases in GPP, SIF, and APAR between late summer and winter (DOY 250–285; Figure. 7 a–c). While GPP and APAR decreased gradually over the study period, SIF decreased rapidly at nearly double the rate of GPP. Daily LUE_p , Φ_F and f_{esc} declined over the course of the study period (Figure. 7 e–g). We observed a decline in LUE_p , but the seasonal trend was not as pronounced for Φ_F , air temperature and CCI. In addition, LUE_p and f_{esc} showed stronger sensitivity to sky conditions than Φ_F , air temperature and CCI.

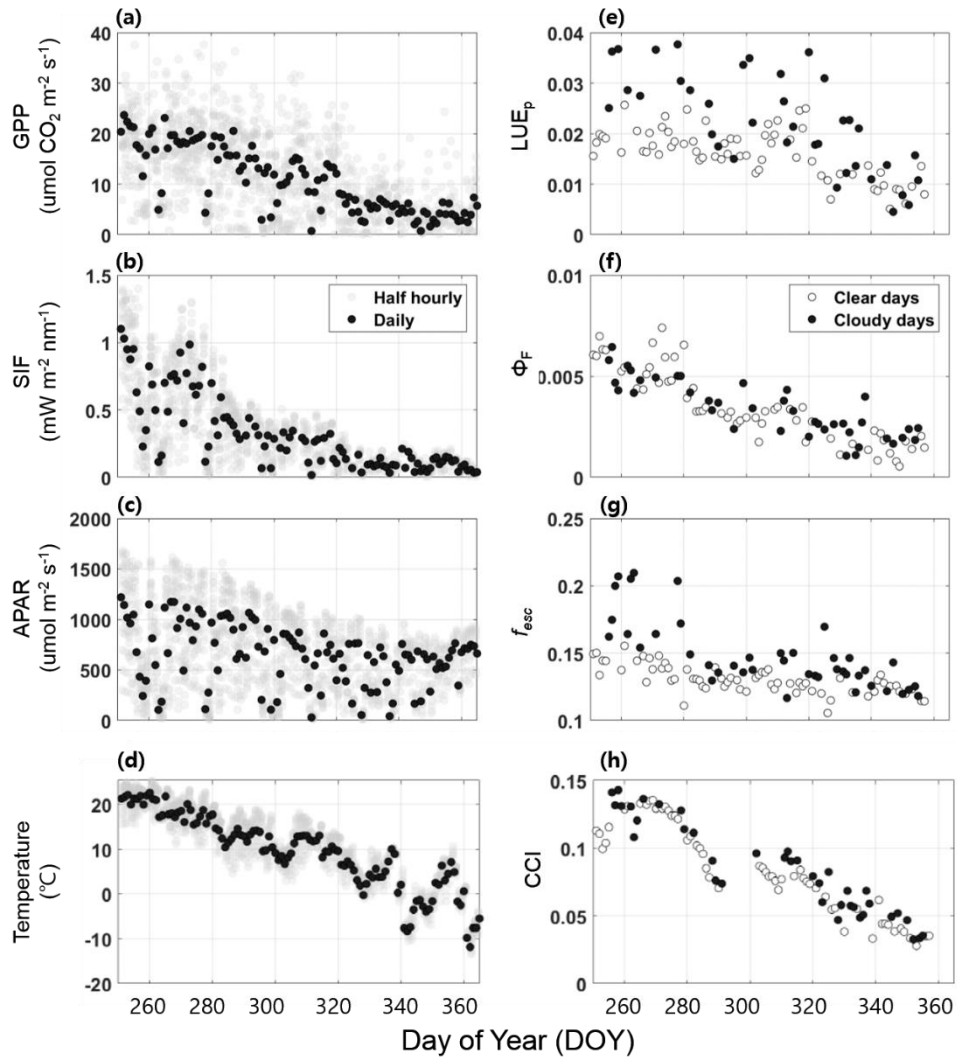


Figure 7) Seasonal variation in field-measured GPP, SIF, APAR and air temperature values (a–d), and LUE_p , Φ_F , f_{esc} and CCI (e–h). For GPP, SIF, APAR and air temperature, grey circles indicate half-hourly data, whereas black circles represent daily mean values. For LUE_p , Φ_F , f_{esc} and CCI, empty circle and black filled circle indicate clear and cloudy days. LUE_p is light use efficiency of canopy photosynthesis (ratio of GPP to APAR), Φ_F is canopy fluorescence yield (ratio of SIF and f_{esc} to APAR), CCI is chlorophyll: carotenoid index, and f_{esc} is the canopy escape fraction which is that the fraction of emitted SIF photons from all leaves in the canopy. Refer Eq. 1 to 3 for definitions of all terms.

The relationship between GPP and SIF in the canopy was strongly non-linear (Figure. 8); hyperbolic regression yielded a considerably higher R^2 and lower rRMSE ($R^2 = 0.91$, rRMSE = 19%) than linear regression ($R^2 = 0.80$, rRMSE = 27%). We found that RMSE did not differ between cloudy and clear days (1.9 and 2.0, respectively).

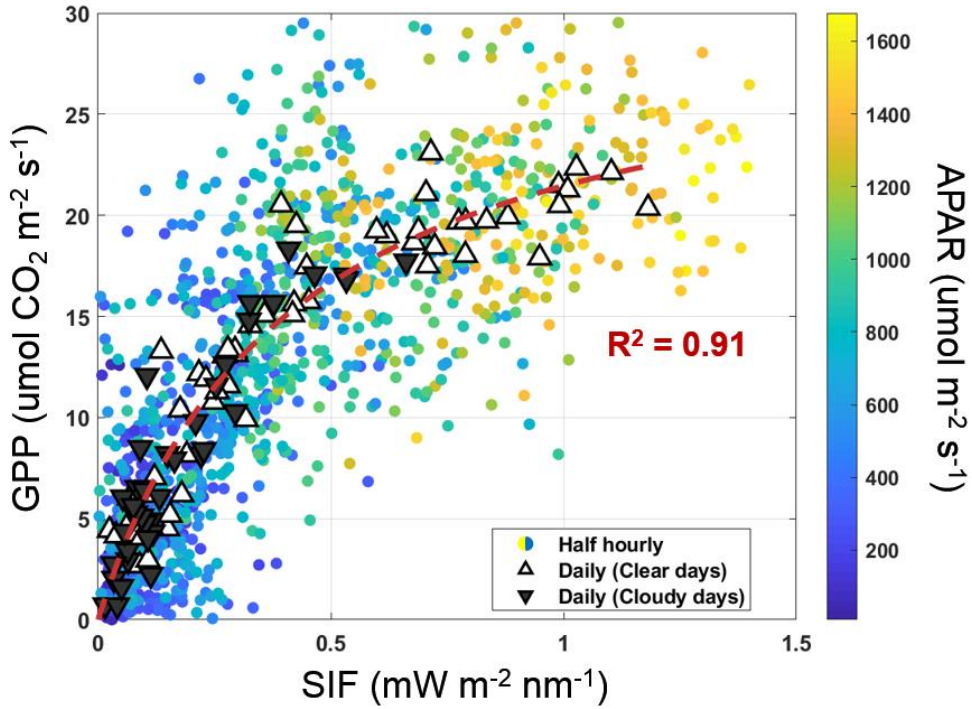


Figure 8) Relationship between SIF and GPP over APAR. The color of filled circles are half-hourly data with APAR, whereas black and white triangles represent daily means on cloudy and clear days, respectively. The hyperbolic regression line is the dashed red line, and R^2 represents the coefficient of determination.

We found that the slopes between SIF and APAR showed gradual changes with the air temperature (Figure. 9b). At high air temperature (~ 25 °C), the slope of the SIF–APAR was 0.0006, and as the temperature decreased, the slope of the SIF–APAR became

smaller ($\sim 0^\circ\text{C}$, slope of the SIF–APAR was 0.00005). This corresponds to the decreasing seasonal pattern of canopy–level Φ_F (Figure. 7f). On the other hand, the scatter plots in GPP–APAR and GPP– $f_{esc} \times \text{APAR}$ did not show a clear slope changes with air temperature, and the overall pattern of the two scatter plots did not show clear difference (Figure. 9a).

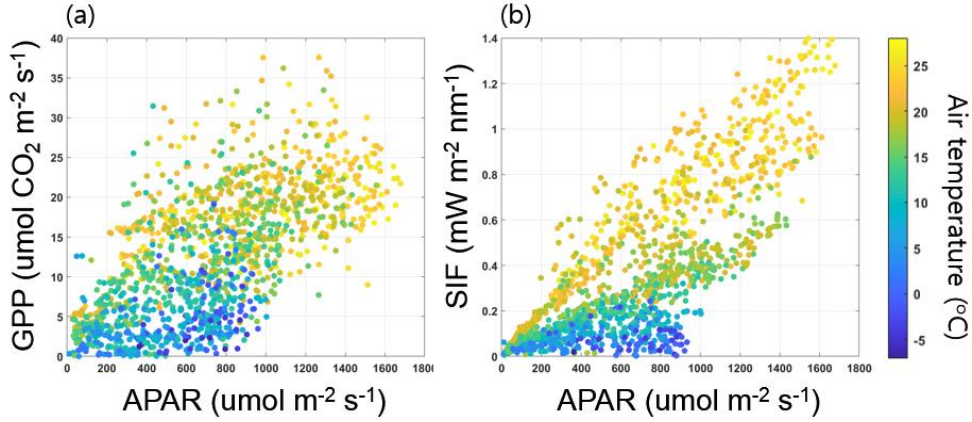


Figure 9) The scatter plot of half hourly GPP and APAR (a), SIF and APAR (b) over the air temperature (both clear and cloudy days). Color map represents air temperature.

While mean daily LUE_P exhibited saturation in high air temperatures, Φ_F did not saturate (Figure. 10), but rather increased gradually with air temperature. We observed Φ_F values of 0.002–0.008 ($\text{mW m}^{-2} \text{sr}^{-1} \text{nm}^{-1}$) / ($\mu\text{mol photons m}^{-2} \text{s}^{-1}$) at temperatures between -10°C and 25°C . When the air temperature was below freezing, Φ_F remained relatively constant at approximately 0.002. Values of LUE_P ranged from approximately 0.005 to 0.04 ($\mu\text{mol CO}_2 \text{m}^{-2} \text{s}^{-1}$) / ($\mu\text{mol photons m}^{-2} \text{s}^{-1}$).

Whereas LUE_P showed strong sensitivity to sky conditions,

Φ_F was relatively insensitive (Figure. 10). We observed a variation of LUE_P in response to changes in sky conditions (Figure. 10b), with lower values on clear days and higher values on cloudy days. In particular, LUE_P exhibited a marked difference in magnitude between clear and cloudy days at temperatures $> 10^\circ \text{C}$.

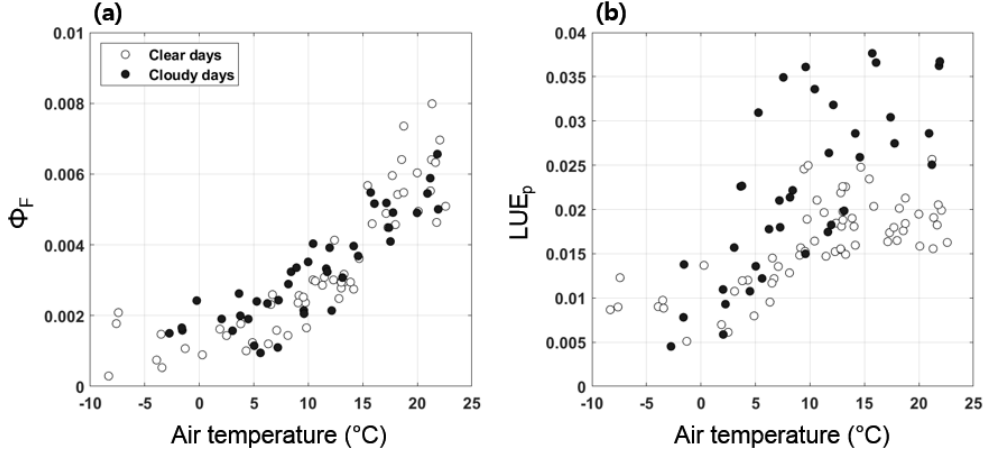


Figure 10) Relationships between air temperature and (a) daily mean canopy fluorescence yield (Φ_F) and (b) light use efficiency of canopy photosynthesis (LUE_P).

We observed substantial differences in the relationships of LUE_P to Φ_F and f_{esc} (Figure. 11). The non-linear $LUE_P - \Phi_F$ relationship in seasonal time scale appeared. The correlation between LUE_P and f_{esc} was stronger ($R^2 = 0.53$ with linear regression; Figure. 11a) than that between LUE_P and Φ_F ($R^2 = 0.37$ with hyperbolic regression; Figure. 11b). In addition, the relationship between LUE_P and $\Phi_F \times f_{esc}$ was stronger than that between LUE_P and Φ_F alone ($R^2 = 0.45$ with hyperbolic regression; Figure. 11c).

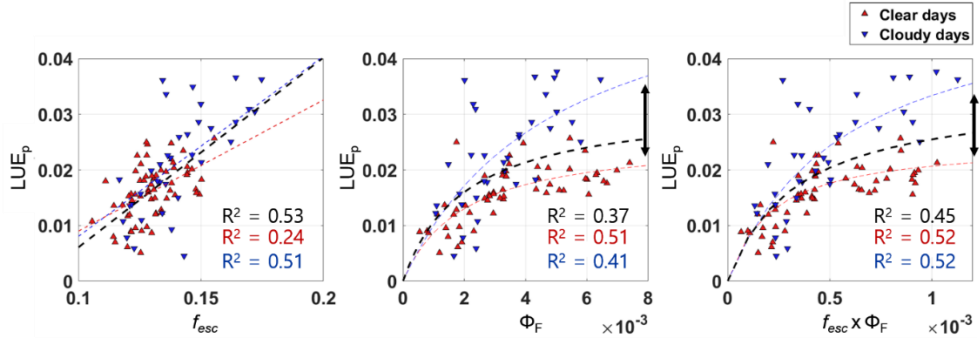


Figure 11) Seasonal correlations between LUE_p and (a) f_{esc} , (b) Φ_F , and (c) $f_{esc} \times \Phi_F$. Triangles indicate daily mean values (blue = cloudy days, red = clear days). The dashed black line is the non-linear regression line for all data; separate non-linear regressions for cloudy and clear days are shown in blue and red, respectively. Black vertical arrows denote difference between clear and cloudy days. R^2 represent the coefficient of determination. Black R^2 is for all data, red R^2 is for clear days and blue R^2 is for cloudy days and.

We found that canopy-level Φ_F was highly correlated to a canopy-level CCI across the seasons ($R^2 = 0.84$, Figure. 12). The seasonal patterns for CCI and Φ_F were continuously decreasing during senescence period (Figure. 7). There was no significant difference in both CCI and Φ_F depending on fractions in diffuse light. In case of the CCI, there were data gaps during DOY 292 to 301 because of unstable power supply (Figure. 7h).

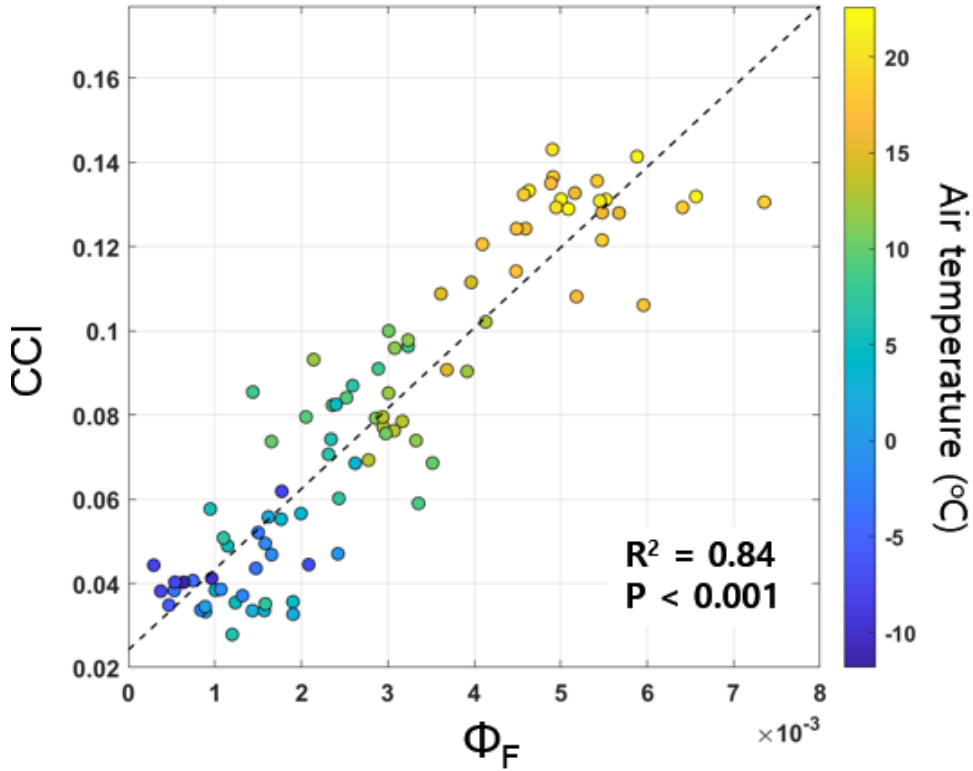


Figure 12) Seasonal correlation between chlorophyll: carotenoid index (CCI) and Φ_F at the canopy level. All points are daily mean values. R^2 represent the coefficient of determination. Color map represents air temperature.

We found that leaf-level results based on active PAM measurements were overall similar as the canopy-level findings (Figure. 13). In particular, $\Phi_{F_{leaf}}$ gradually increased with air temperature and was rather insensitive to sky condition. However, leaf-level $\Phi_{PS(II)}$ showed no consistent dependence on air temperature for high values in summer and there was a clear difference between clear and cloudy days. Φ_{rNPQ} also showed saturation at high air temperatures, but Φ_{rNPQ} reacted in the opposite direction to the sky condition compared to $\Phi_{PS(II)}$. Φ_{sNPQ} was less affected by sky condition and suddenly dropped at air

temperatures of about 5°C.

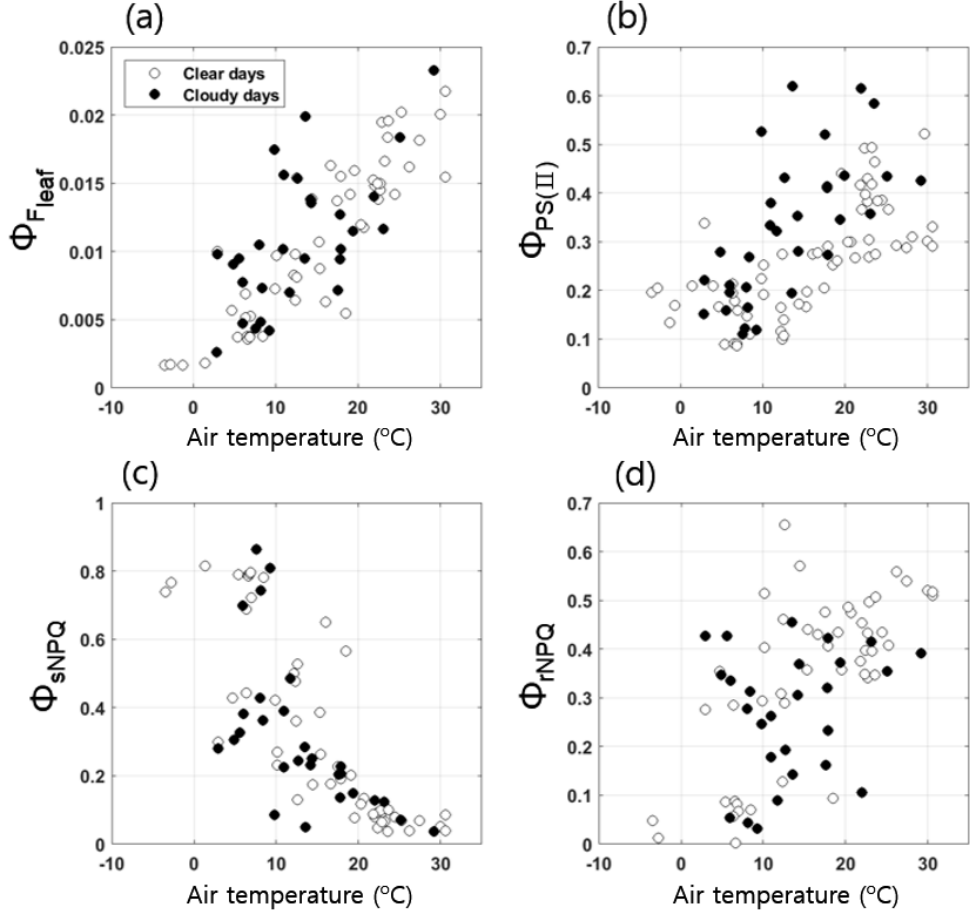


Figure 13) Leaf-level quenching yield data from active fluorometer system. Daily mean leaf-level quantum yield of chlorophyll fluorescence ($\Phi_{F_{leaf}}$) (a), quantum yield of photochemistry ($\Phi_{PS(II)}$) (b), quantum yield of sustained NPQ (Φ_{sNPQ}) (c) and quantum yield of reversible NPQ (Φ_{rNPQ}) (d) from late summer to winter.

4 Discussion

We explored the relationship between canopy-level GPP and SIF in a temperate ENF, and analyzed variations in LUE_p , Φ_F , and f_{esc} individually to better understand the mechanisms underlying the GPP-SIF relationship. The relationship was found to be strongly non-linear, even on a seasonal time scale, contradicting our initial

hypothesis that the SIF–GPP relationship is linear for ENF (Figure. 8). In addition, the product of Φ_F and f_{esc} correlated more strongly with LUE_p compared to Φ_F alone (Figure. 11), which partly contradicts our second hypothesis that f_{esc} does not substantially affect the SIF–GPP relationship in ENF. Here we provide a detailed discussion of our results with respect to the hypotheses. To strengthen our discussion, we include continuous observations of leaf–level chlorophyll fluorescence data collected from sunlit leaves. Although the growth stage of leaf–level data did not overlap with that of canopy data, the leaf–level data offer valuable information about functional relationships between efficiency terms and air temperature.

4.1 *Non–linear relationships between SIF and GPP*

We found that the SIF–GPP relationship was strongly non–linear with the hyperbolic regression exhibiting considerably higher R^2 (0.91) than the linear regression (0.80, daily; Figure. 8). Those results are partly opposed to our hypothesis H1) that the seasonal SIF–GPP relationship is linear in temperate ENF, as seasonal dynamics in LUE_p would be captured by Φ_F (Magney et al., 2019). We think that different physiological mechanisms could explain the non–linear SIF–GPP relationship at *diurnal* and *seasonal* time scales. This is discussed in more detailed in the paragraphs below.

At diurnal time scales, the non–linear SIF–GPP relationship could be explained by fundamental differences between the light responses of SIF and GPP. GPP saturates at high light whereas SIF has a stronger tendency to keep increasing (Gu et al., 2019). In fact, we could clearly see that SIF and GPP responded linearly and non–linearly to APAR at diurnal time scales (Figure. 9 and Appendix B).

SIF showed strong linear relationships to APAR even though the slopes declined with time because Φ_F decreased. On the other hand, GPP showed clearly saturated pattern with APAR. This non-linear pattern could be explained by the low value of maximum rate of carboxylation (V_{cmax}) at our site. The light saturation point of GPP occurs at relatively low APAR under low V_{cmax} , and rises with increasing V_{cmax} . By contrast, SIF does not show a clear saturation pattern with APAR as it is much less sensitive to V_{cmax} than GPP based on the Soil Canopy Observation, photochemistry and Energy fluxes (SCOPE) model (Zhang et al., 2016a). Therefore, the SIF-GPP relationship at half-hourly time scales is more strongly non-linear in low V_{cmax} canopies. Our findings (Figure. 8) are consistent with those of (Zhang et al., 2016a), as V_{cmax} at our site was only $37.3 \mu\text{mol m}^{-2} \text{s}^{-1}$ for sunlit leaves at the peak of the growing season (Kim, 2014). Similar values ($37.6 \mu\text{mol m}^{-2} \text{s}^{-1}$) have also been reported for Korean pine at other sites (Zhou et al., 2011). These values are notably lower than the global mean value for ENF species ($62.5 \mu\text{mol m}^{-2} \text{s}^{-1}$; (Kattge et al., 2009)), suggesting that the diurnal SIF-GPP relationship might be more strongly non-linear in temperate ENF.

While low V_{cmax} appears to explain the non-linearity of the diurnal SIF-GPP relationship, it cannot not fully explain the non-linearity of the *seasonal* SIF-GPP relationship at our site. The non-linear effects of low V_{cmax} on the SIF-GPP relationship are substantially reduced when using daily mean values, and nearly disappear at the weekly scale, even with V_{cmax} values as low as $50 \mu\text{mol m}^{-2} \text{s}^{-1}$ according to SCOPE simulations (Zhang et al., 2016a). Consistent with these results, Magney et al. (2019) reported that a non-linear SIF-GPP relationship at hourly time scales which became linear at daily and weekly time scales with relatively low V_{cmax} (40

$\mu\text{mol m}^{-2} \text{ s}^{-1}$; (Dutta et al., 2019)). In contrast, we found that daily mean values still showed a strong non-linear SIF-GPP relationship that was overlapping with the relationship based on half-hourly data (Figure. 8). This indicates that the low V_{cmax} alone cannot explain the non-linearity of the SIF-GPP relationship at the seasonal time scale at our site.

The non-linearity of the SIF-GPP relationship at the seasonal time scale could be due to differences between LUE_p and Φ_F in terms of physiological mechanisms. In particular, the seasonal variation of LUE_p showed saturated pattern in high air temperature especially in clear days but Φ_F was highly correlated to air temperature (Figure. 10). Two main factors could contribute to the saturation of LUE_p at high air temperature. First, higher PAR values coincide with high air temperature in summer and the resulting higher APAR may lead to stronger saturation of GPP, which is limited by V_{cmax} under such conditions (Figure. A2). Second, the saturation pattern of LUE_p is related to distributions of intercepted photon energy (Porcar-Castell et al., 2014). The reversible NPQ is competitively involved in energy partitioning to reduce the excess energy at high air temperature, which is likely to explain saturation of LUE_p in such air temperature (Figure. 13). As air temperature decreases, the sustained NPQ, which has unique seasonality in ENF, is activated and the portion of photochemistry and reversible NPQ is decreased, which may diminish the saturation of LUE_p across autumn to winter (Figure. 13). According to SCOPE simulation and leaf-level measurement, SIF is much less sensitive to V_{cmax} and photon energy partitioning than GPP, which could explain the absence of saturation of Φ_F at high air temperatures (Gu et al., 2019; Zhang et al., 2016a).

The seasonal variation of Φ_F could be more tightly related to pigment pool changes rather than LUE_P . We found that the Φ_F –CCI relationship was strongly linear in our site ($R^2 = 0.84$; Figure. 12) and CCI was strongly correlated to the pigments pool changes in sunlit leaves (Appendix D). Stronger CCI– Φ_F correlation ($R^2 = 0.84$ in Figure. 12) than CCI– LUE_P correlation ($R^2 = 0.48$ in Figure. S9) further supports our reasoning as CCI is known to be primarily sensitive to pigment pool changes. In addition, we found that LUE_P responded to sky conditions while Φ_F (and CCI) did not respond (Figure. 7). The possibility of strong relationship between pigment pool changes and Φ_F have been suggested in previous studies. Springer et al. (2017) reported that leaf–level florescence yield and CCI had strong linear relationship in ENF. Simulations using SCOPE model also showed that the chlorophyll pool could control the magnitude of Φ_F when LAI is stable (Du et al., 2017).

The leaf–level results based on active PAM measurements support our findings from the canopy–level data. We found overall similar relationships in $\Phi_{F_{\text{leaf}}}$, air temperature and sky condition compared to the canopy–level Φ_F (Figure. 10 and 13). $\Phi_{F_{\text{leaf}}}$ continued to increase with air temperature (Figure. 13a). In high air temperature, Φ_{rNPQ} was the main de–excitation pathway to reduce excess energy (Figure. 13d) and caused the saturation of $\Phi_{PS(II)}$ (Figure. 13b). The dynamic range of changes in $\Phi_{F_{\text{leaf}}}$ was small (<0.01) within one day and from day to day, while Φ_{rNPQ} and $\Phi_{PS(II)}$ varied widely (~ 0.8) depending on sky conditions (Magney et al., 2020). Therefore, Φ_{rNPQ} and $\Phi_{PS(II)}$ seem more sensitive to sky

conditions, and Φ_{Fleaf} seems to be highly correlated with air temperature regardless of sky conditions. In addition, we found that Φ_{Fleaf} and $\Phi_{\text{PS(II)}}$ had non-linear relationships on a diurnal scale (Appendix C), which is consistent with previous studies (Maguire et al., 2020; Porcar-Castell et al., 2014; Zhang et al., 2016a).

It has been documented in the literature that the response of Φ_{SNPQ} to temperature differs between the fall and spring transitions. In particular, it was reported that the fall transition tends to be more gradual compared to the steeper transition in spring (Magney et al., 2019; Porcar-Castell, 2011; Raczka et al., 2019). This indicates that active PAM measurements at our site would also show such differences in the response of Φ_{SNPQ} to air temperature in fall compared to the spring measurements. However, this does not affect our results on the leaf-level responses of Φ_{Fleaf} and $\Phi_{\text{PS(II)}}$ regarding the high temperature response as at such temperature Φ_{SNPQ} is effectively zero and the response is expected to be more consistent between different times of the year.

4.2 *Role of f_{esc} in the SIF-GPP relationship*

f_{esc} was fairly stable across the seasons especially in clear sky conditions (Figure. 7g). As we estimated f_{esc} as the ratio of NIR_v to fPAR (Eq. 3), it is instructive to examine the dynamics of these components individually. Both NIR_v and fPAR exhibited seasonal variation, with declining values from late summer towards winter (Figure. S6). However, the seasonal variations in NIR_v and fPAR partially canceled each other out (Eq. 3), resulting in the rather stable values of f_{esc} across the seasons particularly clear sky days (Figure.

7g). The seasonal patterns in NIR_v and fPAR were at least partly caused by changes in daily mean solar zenith angle (Figure. S7), understory (Figure. S8) and needleleaf phenology (Li and Fang, 2015; Majasalmi et al., 2017; Ollinger, 2011).

Despite its seasonal stability, f_{esc} played a role in strengthening the relationship between LUE_p and Φ_F due to its sensitivity to sky conditions (Figure. 11). This result appears to contradict our second hypothesis that f_{esc} does not affect the SIF–GPP relationship due to its seasonal stability. Sky condition effects were primarily visible at diurnal time scales and tend not to show strong gradual seasonal variations, which implies that the contradiction could indeed be apparent. The tendency for f_{esc} to increase in diffuse sky conditions was also reported in a wheat site (Dechant et al., 2020) but no further detailed analyses were conducted. Therefore, we evaluated the separate responses of the two components of f_{esc} at our site. To focus on the response of fPAR and NIR_v to diffuse sky conditions only, we removed the seasonal trends related to solar zenith angle and phenology (Figures. S10 and S8). After this, we compared between seasonally de-trended fPAR, NIR_v and clearness index. Based on this analysis, fPAR and NIR_v were positively and negatively correlated to clearness index, respectively (Figure. S10), which led to a negative relationship between f_{esc} and clearness index ($R^2 = 0.5$; Figure. S10). Therefore, f_{esc} could show high values in the cloudy conditions, similar to LUE_p .

4.3 Implications of non-linear SIF–GPP relationships in temperate ENF

Our findings differ from previous results as SIF is nonlinearly

related to GPP in a temperate ENF. Based on in-situ data, several studies reported that Φ_F exhibits a linear response to seasonal variations in photosynthesis (Springer et al., 2017; Zhang et al., 2019), and that daily average SIF has a linear relationship with GPP at the canopy level in ENF (Magney et al., 2019). In addition, satellite-based SIF data showed a strong linear relationship with GPP at the seasonal scale (Jeong et al., 2017; Joiner et al., 2014; Sun et al., 2017; Walther et al., 2016; Zhang et al., 2018b). However, our findings of a strongly non-linear SIF-GPP relationship indicate that we need to study the SIF-GPP relationship in ENF in more detail, for example by conducting canopy structure and physiological aspect separately when using satellite SIF retrievals. In addition, more ground-based observations that cover the range of environmental conditions of ENF would be helpful to understand the non-linear SIF-GPP relationship better. Apart from that, the findings of Wohlfahrt et al. (2018) that SIF did not track GPP well during a short-term heat wave in ENF further indicate that non-linear, complex SIF-GPP relationships exist at different time scales, from diurnal scales over a few weeks up to the seasonal time scale.

Our results support the importance of quantifying LUE_P , Φ_F , and f_{esc} , individually, and assessing the relationships among these variables. In clear days, we found that there was a stronger correlation between LUE_P and Φ_F ($R^2 = 0.51$) than a correlation between LUE_P and f_{esc} ($R^2 = 0.24$; Figure. 11). Φ_F substantially outperformed f_{esc} in terms of LUE_P estimation, as Φ_F exhibited clear seasonality. In addition, we confirmed that $APAR \times f_{esc} \approx NIR_v \times PAR$ (Eq.3) could not track GPP well especially in low air temperature (Figure. S12). These results suggest that satellite-

based $NIR_v \times PAR$ could not track GPP well in ENF in fall to winter. Nonetheless, our results suggest that f_{esc} strengthens the relationship between LUE_P and Φ_F (improvement from $R^2 = 0.37$ to $R^2 = 0.45$; Figure. 11). Overall, our findings indicate that both physiological (Φ_F) and structural variation (f_{esc}) should be considered together when estimating GPP using remotely sensed SIF data in ENF. In non-ENF sites, it is also necessary to assess LUE_P , Φ_F , and f_{esc} separately. Dechant et al. (2020) found that daily Φ_F was not correlated with LUE_P ($R^2 < 0.08$) while strong seasonal variation in f_{esc} showed a positive relationship with LUE_P ($R^2 = 0.4 - 0.6$) in crops. Liu et al. (2020b) reported partly even stronger daily correlations between f_{esc} and LUE_P for corn sites ($R^2 = 0.5 - 0.8$). Thus, information about canopy structure ($NIR_v \times PAR$) may allow robust estimates of GPP in ecosystems other than ENF, which is also supported by several other studies (Badgley et al., 2019; Badgley et al., 2017; Baldocchi et al., 2020; Jiang et al., 2020; Wu et al., 2020).

Simulating SIF in ENF currently still has considerable limitations, which could potentially be improved by considering our findings. For example, SCOPE (van der Tol et al., 2009; Vilfan et al., 2016) was originally developed for crops and does not adequately represent the complex, highly clumped canopy structure of ENF. Furthermore, there is currently no process-based subroutine for Φ_{sNPQ} dynamics. Raczka et al. (2019) attempted to overcome this limitation by parameterizing a Φ_{sNPQ} model for the community land model (CLM) using field data. However, they assumed the light saturation point of Φ_{rNPQ} to be constant over the season. Parazoo et al. (2020) analyzed simulations from an ensemble of process based fluorescence models in an ENF site and found large discrepancies

among the models. Therefore, additional works are needed to improve process-based SIF models in ENF, particularly for the Φ_F -air temperature relationship that we observed. In addition, combination of leaf-level and canopy-level fluorescence data with 3D radiative transfer model forced with LiDAR data could open up new possibilities to improve our understanding of the relationship between canopy structural and functional traits in ENF (Liu et al., 2019).

Although we found a non-linear SIF-GPP relationship and strong correlation between CCI and Φ_F , further research is needed to deepen our understanding of the mechanisms leading to the observed patterns in our results as follows. First, the physiological mechanisms of ENF in spring and autumn could be different. According to Porcar-Castell (2011), sustained NPQ in spring was larger than autumn under same air temperature. Therefore, to understand the physiological mechanisms in ENF in-depth, it is necessary to have simultaneous observations at the leaf- and canopy levels over a long period of time. Second, it is necessary to accurately estimate the total emitted SIF to understand the relationship between SIF and GPP at the canopy-level better. Total emitted SIF could have stronger correlation with GPP than canopy escaping SIF because shade leaves could not be ignored (Lu et al., 2020). In this respect, leaf-level physiological parameters such as V_{cmax} , $\Phi_{PS(II)}$ and Φ_{Fleaf} in shade leaves should be also measured to understand whole canopy.

5. Conclusion

We investigated the relationship between in-situ, canopy-level SIF and GPP data in a temperate ENF, and we found a strong

non-linear relationship between SIF and GPP. To understand the mechanisms underlying the non-linear SIF-GPP relationship, we investigated the relationships of LUE_p , Φ_F , and f_{esc} separately. Our detailed analyses resulted in three main conclusions. First, the SIF-GPP relationship was strongly non-linear as their response to APAR and air temperature was different. In diurnal time scale, Φ_F was not saturated but LUE_p showed a clearly saturated pattern especially in high light intensity and air temperature. In seasonal time scale, we found that there was non-linear LUE_p and Φ_F relationship. Second, we found that f_{esc} could strengthen the Φ_F - LUE_p relationship as f_{esc} responded to sky conditions in a similar way as LUE_p . Third, seasonal variation of Φ_F could be more related to pigment pool changes rather than LUE_p as Φ_F was strongly correlated to CCI during senescence period. Further research is needed to deepen our understanding of the mechanisms leading to the observed patterns in our results. We believe that our findings may contribute to a better understanding of SIF-GPP relationships in ENF.

Appendix A. Evaluation of SIF retrieval method

In this paper, we retrieved SIF using the singular vector decomposition method (SVD). We verified the reliable retrieval performance of our method with data-driven simulations. The relationship between input SIF and retrieved SIF showed strong linear relationship and low bias ($R^2 = 0.97$, $RMSE = 0.08$ and relative bias $< 0.1 \%$, Figure. A1).

To evaluate our SIF retrieval method, we used the outgoing irradiance spectra with known reflectance and known fluorescence magnitudes. The simulated upwelling irradiance (I_{OUT}) was calculated as:

$$I_{OUT} = I_{in} \times ref + SIF$$

Where I_{in} is measured incoming irradiance and *ref* stands for the reflectance spectra from field measurements with the Jaz spectrometer. To remove SIF effects in the measured reflectance, especially in the O2A band, we smoothed the reflectance using the *rlloess* method using a span of 50% of the total pixel number of reflectance in MATLAB software (Mathworks, Inc., USA). *SIF* represents canopy fluorescence with known fixed spectral shape of emitted fluorescence which is measured. To consider realistic seasonal variation of SIF, we set the magnitude of SIF as 5 % of incoming irradiance for day of year (DOY) 251 – 280, 3% for DOY 281 – 310 and 1% for DOY 311 – 365.

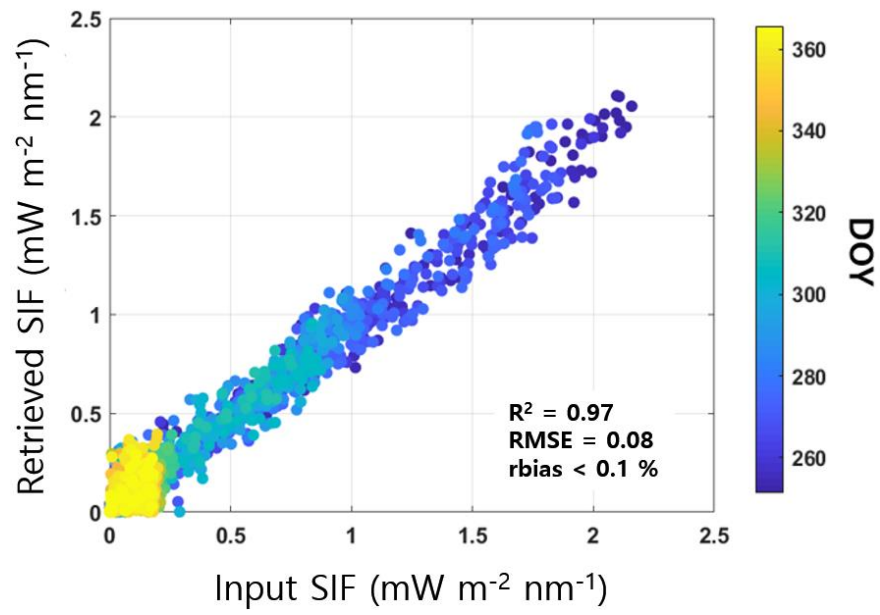


Figure. A1 Comparison between input and retrieved SIF

Appendix B. The relationships between SIF, GPP and APAR in sub daily time scale

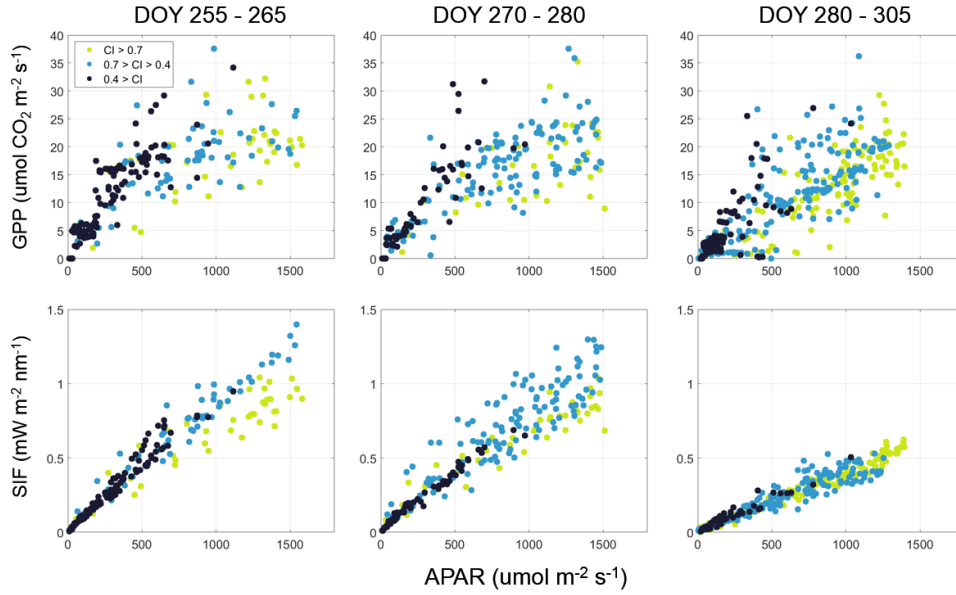


Figure. A2 Light response curves of GPP and SIF. CI indicates clearness index and each dot represents half-hourly data.

Appendix C. Diurnal variation of leaf-level quantum yield of photochemistry and steady-state fluorescence yield

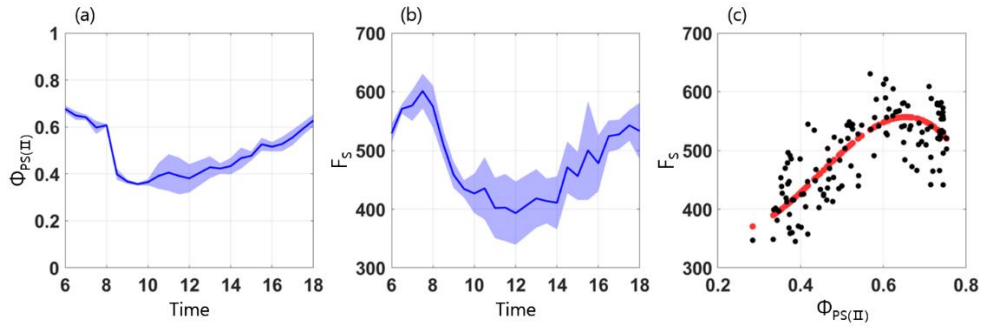


Figure. A3 Diurnal variation of leaf-level quantum yield of photochemistry ($\Phi_{PS(II)}$, (a)) and steady-state fluorescence yield (F_s , (b)) and scatter plot between $\Phi_{PS(II)}$ and F_s (c)

Appendix D. Leaf-level pigment analysis

To collect leaf-level pigment data, we collected 4 to 5 sunlit leaves and grouped them into one sample and collected more than three samples every 2 – 3 weeks during 2019 winter to early summer. We cut the needle leaves into 1cm long segments and stored the samples in liquid nitrogen immediately (within 10 sec) to prevent pigment changes. In the lab, we first measured weight of the leaf samples and then incubated the samples in the brown vial with 5ml Dimethyl Sulfoxide (DMSO) at 65 °C in water bath for 6 hours. After that, we transferred the incubated sample to 2.5 ml disposable cuvette and put in the spectrophotometer. To measure the chlorophyll and carotenoid pigment contents, we used empirical functions based on Wellburn (1994). We computed canopy-level CCI as an average for data when solar zenith angle is <70 degree.

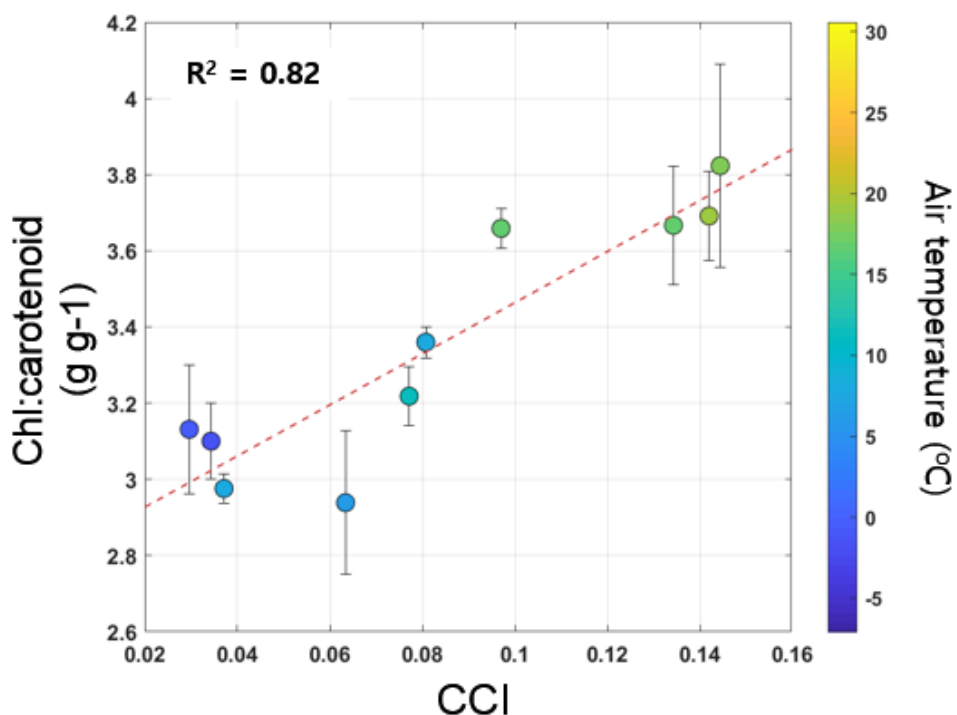


Figure. A4 Seasonal correlation between leaf-level Chl:carotenoid and canopy-level chlorophyll: carotenoid index (CCI)

Appendix E. The nomenclature and method used in this study.

Symbols	Definition (C = canopy-level, L = leaf-level)	Method
GPP	Gross primary productivity (C)	Observed
LUE_p	Light use efficiency (C)	Eq. 1
PAR	Photosynthetically active radiation (C)	Observed
APAR	Absorbed photosynthetically active radiation (C)	$PAR \times fPAR$
fPAR	Fraction of photosynthetically active radiation (C)	Observed
f_{esc}	Canopy escape fraction of the canopy (C)	Eq. 3
NDVI	Normalized difference vegetation index (C)	Eq. 4
NIR_V	Near-infrared reflectance of terrestrial vegetation (C)	$NDVI \times NIR_{ref}$
CCI	Chlorophyll: carotenoid index (C)	Eq. 5
SIF	Solar-induced chlorophyll fluorescence (C)	Observed
Φ_F	Chlorophyll fluorescence yield for canopy-level (C)	Eq. 2
Φ_{Fleaf}	Quantum yield of Chlorophyll fluorescence (L)	Table 1
$\Phi_{PS(II)}$	Quantum yield of Photochemistry (L)	Table 1
Φ_{sNPQ}	Quantum yield of Sustained NPQ (L)	Table 1

Φ_{rNPQ}	Quantum yield of Reversible NPQ (L)	Table 1
Φ_{D}	Quantum yield of Basal thermal energy dissipation (L)	Table 1
F_{mR}	Summer night reference measured for needles in the absence of sustained NPQ (L)	Observed
F_{s}	Steady-state fluorescence yield (L)	Observed
F'_{m}	Maximal fluorescence yield (L)	Observed
F_{m}	Maximal fluorescence yield in the night time (L)	Observed
F_{o}	Minimal fluorescence yield in the night time (L)	Observed

Chapter 4. Monitoring spring phenology of a multi-layer canopy in a deciduous broadleaf forest: What signal do satellites actually see?

1 Introduction

Monitoring spring phenology is crucial for understanding feedbacks of vegetation to climate system (Peñuelas and Filella, 2009). The leaf unfolding could influence the interaction between biosphere and atmosphere through energy exchanging, carbon cycling, water cycling (Bonan, 2008; Jeong et al., 2014; Keenan et al., 2014; Richardson et al., 2013a). The dates of leaf unfolding are strongly related to climate change, thus various studies have reported changes in spring phenology (Ettinger et al., 2020; Körner and Basler, 2010; Menzel, 2002; Menzel et al., 2006).

To monitor leaf-out and full-leaf dates, satellite remote sensing has been widely used. Satellite observations have the advantage that we can quantify vegetation changes in large areas without visiting the site (Richardson et al., 2013b), thus it is currently being used as the most useful tool to see vegetation changes since the 1970s (Piao et al., 2019). In particular, the normalized difference vegetation index (NDVI) from satellite imagery has been widely applied in the study of plant phenology to extract leaf-out and full-leaf dates (Helman, 2018). However, phenometrics detection based on satellite NDVI in deciduous broadleaf forest still has several important limitations.

Typically, deciduous broadleaf forests have multi-layer canopies, which implies increased complexity in both space and time.

In the forest, understory and overstory vegetation compete for light and interact with each other vertically, so they are located in a specific environment according to their physiological tolerance (Barbier et al., 2008; Liu et al., 2020). Even though the understory and overstory are experiencing almost the same climatic conditions, they have different spring phenology due to different growth strategies. For example, most of the understory vegetation species unfold leaves before the leaf-out dates of the overstory to absorb enough light energy for survival under the shadow from overstory in summer (Augspurger, 2009; Muller, 1978; Richardson and O' Keefe, 2009). However, when we see the forest from space by using satellites, the imagery contains a mixed signal of over- and understory. The seasonal pattern of NDVI observed from satellites could be changed when two or more species are overlapped (Badeck et al., 2004). This phenomenon could directly affect the leaf-out and full-leaf dates extracted from the satellite imagery. Ultimately, we have the following question: What phenology do we actually see from space compared to ground observations on multi-layer canopy phenology?

Research on the understanding of relationships between continuously observed multi-layer phenology in the ground and spring phenology extracted by satellite is still lacking. To monitor multi-layer phenology separately, numerous efforts have been made from the ground. Previous studies observed multi-layer phenology by visual inspection (Kim et al., 2021; Richardson and O' Keefe, 2009). Some studies also used RGB cameras to monitor multi-layer phenology. For example, Liu et al. (2021) installed trail cameras to monitor over- and understory phenology separately and Moore et al. (2017) installed two cameras to capture the changes of multi-layer

phenology. Furthermore, some studies tried to understand the satellite signal compared to in-situ observed multi-layer spring phenology (Nagai et al., 2014). In particular, one study compared MODIS leaf area index (LAI) products with in-situ observed plant area index from multi-canopies (Ahl et al., 2006), which showed that the understory development and temporal compositing of satellite data could make the difference between field observation and satellite estimation. Another study used low-cost spectral sensors to track multi-layer phenology and found that satellite NDVI could capture understory leaf unfolding in a deciduous broadleaf forest (Ryu et al., 2014). However, although observations of multi-layer phenology and comparisons with satellite products have been made, studies that continuously observed multi-layer phenology for a long period in the field and compared it with satellite-based phenology are still lacking. This limits our understanding as the responses of phenology to climatic variations can only be quantified based on sufficiently long time series.

Previous studies used inconsistent methods to extract leaf-out and leaf-full dates. Although several methods are developed to extract phenological events (White et al., 2009; Xie and Wilson, 2020), there are two approaches which have been broadly used to extract leaf-out and full-leaf date from satellite imagery. They include the vegetation growth curve (Zhang et al., 2003) and percentage of the vegetation growth amplitude (White et al., 1997). Both methods have the following advantages and disadvantages. The method based on vegetation growth curve fitting is ecologically meaningful and does not require pre-smoothing of data or a subjective threshold value (Zhang et al., 2003), but the logistic curve used in this approach could not fit well the seasonal dynamics of

vegetation in some region (Cao et al., 2015). The threshold method, on the other hand, is easy to use and it could be applied without considering vegetation growth trajectories. However, inconsistent threshold values could be arbitrarily selected to determine leaf-out dates and full-leaf dates. For example, threshold values of 10% (Jonsson and Eklundh, 2002), 15% (Moon et al., 2019), 20% (Wang et al., 2019; Yu et al., 2010), 30% (White et al., 2014), 50% (Bórnez et al., 2020; Bradley et al., 2007; White et al., 1997) have been used in previous studies. Therefore, further efforts are required to understand the difference between spring phenology from different phenology algorithm and in-situ observed leaf-out and full-leaf dates.

In this study, our objective is to investigate the relationships between multi-payer phenology and leaf-out and full-leaf dates from the curvature change rate and threshold methods. For comprehensive assessment of their relationships, we observed multi-layer phenology and relevant climate variables continuously during 2013 – 2020 in a deciduous broadleaf forest, South Korea. We installed low-cost multi-channel spectrometers above and below overstory allowed us to monitor over- and understory phenology independently, continuously. Our goal is to address the following scientific questions: 1) What is the difference between extracted satellite-based leaf-out and full-leaf dates according to different phenology algorithm? 2) How do satellite-based leaf-out and full-leaf dates relate to in-situ multi-layer phenology? 3) What are the implications of the difference between satellite-based and multi-layer phenology?

2 Materials and Methods

2.1 Study site

Our study sites is a deciduous broadleaf forest (DBF) in Gwangneung Experimental Forest which is located in the mid-western part of the Korean Peninsula (latitude: 37.748717N, longitude: 127.148176E, elevation: 260 m, slope: 10–20°). Annual maximum, minimum, and mean temperatures were 35, –15, and 10 ° C, respectively. Annual mean precipitation was around 1365 mm and mean annual gross primary productivity was around 1380 gC m^{–2} year^{–1} (Lee et al., 2020). Overstory canopy consisted of *Quercus acutissima*, *Quercus serrata*, and *Carpinus laxiflora*. The overstory species were old natural deciduous from 60 to 600 years old. Dominant understory species is deciduous including *Euonymus oxyphyllus* and *Cornus kousa*. The mean canopy height was about 18 m and maximum value of leaf area index (LAI) were around 5 – 6 in summer. We defined the overstory as trees higher than 10 m and understory as trees smaller than 10 m because the vertical variation of leaf area density was clearly divided by around 10 m based on a previous study (Figure 1, Song and Ryu (2015)).

2.2 Multi-layer spectral reflectance and transmittance measurement

To monitor over- and understory canopy phenology independently, continuously, we installed low-cost multi-channel spectrometers (LED sensors) on the 2m booms and installed the booms at 10 m and 22 m horizontally in a walkable 20 m high tower (Figure 14). The LED sensors measured spectral intensities in the bands of blue, green, red and near-infrared (NIR) (Ryu et al., 2014).

The LED sensors were covered by diffusers made out of Teflon material, so the field of view of sensor was approximately 180 degrees. For each height, we installed two pairs, upward- and downward-facing direction, to monitor the bi-hemispheric reflectance. All sensors were connected to a data logger (CR1000 Campbell Sci., Inc., CSI, Logan Utah) and we sampled the irradiance data every 30 seconds and stored half-hour mean values. We calculated daily dark current value which was measured during night time (22:00 – 03:00) and removed the dark current from observed digital number at each band for each day. To ensure long-term consistency of LED spectral data, we cross-calibrated the four bands of upward- and downward-facing LED sensors using a net radiometer (CNR4, Kipp & Zonen, the Netherlands). The net radiometer was installed at the 40 height of the tower 60 m from the LED installed tower. Although the wavelength range observed by LEDs and CNR4 were different and their relationships were non-linear, it was confirmed that there was no significant different from year to year (Figure. S1). In addition, we co-located all LED sensors at the top of the 20 m tower and installed them in the zenith direction and then cross-calibrated each spectral band in 2013 and 2015.

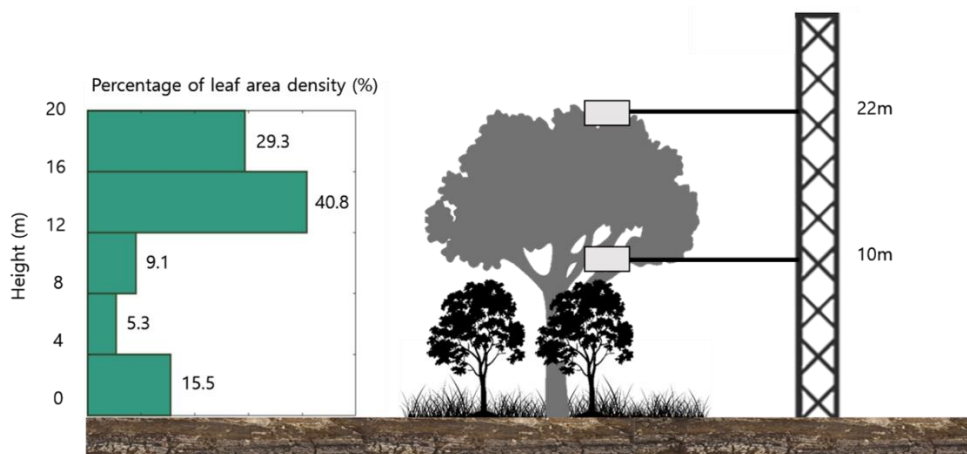


Figure 14) Experimental design at the deciduous broadleaf forest. White box

represent LED-sensors at 22 m and 10 m. The percentage of leaf area density data is from (Song et al., 2015).

We calculated reflectance of red and NIR by using upward- and downward-facing sensors at each layer. To compute daily reflectance value, we averaged the observed data when solar zenith angle (SZA) was lower than 70 degrees because the Teflon diffuse material had increased bias from the ideal cosine response curve when the SZA was larger than 70 degrees (Ryu et al., 2010) and the signal to noise ratio could be lower when the light condition was low. In addition, we applied the *Hampel* outlier filter to remove severe outliers in red and NIR reflectance (Hampel, 1974). We applied the filter with a three standard deviations and a window length of 2 days. By using daily averaged red and NIR band, we computed NDVI as bellow equation (Tucker, 1979).

$$\text{NDVI} = \frac{\rho_{\text{NIR}} - \rho_{\text{red}}}{\rho_{\text{NIR}} + \rho_{\text{red}}} \quad (\text{Eq. 1})$$

where ρ is spectral reflectance and NIR and red is daily mean NIR and red band reflectance.

To monitor overstory phenology, we measured transmittance of overstory canopy. We used blue band from upward-facing sensors at 22 m and 10 m as blue light minimizes canopy scattering effects that can bias gap fraction estimation (Brusa and Bunker, 2014). To obtain relative large footprint and reduce variation in daily transmittance data, we chose measured data under diffuse sky condition to avoid heterogeneities in the radiation field that can be caused by sun flecks. We used clearness index, which is ratio of PAR above the canopy to the PAR at top of atmosphere, to define diffuse sky condition. We defined the diffuse sky condition when clearness

index was below 30 % threshold in the sorted half-hourly clearness index based on observed PAR data when SZA was less than 70. We applied a *Hampel* outlier filter in the same way as the reflectance to remove severe outliers. In addition, we removed daily mean data when light conditions were extremely low because as these conditions can lead to outliers. We defined the low light condition day as daily mean clearness index was below 30 % threshold in the sorted daily clearness index during whole observation period.

2.3 Phenometrics detection

We evaluated the widely used two phenology algorithm as 1) curvature change rate method and 2) threshold method with NDVI observed above top of the canopy. Before using both methods, we fitted the observed NDVI using the logistic function as below.

$$Y = a + \frac{b}{1 + \exp(c - dx)} \quad (\text{Eq. 2})$$

where a, b, c and d are parameters, x is day of year and y is observed NDVI above top of the canopy.

For the curvature change rate, we calculated the second-order derivative of the fitting curve and we defined the leaf-out date and full-leaf dates as the first and second peak of NDVI of the second order derivative curve (Figure. S2). In case of the threshold method, we calculated the corresponding day of year (DOY) by applying different threshold values to logistic fitted NDVI. Previous studies applied cubic splines or normalized NDVI and then a dates corresponding to the threshold were selected because satellite products had a lot of data gaps and noise in seasonal pattern, thus strict fitting methods were required (Moon et al., 2019; Wang et al., 2019; White et al., 1997). In our study, we used logistic fitting

method because 1) there was less noise and data gaps in LED data and 2) to do the same comparison with the curvature change rate method.

To quantify the uncertainty of spring phenology from both phenology algorithm, we processed the data in the following way based on a previous study (Ryu et al., 2014). First, we calculated uncertainty in four parameters (a , b , c , d , in Eq.2) by using non-linear regression parameter confidence interval function (*nlparci* function) in MATLAB (MathWorks Inc., Natick, MA, USA). Second, we made 10,000 samples by using multivariate normal random numbers (*mvnrnd* function in MATLAB) based on the uncertainty in four parameters from *nlparci* function. After that, we fitted the logistic curve with random samples and extracted leaf-out and full-leaf dates from the two phenology algorithm. Finally, we could calculate error range as three standard deviation of the extracted whole leaf-out and full-leaf days.

2.4 In-situ multi-layer phenology

In this study, we derived in-situ multi-layer phenology from LED data collected from 10 m and 22 m heights. We used NDVI data collected at 10 m height to monitor in-situ understory phenology and the used 1-transmittance data in overstory canopy to extract in-situ overstory phenology. In a previous study (Ryu et al., 2014), the leaf-out dates were defined as the date when 50 % of new leaves were over 1 cm and full-leaf date was defined as the dates when the leaves size was around 70 % of the full-leaf size in our site. Based on previous in-situ observed data, we determined the best method for estimating in-situ leaf-out and full-leaf dates of under- and overstory at our site as follows. For in-situ leaf-out and full-leaf

dates of understory canopy, we used observed NDVI data collected at 10 m LED sensor. To extract understory leaf-out dates, we fitted observed NDVI using the logistic function and then we generated the second-order derivative fitting curve. After then we determined leaf-out as DOY at the peak of second-order derivative fitting curve. To extract understory full-leaf dates, we used a threshold method (80 %) based on the fitted NDVI data. For overstory leaf-out and full-leaf dates, we used the 1-transmittance data from 10 m and 22 m upward-facing blue LEDs. First, we calculated 1-transmittance value (i.e. absorptance without reflectance) and then we fitted them with the logistic function. Second, we used a threshold method (20 % for leaf-out dates and 70 % for full-leaf dates) to extract in-situ overstory leaf-out and full-leaf dates. We selected the fitting method and threshold value for understory and overstory leaf-out and full-leaf dates based on Ryu et al. (2014). In Ryu et al. (2014), leaf-out date was defined as the date when 50 % of new leaves were around 1 cm and full-leaf date was defined as the date when 70 % of full-leaf size. We confirmed that our threshold methods could track well visual observed multi-layer phenology (reference in-situ dates were from Ryu et al. (2014)) as bias were less than 2 days for under- and overstory leaf-out and full-leaf dates. To compute range of the error, we made 10,000 random samples as reported in the chapter of 2.3, and calculated one standard deviation of the extracted whole leaf-out and full-leaf days. In addition, we used the data collected from one camera with fisheye lens at around 16 m height to confirm that our methods of estimating in-situ leaf-out and full-leaf dates in the overstory canopy were correct. Through the installed camera, we were able to continuously check under- and overstory changes visually and we confirmed the difference in multi-

layer phenology by years (Figure. A1).

2.5 Satellite remote sensing data

We used MODIS satellite products (MOD09GQ, MYD09GQ and MCD43A3) and Landsat 8 surface reflectance product to understand satellite NDVI based phenology. The MOD09GQ is daily Terra surface reflectance product and the MYD09GQ is daily Aqua surface reflectance product (Vermote and Wolfe, 2015). Both products have 250 m spatial resolution. MCD43A3 daily surface reflectance data set is adjusted for viewing geometry using the bidirectional reflectance distribution function and it has 500 m spatial resolution (Schaaf and Wang, 2015). Landsat 8 product is atmospherically corrected surface reflectance from the OLI/TIRS sensors and it has 30 m spatial resolution (Vermote et al., 2016). For MOD09GA and MYD09GQ, we downloaded the data via global subsets tool (DAAC, 2018). We chose highest quality data (no cloud, low or average of aerosol quantity, not adjacent to cloud) based on MODLAND QA bits from MO(Y)D09GA products. In case of the MCD43A3 and Landsat 8 surface reflectance products, we used Google Earth Engine to extract surface reflectance and NDVI. We selected one pixel which includes the tower location.

2.6 Meteorological variables

We measured air temperature (HMP-35; Vaisala, Helsinki, Finland) and PAR (L180; LICOR) at the top of the 40 m tower with a net radiometer also installed. In addition, we measured the air temperature at above (10 m) and below (30 m) the overstory canopy.

To quantify thermal requirement for leaf-out, we calculated growing degree days (GDD) as follows:

$$\text{GDD} = \frac{T_{\max} + T_{\min}}{2} - T_{\text{base}} \quad (\text{Eq. 3})$$

Where T_{\max} and T_{\min} are maximum and minimum air temperature during one day. T_{base} is optimal base temperature and it is usually determined experimentally based on life cycle. Here, we adopted the T_{base} as 5 °C for under and overstory based on a previous study (Prentice et al., 1992). The accumulated GDD (AGDD) was sum of GDD during preseason. We determined the preseason length as from DOY 1 to 91 because the understory leaves have not yet unfolded during this period. We used the fixed preseason length because the over- and understory species did not change much during whole observation period (2013 – 2020 spring). We defined the chilling days based on a widely used method as when the daily mean temperature was lower than 5 degree (Fu et al., 2015). The number of accumulated chill days (NCD) was defined as the sum of number of chilling days during preseason period.

3 Results

3.1 Seasonal to interannual variations of NDVI, 1-transmittance, and air temperature

NDVI from 22 m and 10 m LEDs, 1 – transmittance, and air temperature showed distinct seasonal patterns in the study site (Figure. 15). NDVI from 22 m and 10 m LED increased rapidly in the spring season (around DOY 100) and decreased in autumn (around DOY 300). In addition, we could see that satellite products (Landsat 8 and MO(Y)D09GQ)-based NDVI exhibited strong seasonality similar to NDVI from 22 m LED (Figure. 15a). The 1 – transmittance was more scattered than NDVI, but it had similar seasonal pattern with NDVI (Figure. 15c). Air temperature was minimum -17.9 °C

and the maximum 30.7 °C, and it increased and decreased gradually, not rapidly like NDVI and 1 – transmittance.

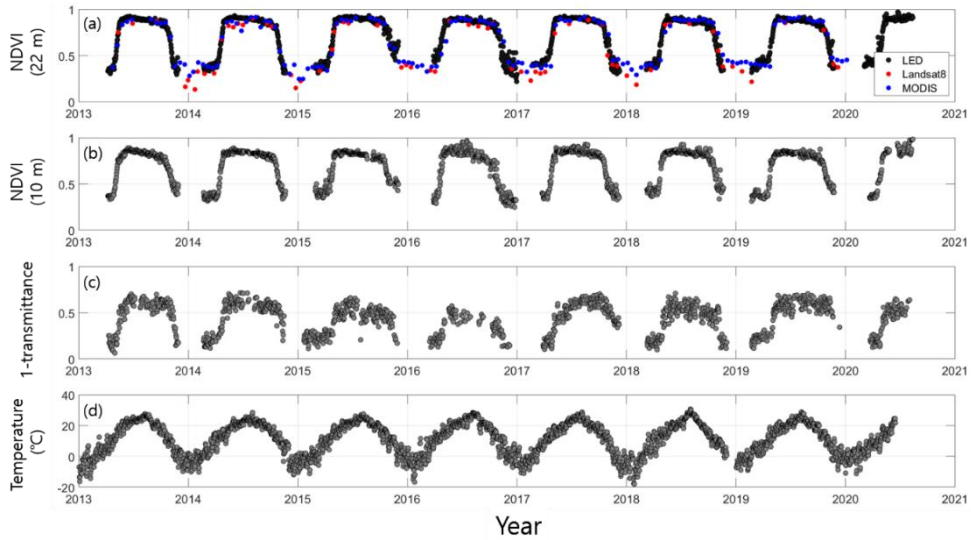


Figure 15) Inter-annual and seasonal variation in field-measured daily multi-layer NDVI, 1-transmittance, air temperature and satellite products (Landsat8 and MODIS; MO(Y)D09GQ)

NDVI from 22m LED and satellites-based NDVI agreed well (Figure. 16). The NDVI from 22 m LED and satellite-based NDVI that combines NDVI of Landsat8, MOD09, MY09 and MCD43 had Pearson correlation coefficients (R^2) of 0.94 and root mean square error (RMSE) of 0.04. Overall, magnitude of satellite-based NDVI was similar to NDVI from LED 22 m as bias was -0.03 . In addition, we found strong linear relationships between the individual satellite NDVI and the NDVI from 22 m LED (R^2 of 0.85, 0.96, 0.96, 0.94 and bias of -0.05 , -0.03 , -0.04 , and -0.03 for Landsat8, MOD09, MYD09 and MCD 43, respectively).

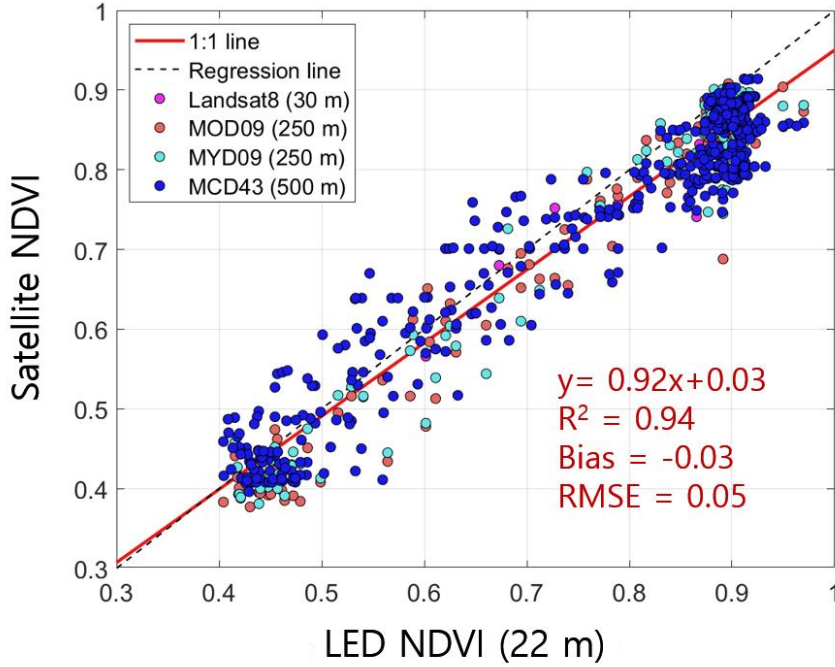


Figure 16) Scatter plot between MODIS and Landsat8-based NDVI and NDVI from LED 22 m. For satellite NDVI, we used Landsat8 (30 m, spatial resolution), MOD09 (250 m), MYD09 (250 m) and MCD43A4 (500 m) products. The linear regression line was calculated by the relationship between satellite NDVI from whole products and NDVI observed by LED 22 m.

3.2 Inter-annual variation of leaf-out and full-leaf dates

We found that leaf-out dates detected from LED data in 22 m using 10 % threshold method and curvature change rate method showed similar magnitudes and inter-annual variations with in-situ understory leaf-out dates (Figure. 17). The bias between the leaf-out dates from 10 % threshold method and the curvature change rate method was 0.37 days. The leaf-out dates from 10 % threshold method had strong correlation with the leaf-out dates from curvature change rate method ($R^2 = 0.99$). We also found that in-situ understory leaf-out dates were very similar to the leaf-out dates

from the 10 % threshold method (R^2 of 0.86, bias = -1.1 days) and leaf-out dates from the curvature change rate method (R^2 of 0.87, bias = -0.75 days).

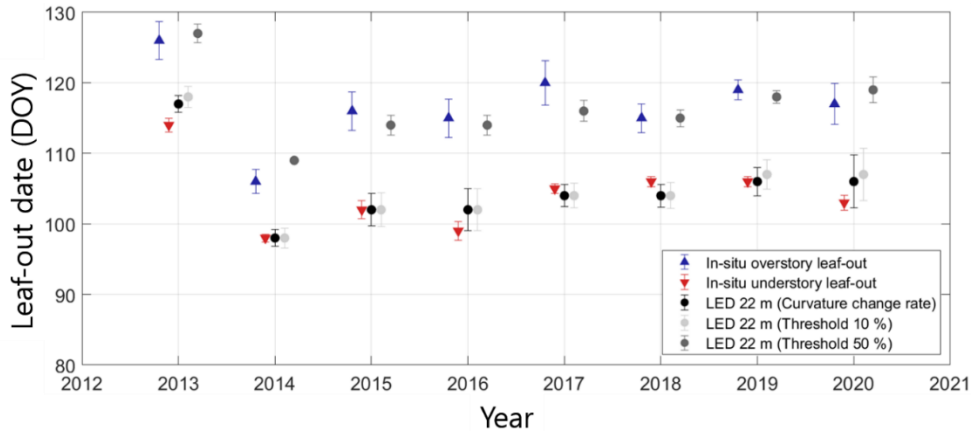


Figure 17) Annual leaf-out dates from understory, overstory, LED 22m with different phenology algorithm

In case of the full-leaf dates, the relationships between in-situ multi-layer, threshold and curvature change method-based full-leaf dates were complex. The dates calculated using the 70 % threshold method using NDVI from 22 m LED showed similar magnitude to the in-situ understory full-leaf dates ($R^2 = 0.93$, bias = -0.5 days, Figure. 18). The dates calculated using the 90 % threshold method using NDVI from 22 m LED showed similar magnitude to the in-situ overstory full-leaf dates ($R^2 = 0.8$, bias = -1.7 days) and full-leaf dates from curvature change rate method (R^2 of 0.81, Bias = -2.1 days).

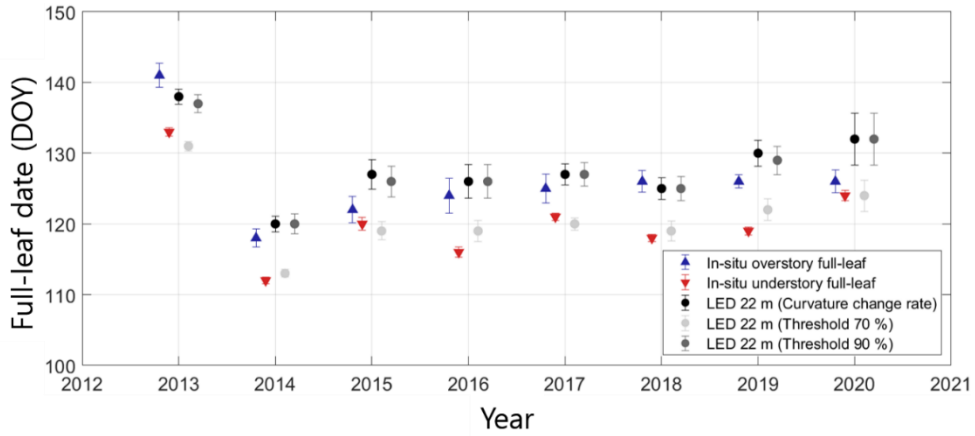


Figure 18) Annual full-leaf dates from understory, overstory, LED 22m with different phenology algorithm

3.3 The relationships between dates calculated according to threshold and in-situ multi-layer phenology

According to threshold value, we found that the extracted leaf-out and full-leaf dates showed various bias and R^2 with in-situ multi-layer phenology. We found that bias was lowest with under- and overstory leaf-out dates and under- and overstory full-leaf dates when thresholds were 8 %, 50 %, 70 %, and 87 %, respectively. Overall, threshold-based dates had high R^2 with understory leaf-out dates and full-leaf dates rather than overstory (Figure. 19b). In case of the leaf-out dates, threshold-based dates showed increased R^2 with overstory leaf-out dates as the threshold value increased, and R^2 was decreased with understory leaf-out dates. When the threshold was from 35 % to 50 %, threshold-based dates had slightly higher R^2 with overstory leaf-out dates than understory leaf-out dates. In case of the full-leaf dates, threshold-based dates had constant R^2 with understory full-leaf dates as the threshold increased, while R^2 with overstory full-leaf dates was decreased

gradually.

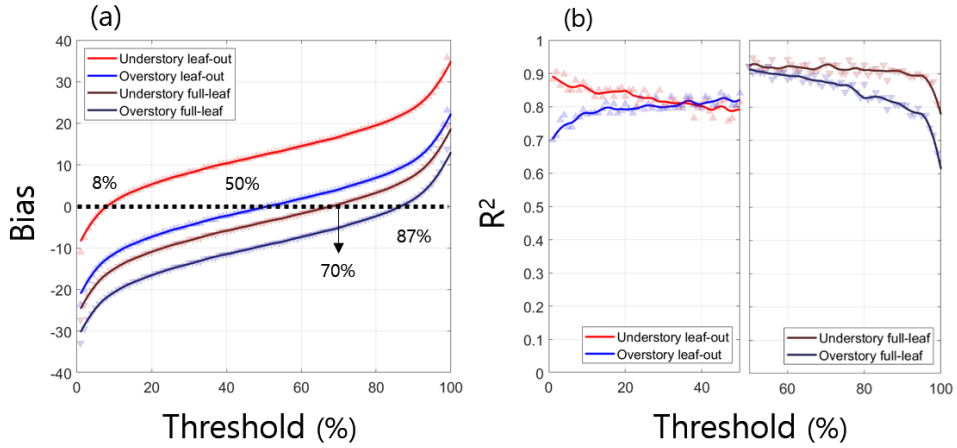


Figure 19) The bias (a) and R^2 (b) between observed leaf-out dates and full-leaf dates of multi-layer canopy and leaf-out dates and leaf-out dates calculated over the threshold changes

3.4 The relationship between multi-layer phenology, AGDD and NCD

In-situ understory and overstory leaf-out dates showed different relationships with AGDD and NCD (Figure. 20). Overstory leaf-out dates had a strong negative linear relationship with AGDD ($R^2 = 0.86$). Understory leaf-out dates also had a negative linear relationship with AGDD, but there were some differences as understory leaf-out dates showed lower R^2 with AGDD than overstory ($R^2 = 0.69$) and the sensitivity was also slightly lower. The slope between AGDD and overstory leaf-out dates was -0.19 and understory was -0.15 (both p -values < 0.05). In relation to NCD, leaf-out dates of understory showed significant relationship with NCD (p -value < 0.05) and overstory leaf-out date had no significant relationship with NCD (p -value > 0.1). Understory leaf-out dates showed high R^2 ($R^2 = 0.49$) with NCD and the sensitivity

was also different between under- and overstory as the slope between the understory leaf-out dates and NCD was 0.96 and the slope of the overstory was 0.7.

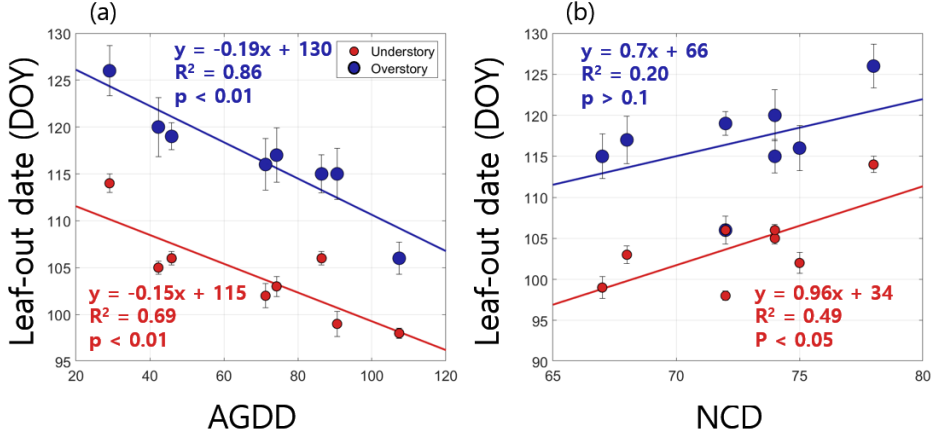


Figure 20) Relationships between leaf-out dates of over-, understory, and accumulated growing degree days (AGDD) (a) and number of accumulated chill days (NCD) (b). To avoid overlapping point between overstory and understory leaf-out dates, we used different size of the symbols.

4 Discussion

In this study, we comprehensively investigated the relationships between satellite-based and in-situ multi-layer spring phenology. In addition, we explored the relationships between leaf-out and full-leaf dates calculated by the different phenology algorithm including curvature change rate, threshold percentage, and the in-situ multi-layer phenology. We assumed that the NDVI from 22 m LED which was installed above overstory serves as the proxy of the satellite-based NDVI because 1) NDVI from 22m LED was strongly correlated to satellite-based NDVI (Figure. 16) and 2) NDVI from 22 m LED has fewer data gaps compared to satellite products (Figure. 15), so leaf-out and full-leaf dates based on NDVI

from 22m LED could have relatively less uncertainty than dates calculated by using satellite-based NDVI. We found that the understory leaf-out dates were similar to satellite-based leaf-out dates and satellite-based leaf-out and full-leaf dates calculated by threshold method showed different R^2 and bias with multi-layer phenology according to threshold value. In addition, the under- and overstory leaf-out dates showed different responses to temperature. Here we provided a detailed discussion of the answers to the questions presented in the introduction.

4.1 How do satellite-based leaf-out and full-leaf dates differ from in-situ multi-layer phenology?

The satellite-based leaf-out dates were more strongly related to understory than overstory in a deciduous broadleaf forest. Satellite-based leaf-out dates showed similar inter-annual variation and magnitude to understory leaf-out dates (Figure. 17). Regardless of the phenology algorithm, both the curvature change rate and threshold 10 % were similar to the in-situ understory leaf-out dates (Curvature change rate method: $R^2 = 0.87$, bias = -0.75 , threshold 10 %: $R^2 = 0.86$, bias = -1.12). Although the amount of LAI in the understory vegetation accounts for only 30 % of total LAI, it seems that the signal of understory could strongly affect the satellite-based leaf-out signal because overstory LAI was around zero at the time of the understory leaf-out. This results are similar to the results of previous studies. Ahl et al. (2006) found that the MODIS LAI product was earlier than the in-situ overstory LAI and explained that the understory components may have influenced the satellite signal. Ryu et al. (2014) found that in-situ understory leaf-out date was similar to leaf-out date from MODIS NDVI, while overstory leaf-out dates

were about 13 days later. The previous study only looked at single year of data, while we found that a consistent bias across 8 years.

The relationships between satellite-based full-leaf dates and in-situ multi-layer phenology were complex. The satellite-based full-leaf dates using the curvature change rate method were similar to the threshold of 90 % and in-situ overstory full-leaf dates (Figure. 18). When we averaged 8 years data, we could see that satellite-based full-leaf dates from curvature change rate was similar to overstory full-leaf dates clearly (Figure. S2). Satellite-based full-leaf dates could be related to mixture of understory and overstory signal because satellite-based full-leaf dates were later than overstory leaf-out dates (Figures. 17 and 18). Understory full-leaf dates were earlier than overstory full-leaf dates by 5.6 days, and 7.7 days earlier than satellite-based full-leaf dates using the curvature change rate method (Figure. 18). In satellite view, the influence of overstory full-leaf dates could be larger than understory because the overstory LAI is more than three times larger than understory LAI at maturity (Figure. 14).

Satellite-based full-leaf dates based on threshold method had higher R^2 with understory full-leaf date than overstory full-leaf dates regardless of the threshold % (Figure. 19). This phenomenon can be verified through simulation (Figure. A2). In simulation, we fixed full-leaf dates as DOY 120 and leaf-out dates were adjusted at 5-days interval from DOY 70 to 95. After then we checked the extracted dates from curvature change rate and 10%, 90 % threshold method. Although we fixed full-leaf dates, we found that full-leaf dates from threshold method were increased according to the increased leaf-out dates (Figure. A2). On the other hand, there were no changed in the full-leaf dates from curvature change rate method.

Understory leaf-out dates and full-leaf dates could be strongly correlated (Richardson et al., 2010) and satellite-based leaf-out dates could be influenced by understory leaf-out dates (Figure. 17). Threshold-based full-leaf dates could be affected by leaf-out dates (Figure. A2), thus threshold-based full-leaf dates using satellite NDVI had high R^2 with understory full-leaf dates. Therefore, estimated full-leaf dates could be affected by used phenology algorithm and we should be careful this when interpreting the full-leaf dates.

Although it is challenging to compare satellite imagery and field observed data, our results are reliable for the following reasons. We used NDVI value observed by top of the canopy LED to understand satellite-based leaf-out and full-leaf dates because the satellite products had considerable data gaps and the data gaps could affect extracted leaf-out dates (White et al., 2014). In observed LED data, there were fewer data gaps (only less than 5 days during from DOY 60 to 180) compared to satellite products (Figure. 15a). Overall, inter-annual and seasonal pattern of satellite-based and LED-based NDVI was well matched (Figure. 15a) and LED-based NDVI was highly correlated with satellites with various spatial resolutions ($R^2 = 0.94$, $RMSE = 0.04$, Figure. 16). Furthermore, the spatial heterogeneity of the canopy in our site is relatively low as there was no significant difference between the averaged NDVI from one and four pixel of MODIS and corresponding averaged NDVI of the pixels of Landsat (Ryu et al., 2014). We also confirmed that there was no significant difference (bias = -1.13 days) between the satellite-based leaf-out and LED (22 m) NDVI-based leaf-out dates (Figure. A3).

4.2 Are the 10 % and 90 % thresholds from satellite-based NDVI always well matched with the leaf-out and full-leaf dates calculated by the curvature change rate?

We found that 10 % and 90 % thresholds based on NDVI from LED 22 m were most closely matched with leaf-out and full-leaf dates calculated by curvature change rate method (Figure. 17 and 18). Threshold 10 % and 90 % had 0.38 days bias with curvature change rate-based leaf-out and full leaf dates. These results are similar to previous studies. According to Shang et al. (2017), the leaf-out dates from 9.18 % threshold method showed similar dates with curvature change rate method-based leaf-out dates. Although the mixture of grassland and forest could not be fitted well with logistic fitting method (Cao et al., 2015; Shang et al., 2017), their threshold value was similar with ours.

If so, are the 10 % and 90 % thresholds based on NDVI from LED 22 m always similar to the leaf-out and full-leaf dates calculated by the curvature change rate? At our site, there were no differences in the curvature change rate-based leaf-out and full-leaf dates and 10 % and 90 % threshold during 8 years (Figure. 17 and 18). The leaf-out dates differed only by one day in 2013, 2019 and 2020. However, the difference between dates from two methods could be changed depending on the growth rate of vegetation. In our simulation results, the difference between leaf-out dates from both methods were larger when the spring growth rate was lower (Figure. A2). These results mean that the threshold value with the same leaf-out date as the curvature change rate method could vary depending on vegetation growth rate. In addition, we found that threshold-based full-leaf dates were strongly affected by leaf-out dates, while curvature change rate method did not. These results suggest that

type of variables used for phenology detection could also make the difference between extracted dates from threshold and curvature change rate methods. For example, canopy structure information (e.g. LAI), carbon flux (e.g. gross primary productivity (GPP)) and vegetation indices showed different spring growth rate even in the same site (White et al., 2014). In some sites, canopy structure and carbon flux increased more slowly than vegetation indices (Soudani et al., 2021a). Therefore, it is necessary to carefully consider and select a phenology algorithm according to the site characteristics and the used variables.

4.3 What are the implications of the difference between satellite-based and multi-layer phenology?

In-situ understory and overstory leaf-out dates responded to AGDD and NCD differently (Figure. 20). For AGDD, overstory leaf-out showed a stronger negative relationship than understory (Figure. 20a). On the other hand, understory showed a stronger positive correlation with NCD and overstory showed less correlation with NCD (Figure. 20b). In addition, Overstory leaf-out dates responded more sensitively to AGDD and the understory leaf-out dates were more sensitive to the NCD (Figure. 20). In the case of 2013, we found that overstory leaf-out date had a low correlation with NCD compared to other years. (Figure. 20b). Even if we remove the 2013 data, the difference between overstory and understory leaf-out dates with NCD did not change significantly as the overall relationship between overstory leaf-out dates and NCD was R^2 of 0.4 (p-value > 0.1) and slope was 0.63 after removing 2013 data. The difference in response to temperature between under- and overstory species could be related to evolutionary aspects. In most

deciduous forests, understory species had earlier leaf-out dates than overstory species (Augspurger, 2004; Augspurger and Bartlett, 2003; Gill et al., 1998; Richardson and O' Keefe, 2009; Seiwa, 1999). Understory have earlier leaf expansion in spring to avoid shade from overstory leaves. Extending the understory phenology by avoiding the shadow of the overstory leaves allows understory vegetation to maximize light absorption and used for energy to persist under overstory shade during the summer (Augspurger et al., 2005; Gill et al., 1998; Kwit et al., 2010; Seiwa, 1999; Vitasse, 2013). At the same time, understory are more likely to be exposed in the early spring frost (Augspurger, 2013; Hufkens et al., 2012; Vitasse et al., 2014). Therefore, to protect their leaves from spring frost, understory should respond sensitively to chill, thus understory leaf-out dates had strong positive correlation and sensitivity with NCD (Figure. 20b). On the other hand, the overstory showed relatively weaker relationship with NCD because the overstory leaves emerge later and there is less possibility to be exposed to spring frost.

What are the implications of different temperature responses of understory and overstory leaf-out? We found that satellite-based leaf-out dates tracked understory leaf-out dates (Figure. 17). In addition, we found that overstory was more sensitive to temperature increase than understory (Figure. 20). These results suggest that we need to be more careful in predicting total amount of carbon uptake from vegetation changes using satellite products. For example, numerous previous studies reported that the total amount of carbon uptake via photosynthesis could be increased because satellite-based leaf out dates are getting earlier and growing seasons are getting longer (Myneni et al., 1997; Peñuelas and Filella, 2009; Peñuelas et al., 2002; Piao et al., 2006; Piao et al., 2019).

Based on our data, we suggest that the amount of carbon uptake in deciduous forest may increase faster than previous expectation. In deciduous forest, the amount of LAI in the overstory is larger than the understory LAI and the amount of overstory photosynthesis is larger than understory generally (Misson et al., 2007; Muraoka et al., 2008; Sampson et al., 2006). In our site, the overstory responds more sensitively to GDD, thus the leaf-out time of overstory is advanced earlier than that of understory according to warming. Therefore, overstory leaf-out dates, which have a greater impact on carbon uptake than leaf-out we see by using satellites, are changing more rapidly to climate change and it means that carbon uptake may increase faster than expected.

4.4 Limitations and Implications for future studies

Fewer studies have presented in-situ autumnal phenological events compared to spring phenology. The mechanisms and trends in response to temperature changes during senescence period are still not well known due to lack of research (Piao et al., 2019). Furthermore, there were difficulties in interpreting the autumn data observed in the field. For example, in this study, we only investigated the relationship between ground- and satellite observation during spring period for the following reason. We defined the in-situ spring phenology of overstory using transmittance data and used NDVI for in-situ spring phenology of understory. In spring, detecting phenometrics using transmittance and NDVI had relatively small differences compared to senescence period (Soudani et al., 2021a). On the other hand, in the senescence period, NDVI and transmittance could show a distinct difference. For example, the dominant overstory species on our site exhibits marcescence which is that

withering of the leaves on trees without leaf-fall and abscission (Abadía et al., 1996). Therefore, transmittance had high magnitude consistently during senescence period compared to NDVI because the leaves hung on the tree. This phenomenon causes difficulties in determining leaf-fall dates by using transmittance.

Additional in-situ multi-layer phenology observation-based studies are needed to understand and interpret satellite-based phenology. We observed multi-layer phenology over 8 years and revealed that satellite-based leaf-out dates were mostly determined by understory unfolding (Figure. 17) and full-leaf dates were mostly related to overstory phenology (Figure. 18). However, we are aware of the limitation that we observed only a single site. Although the observed overstory dominant species in this study accounts for around 24.2 % of the forests in South Korea, the spring phenology of overstory could differ according to location and environmental conditions (Migita et al., 2007; Nakajima et al., 2012). In addition, the vertical and horizontal vegetation profiles of the ecosystem could be different depending on the land cover type. For example, understory accounts for a significant portion of the total vegetation in the savannah (Moore et al., 2016). In evergreen needleleaf forest, where the overstory is formed at high density, the question remains whether the understory unfolding could affect the satellite-based leaf-out dates. To understand the relationship between multi-layer and satellite-based phenology with high spatiotemporal resolution in various sites, recently developed low-cost near surface sensors could be helpful (Kim et al., 2019; Ryu et al., 2010; Soudani et al., 2012). The in-situ observed multi-layer phenology can be used to validate satellite-based multi-layer phenology detection method. Recently, method for estimating background reflectance using the

ratio of bidirectional reflectance distribution function and albedo data (Pisek et al., 2021) or estimating understory and overstory LAI using multi-angle imaging spectroradiometer (Liu et al., 2017) or estimating phenometrics using synthetic aperture radar (Soudani et al., 2021b) have been developed, but sufficient verification has not been made yet.

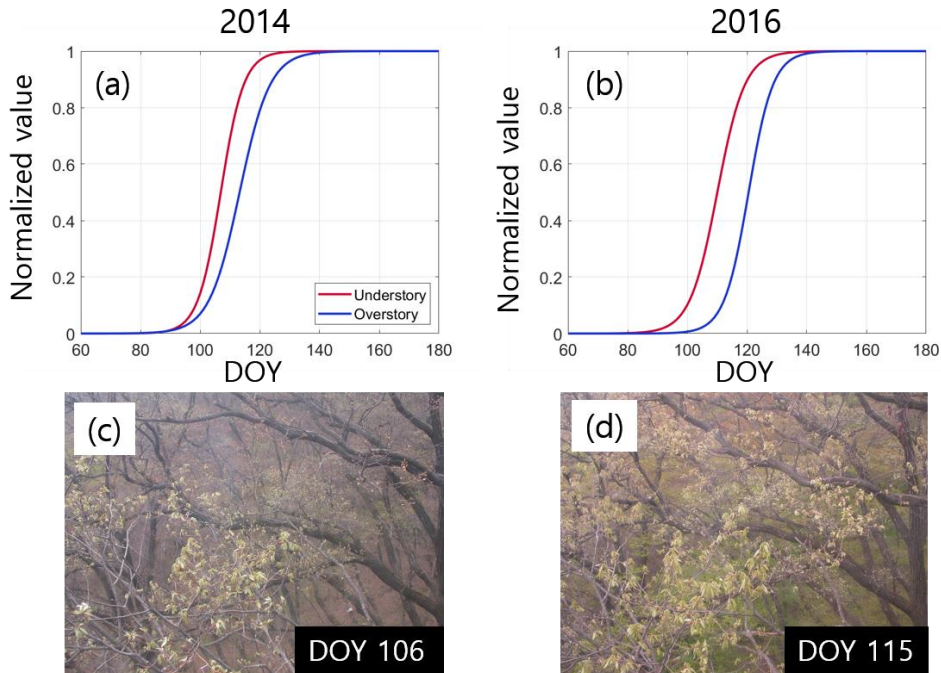
Conclusion

In this study, we comprehensively investigated the relationship between in-situ multi-layer and satellite-based phenology. We installed multi-channel spectrometers at above and below overstory canopy to monitor over- and understory canopy phenology separately. Our analyses resulted in three main findings. First, satellite-based leaf-out dates were strongly related to understory leaf-out dates while satellite-based full-leaf dates were related to overstory full-leaf dates. Second, depending on the threshold % and vegetation growth rate, the leaf-out and full-leaf dates calculated by the curvature change rate and threshold method are different. Third, overstory- and understory leaf-out dates showed different responses to temperature as overstory leaf-out dates were strongly correlated to AGDD while understory leaf-out dates were less strongly related to AGDD and also sensitive to NCD. Overall, these results suggested we need to be more careful in interpreting climate change-related vegetation changes based on satellite observations. The satellite-based spring phenology may have different results depending on which phenology algorithm was used based on our results. Furthermore, satellite-based leaf-out and full-leaf dates were mixture of understory and overstory signals, thus which vegetation layer affected the satellite observation signal

should be sufficiently considered when we explore the relationship between satellite-based spring phenology and climate changes.

Appendix A. Image-based multi-layer phenology monitoring

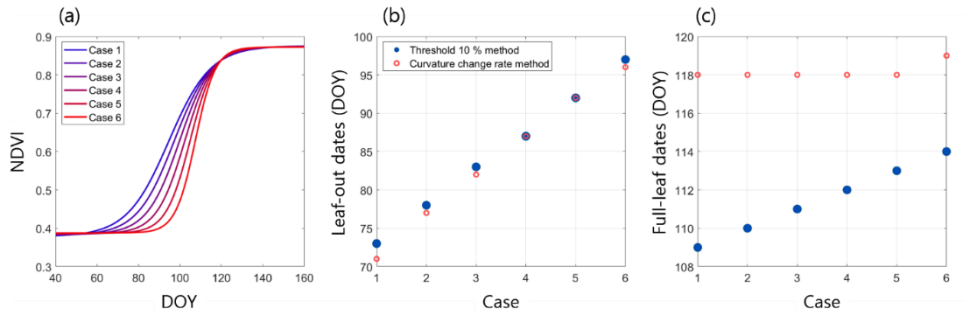
To monitor the seasonal variation of multi-layer canopy phenology, camera (Nikon Coopix 4500; Nikon, Tokyo, Japan) was installed with fisheye lens (FC-E8; Nikon) at 18 m height on same tower with LED sensors (Choi et al., 2011). The camera was connected to a laptop using a LAN cable, thus the image files were stored in the laptop in JPEG format automatically. The camera was set to take pictures with one hour interval from 0900 to 1700. We visually confirmed whether the extracted multi-layer leaf-out dates were consistent with the collected photos. For example, the greenness of the understory (background color) was clearly different in 2014 and 2016 even though the overstory leaf-size was similar in 2014 and 2016 (Figure. A1).



A1) The fitted curve of overstory ($1 - \text{transmittance}$) and overstory (NDVI) in 2014 (a) and 2016 (b) and collected images at overstory SOS in 2014 (c) and 2016 (d). We could see leaf size of overstory was similar in both images, but the understory (background) was much greener in 2016 because the days between understory SOS and overstory SOS was longer in 2014

Appendix B. Simulation of spring phenology detection

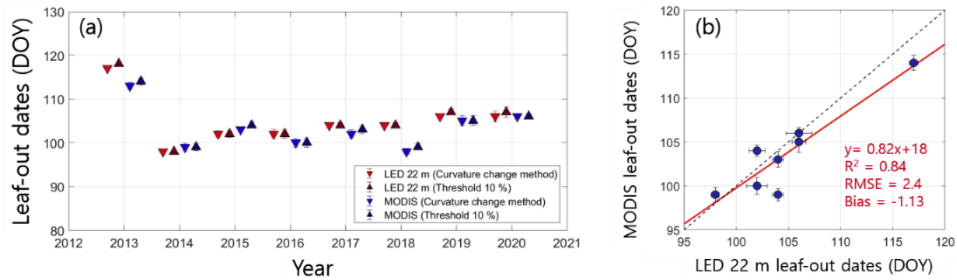
We simulated phenological green-up curve of NDVI to understand the difference between threshold method and curvature change rate method. We fixed full-leaf date at DOY 120 and changed the leaf-out dates from DOY 70 to DOY 95 with 5-days interval. After then we fitted the NDVI value using logistic fitting method (Fig. A2a) and applied threshold 10 %, 90 % and curvature change rate method (Figure. A2b and c). In case of the leaf-out dates, threshold 10 % and dates from curvature change rate method were increased according to delayed leaf-out dates (Figure. A2b). On the other hand, the two methods showed different results for full-leaf dates. The full-leaf dates based on threshold method were affected by leaf-out dates. The full-leaf dates based on the threshold 90 % were increased continuously as the leaf-out dates increased. However, the full-leaf dates from the curvature change method showed a constant value except case 6 (Figure. A2c).



A2) Simulated phenological green-up curve of NDVI (a) and leaf-out dates and full-leaf dates from threshold and curvature change rate method (b and c).

Appendix C. Comparison between leaf-out dates from MODIS NDVI and LED NDVI

In this study, we used NDVI observed by LED 22 m to understand satellite-based spring phenology. In addition, we confirmed that LED 22 m-based NDVI and satellite-based NDVI (MODIS and Landsat) had strong linear correlation ($R^2 = 0.94$, Figure. 3). We additionally confirmed that the LED- and satellite-based leaf-out dates were significantly correlated (Figure. A3). We fitted MODIS MCD43 product (500m spatial resolution) using logistic fitting method and then calculated leaf-out dates using 10 % threshold and curvature change rate method. During 8 years, the relationship had R^2 of 0.84 and bias was -1.13 day. In 2018, we found that MODIS product showed much earlier leaf-out dates compared to LED-based. Except 2018, R^2 was 0.94 and bias was -0.58 .



A3) Annual MODIS NDVI based leaf-out dates and LED NDVI leaf-out dates (22 m) (a) and scatter plot between MODIS NDVI leaf-out dates and leaf-out dates from LED 22 m NDVI (b). To calculate MODIS based leaf-out dates, we used MCD43 (500 m, spatial resolution) product.

Reference

- Ahl, D.E. et al., 2006. Monitoring spring canopy phenology of a deciduous broadleaf forest using MODIS. *Remote Sensing of Environment*, 104(1): 88–95.
- Alemohammad, S.H. et al., 2017. Water, Energy, and Carbon with Artificial Neural Networks (WECANN): A statistically-based estimate of global surface turbulent fluxes and gross primary productivity using solar-induced fluorescence. *Biogeosciences (Online)*, 14(18): 4101.
- Augspurger, C.K., 2009. Spring 2007 warmth and frost: phenology, damage and refoliation in a temperate deciduous forest. *Functional Ecology*, 23(6): 1031–1039. doi:10.1111/j.1365-2435.2009.01587.x
- Bórnez, K., Descals, A., Verger, A. and Peñuelas, J., 2020. Land surface phenology from VEGETATION and PROBA-V data. Assessment over deciduous forests. *International Journal of Applied Earth Observation and Geoinformation*, 84: 101974.
- Badeck, F.-W. et al., 2004. Responses of spring phenology to climate change. *New Phytologist*, 162(2): 295–309. doi:10.1111/j.1469-8137.2004.01059.x
- Badgley, G., Anderegg, L.D., Berry, J.A. and Field, C.B., 2019. Terrestrial gross primary production: Using NIRV to scale from site to globe. *Global Change Biology*, 25(11): 3731–3740.
- Badgley, G., Field, C.B. and Berry, J.A., 2017. Canopy near-infrared reflectance and terrestrial photosynthesis. *Science Advances*, 3(3): e1602244.
- Baker, N.R., 2008. Chlorophyll fluorescence: A probe of photosynthesis in vivo. *Annual Reviews of Plant Biology*, 59: 89–113.
- Baldocchi, D.D. et al., 2020. Outgoing Near Infrared Radiation from Vegetation Scales with Canopy Photosynthesis Across a Spectrum of Function, Structure, Physiological Capacity and Weather. *Journal of Geophysical Research: Biogeosciences*, n/a(n/a): e2019JG005534. doi:10.1029/2019jg005534
- Baldocchi, D.D., Wilson, K.B. and Gu, L., 2002. How the environment, canopy structure and canopy physiological functioning influence carbon, water and energy fluxes of a temperate broad-leaved deciduous forest—an assessment with the biophysical model CANOAK. *Tree Physiology*, 22(15–16): 1065–1077.
- Barber, J., Malkin, S. and Telfer, A., 1989. The origin of chlorophyll fluorescence in vivo and its quenching by the photosystem II reaction centre. *Philosophical*

- Transactions of the Royal Society of London. B, Biological Sciences, 323(1216): 227–239.
- Barbier, S., Gosselin, F. and Balandier, P., 2008. Influence of tree species on understory vegetation diversity and mechanisms involved—a critical review for temperate and boreal forests. *Forest ecology and management*, 254(1): 1–15.
- Berry, J. and Kornfeld, A., 2019. Collaborative research on ecophysiological controls on Amazonian precipitation seasonality and variability, united states. doi:<https://doi.org/10.2172/1570388>
- Boechat, A.A., Su, D., Hall, D.R. and Jones, J.D., 1991. Bend loss in large core multimode optical fiber beam delivery systems. *Applied optics*, 30(3): 321–327.
- Bonan, G.B., 2008. Forests and climate change: forcings, feedbacks, and the climate benefits of forests. *science*, 320(5882): 1444–1449.
- Bradley, B.A., Jacob, R.W., Hermance, J.F. and Mustard, J.F., 2007. A curve fitting procedure to derive inter-annual phenologies from time series of noisy satellite NDVI data. *Remote sensing of environment*, 106(2): 137–145.
- Brusa, A. and Bunker, D.E., 2014. Increasing the precision of canopy closure estimates from hemispherical photography: Blue channel analysis and under-exposure. *Agricultural and Forest Meteorology*, 195: 102–107.
- Campbell, P.K.E. et al., 2019. Diurnal and Seasonal Variations in Chlorophyll Fluorescence Associated with Photosynthesis at Leaf and Canopy Scales. *Remote Sensing*, 11(5): 488.
- Cao, R., Chen, J., Shen, M. and Tang, Y., 2015. An improved logistic method for detecting spring vegetation phenology in grasslands from MODIS EVI time-series data. *Agricultural and Forest Meteorology*, 200: 9–20.
- Chang, C.Y. et al., 2020. Systematic assessment of retrieval methods for canopy far-red solar-induced chlorophyll fluorescence (SIF) using high-frequency automated field spectroscopy. *Journal of Geophysical Research: Biogeosciences*, n/a(n/a): e2019JG005533. doi:[10.1029/2019JG005533](https://doi.org/10.1029/2019JG005533)
- Cheng, Y.-B. et al., 2013. Integrating solar induced fluorescence and the photochemical reflectance index for estimating gross primary production in a cornfield. *Remote Sensing*, 5(12): 6857–6879.
- Cogliati, S. et al., 2015. Continuous and long-term measurements of reflectance and sun-induced chlorophyll fluorescence by using novel automated field

- spectroscopy systems. *Remote Sensing of Environment*, 164: 270–281. doi:<https://doi.org/10.1016/j.rse.2015.03.027>
- DAAC, O., 2018. MODIS and VIIRS Land Products Global Subsetting and Visualization Tool. ORNL DAAC, Oak Ridge, Tennessee, USA. Accessed 15/03/19. Subset obtained for MOD13Q1 product at 37.3794 S, 70.2695 ...
- Damm, A. et al., 2010a. Remote sensing of sun-induced fluorescence to improve modeling of diurnal courses of gross primary production (GPP). *Global Change Biology*, 16(1): 171–186.
- DAMM, A. et al., 2010b. Remote sensing of sun-induced fluorescence to improve modeling of diurnal courses of gross primary production (GPP). *Global Change Biology*, 16(1): 171–186. doi:[doi:10.1111/j.1365-2486.2009.01908.x](https://doi.org/10.1111/j.1365-2486.2009.01908.x)
- Damm, A. et al., 2011. Modeling the impact of spectral sensor configurations on the FLD retrieval accuracy of sun-induced chlorophyll fluorescence. *Remote Sensing of Environment*, 115(8): 1882–1892. doi:<https://doi.org/10.1016/j.rse.2011.03.011>
- Damm, A. et al., 2015. Far-red sun-induced chlorophyll fluorescence shows ecosystem-specific relationships to gross primary production: An assessment based on observational and modeling approaches. *Remote Sensing of Environment*, 166: 91–105. doi:<https://doi.org/10.1016/j.rse.2015.06.004>
- Daumard, F. et al., 2010. A Field Platform for Continuous Measurement of Canopy Fluorescence. *IEEE Transactions on Geoscience and Remote Sensing*, 48(9): 3358–3368. doi:[10.1109/TGRS.2010.2046420](https://doi.org/10.1109/TGRS.2010.2046420)
- Dechant, B. et al., 2020. Canopy structure explains the relationship between photosynthesis and sun-induced chlorophyll fluorescence in crops. *Remote Sensing of Environment*, 241: 111733. doi:<https://doi.org/10.1016/j.rse.2020.111733>
- Demmig-Adams, B. and Adams III, W.W., 1996. The role of xanthophyll cycle carotenoids in the protection of photosynthesis. *Trends in Plant Science*, 1(1): 21–26. doi:[https://doi.org/10.1016/S1360-1385\(96\)80019-7](https://doi.org/10.1016/S1360-1385(96)80019-7)
- Demmig-Adams, B. and Adams III, W.W., 2006. Photoprotection in an ecological context: the remarkable complexity of thermal energy dissipation. *New Phytologist*, 172(1): 11–21.
- Du, S. et al., 2019. SIFSpec: Measuring Solar-Induced Chlorophyll Fluorescence

- Observations for Remote Sensing of Photosynthesis. *Sensors*, 19(13): 3009.
- Du, S., Liu, L., Liu, X. and Hu, J., 2017. Response of canopy solar-induced chlorophyll fluorescence to the absorbed photosynthetically active radiation absorbed by chlorophyll. *Remote Sensing*, 9(9): 911.
- Dutta, D., Schimel, D.S., Sun, Y., van der Tol, C. and Frankenberg, C., 2019. Optimal inverse estimation of ecosystem parameters from observations of carbon and energy fluxes. *Biogeosciences*, 16(1): 77–103.
- Ettinger, A. et al., 2020. Winter temperatures predominate in spring phenological responses to warming. *Nature Climate Change*, 10(12): 1137–1142.
- Falge, E. et al., 2001. Gap filling strategies for defensible annual sums of net ecosystem exchange. *Agricultural and Forest Meteorology*, 107(1): 43–69.
- Flexas, J. et al., 2002. Steady-state chlorophyll fluorescence (Fs) measurements as a tool to follow variations of net CO₂ assimilation and stomatal conductance during water-stress in C₃ plants. *Physiologia Plantarum*, 114(2): 231–240.
- Fournier, A. et al., 2012. Effect of canopy structure on sun-induced chlorophyll fluorescence. *ISPRS Journal of Photogrammetry and Remote Sensing*, 68: 112–120.
- Frankenberg, C. and Berry, J., 2018. Solar induced chlorophyll fluorescence: origins, relation to photosynthesis and retrieval.
- Frankenberg, C. et al., 2011. New global observations of the terrestrial carbon cycle from GOSAT: Patterns of plant fluorescence with gross primary productivity. *Geophysical Research Letters*, 38(17).
- Fratini, G., Ibrom, A., Arriga, N., Burba, G. and Papale, D., 2012. Relative humidity effects on water vapour fluxes measured with closed-path eddy-covariance systems with short sampling lines. *Agricultural and Forest Meteorology*, 165: 53–63.
- Fu, Y.H. et al., 2015. Declining global warming effects on the phenology of spring leaf unfolding. *Nature*, 526(7571): 104–107.
- Gamon, J., Kovalchuck, O., Wong, C., Harris, A. and Garrity, S., 2015. Monitoring seasonal and diurnal changes in photosynthetic pigments with automated PRI and NDVI sensors. *Biogeosciences*, 12(13): 4149–4159.
- Gamon, J., Serrano, L. and Surfus, J., 1997. The photochemical reflectance index: an optical indicator of photosynthetic radiation use efficiency across species, functional types, and nutrient levels. *Oecologia*, 112(4): 492–501.
- Gamon, J.A. et al., 2016. A remotely sensed pigment index reveals photosynthetic

- phenology in evergreen conifers. *Proceedings of the National Academy of Sciences*, 113(46): 13087–13092.
- Garrrity, S.R., Vierling, L.A. and Bickford, K., 2010. A simple filtered photodiode instrument for continuous measurement of narrowband NDVI and PRI over vegetated canopies. *Agricultural and Forest Meteorology*, 150(3): 489–496.
- Gloge, D., 1972. Bending loss in multimode fibers with graded and ungraded core index. *Applied optics*, 11(11): 2506–2513.
- Goulas, Y. et al., 2017. Gross Primary Production of a Wheat Canopy Relates Stronger to Far Red Than to Red Solar–Induced Chlorophyll Fluorescence. *Remote Sensing*, 9(1): 97.
- Grossmann, K. et al., 2018. PhotoSpec: A new instrument to measure spatially distributed red and far–red Solar–Induced Chlorophyll Fluorescence. *Remote Sensing of Environment*, 216: 311–327. doi:<https://doi.org/10.1016/j.rse.2018.07.002>
- Gu, L. et al., 2005. Objective threshold determination for nighttime eddy flux filtering. *Agricultural and Forest Meteorology*, 128(3–4): 179–197.
- Gu, L., Han, J., Wood, J.D., Chang, C.Y.Y. and Sun, Y., 2019. Sun-induced Chl fluorescence and its importance for biophysical modeling of photosynthesis based on light reactions. *New Phytologist*: 1.
- Gu, L., Wood, J., Chang, C.Y., Sun, Y. and Riggs, J., 2018. Advancing terrestrial ecosystem science with a novel automated measurement system for sun-induced chlorophyll fluorescence for Integration with eddy covariance flux networks. *Journal of Geophysical Research: Biogeosciences*.
- Guanter, L. et al., 2012. Retrieval and global assessment of terrestrial chlorophyll fluorescence from GOSAT space measurements. *Remote Sensing of Environment*, 121: 236–251.
- Guanter, L. et al., 2013. Using field spectroscopy to assess the potential of statistical approaches for the retrieval of sun–induced chlorophyll fluorescence from ground and space. *Remote Sensing of Environment*, 133: 52–61.
- Guanter, L. et al., 2014. Global and time–resolved monitoring of crop photosynthesis with chlorophyll fluorescence. *Proceedings of the National Academy of Sciences*, 111(14): E1327–E1333. doi:10.1073/pnas.1320008111
- Hampel, F.R., 1974. The influence curve and its role in robust estimation. *Journal of the american statistical association*, 69(346): 383–393.
- Helman, D., 2018. Land surface phenology: What do we really ‘see’ from space?

- Science of the Total Environment, 618: 665–673.
- Horst, T. and Lenschow, D., 2009. Attenuation of scalar fluxes measured with spatially-displaced sensors. *Boundary-layer Meteorology*, 130(2): 275–300.
- Howell, S.B., 1989. Two-dimensional aperture photometry: signal-to-noise ratio of point-source observations and optimal data-extraction techniques. *Publications of the Astronomical Society of the Pacific*, 101(640): 616.
- Hueni, A. and Bialek, A., 2017. Cause, effect, and correction of field spectroradiometer interchannel radiometric steps. *IEEE Journal of Selected Topics in Applied Earth Observations and Remote Sensing*, 10(4): 1542–1551.
- Jahns, P. and Holzwarth, A.R., 2012. The role of the xanthophyll cycle and of lutein in photoprotection of photosystem II. *Biochimica et Biophysica Acta (BBA) – Bioenergetics*, 1817(1): 182–193.
- Jeong, S.-J. et al., 2014. Effects of double cropping on summer climate of the North China Plain and neighbouring regions. *Nature Climate Change*, 4(7): 615–619.
- Jeong, S.-J. et al., 2017. Application of satellite solar-induced chlorophyll fluorescence to understanding large-scale variations in vegetation phenology and function over northern high latitude forests. *Remote Sensing of Environment*, 190: 178–187. doi:<https://doi.org/10.1016/j.rse.2016.11.021>
- Jiang, C., Guan, K., Wu, G., Peng, B. and Wang, S., 2020. A daily, 250 m, and real-time gross primary productivity product (2000–present) covering the Contiguous United States. *Earth Syst. Sci. Data Discuss.*, 2020: 1–28. doi:10.5194/essd-2020-36
- Jiang, C. and Ryu, Y., 2016. Multi-scale evaluation of global gross primary productivity and evapotranspiration products derived from Breathing Earth System Simulator (BESS). *Remote Sensing of Environment*, 186: 528–547.
- Joiner, J. et al., 2013. Global monitoring of terrestrial chlorophyll fluorescence from moderate-spectral-resolution near-infrared satellite measurements: methodology, simulations, and application to GOME-2. *Atmospheric Measurement Techniques*, 6(10): 2803–2823.
- Joiner, J. et al., 2014. The seasonal cycle of satellite chlorophyll fluorescence observations and its relationship to vegetation phenology and ecosystem

- atmosphere carbon exchange. *Remote Sensing of Environment*, 152: 375–391. doi:<https://doi.org/10.1016/j.rse.2014.06.022>
- Jonsson, P. and Eklundh, L., 2002. Seasonality extraction by function fitting to time-series of satellite sensor data. *IEEE transactions on Geoscience and Remote Sensing*, 40(8): 1824–1832.
- Julitta, T. et al., 2016. Comparison of Sun-Induced Chlorophyll Fluorescence Estimates Obtained from Four Portable Field Spectroradiometers. *Remote Sensing*, 8(2): 122.
- Köhler, P. et al., 2018. Global retrievals of solar-induced chlorophyll fluorescence with TROPOMI: First results and intersensor comparison to OCO-2. *Geophysical Research Letters*, 45(19): 10,456–10,463.
- Körner, C. and Basler, D., 2010. Phenology under global warming. *Science*, 327(5972): 1461–1462.
- Kang, M. et al., 2018. Changes and improvements of the standardized eddy covariance data processing in KoFlux. *Korean Journal of Agricultural and Forest Meteorology*, 20(1): 5–17.
- Kattge, J., Knorr, W., Raddatz, T. and Wirth, C., 2009. Quantifying photosynthetic capacity and its relationship to leaf nitrogen content for global-scale terrestrial biosphere models. *Global Change Biology*, 15(4): 976–991.
- Kebabian, P.L., Theisen, A.F., Kallelis, S. and Freedman, A., 1999. A passive two-band sensor of sunlight-excited plant fluorescence. *Review of Scientific Instruments*, 70(11): 4386–4393.
- Keenan, T.F. et al., 2014. Net carbon uptake has increased through warming-induced changes in temperate forest phenology. *Nature Climate Change*, 4(7): 598–604. doi:10.1038/nclimate2253
- Kim, J. et al., 2021. Regional and Species Variations in Spring and Autumn Phenology of 25 Temperate Species in South Korea. *Asia-Pacific Journal of Atmospheric Sciences*: 1–15.
- Kim, J., Ryu, Y., Jiang, C. and Hwang, Y., 2019. Continuous observation of vegetation canopy dynamics using an integrated low-cost, near-surface remote sensing system. *Agricultural and Forest Meteorology*, 264: 164–177. doi:<https://doi.org/10.1016/j.agrformet.2018.09.014>
- Kim, T.K., 2014. Effects of Leaf Area Change on Transpiration and Productivity of 50-year-old *Pinus koraiensis* stands in Mt. Taehwa, Seoul National University. doi:<http://hdl.handle.net/10371/121071>

- Kobayashi, H. et al., 2018. In situ observations reveal how spectral reflectance responds to growing season phenology of an open evergreen forest in Alaska. *Remote Sensing*, 10(7): 1071.
- Lee, B. et al., 2020. An artificial intelligence approach to predict gross primary productivity in the forests of South Korea using satellite remote sensing data. *Forests*, 11(9): 1000.
- Lee, H., Park, J., Cho, S., Lee, M. and Kim, H.S., 2019. Impact of leaf area index from various sources on estimating gross primary production in temperate forests using the JULES land surface model. *Agricultural and Forest Meteorology*, 276: 107614.
- Lee, S., Ryu, Y. and Jiang, C., 2015. Urban heat mitigation by roof surface materials during the East Asian summer monsoon. *Environmental Research Letters*, 10(12): 124012.
- Li, W. and Fang, H., 2015. Estimation of direct, diffuse, and total FPARs from Landsat surface reflectance data and ground-based estimates over six FLUXNET sites. *Journal of Geophysical Research: Biogeosciences*, 120(1): 96–112.
- Li, Z. et al., 2020. Solar-induced chlorophyll fluorescence and its link to canopy photosynthesis in maize from continuous ground measurements. *Remote Sensing of Environment*, 236: 111420. doi:<https://doi.org/10.1016/j.rse.2019.111420>
- Liang, J. et al., 2016. Positive biodiversity–productivity relationship predominant in global forests. *Science*, 354(6309): aaf8957.
- Liu, H., Ye, Q. and Wiens, J.J., 2020a. Climatic–niche evolution follows similar rules in plants and animals. *Nature ecology & evolution*, 4(5): 753–763.
- Liu, L. et al., 2020b. Estimating maize GPP using near-infrared radiance of vegetation. *Science of Remote Sensing*, 2: 100009.
- Liu, N. et al., 2021. Trail camera networks provide insights into satellite-derived phenology for ecological studies. *International Journal of Applied Earth Observation and Geoinformation*, 97: 102291.
- Liu, W. et al., 2019. Simulating solar-induced chlorophyll fluorescence in a boreal forest stand reconstructed from terrestrial laser scanning measurements. *Remote Sensing of Environment*, 232: 111274. doi:<https://doi.org/10.1016/j.rse.2019.111274>
- Liu, X. and Liu, L., 2018. Influence of the canopy BRDF characteristics and illumination conditions on the retrieval of solar-induced chlorophyll

- fluorescence. *International Journal of Remote Sensing*, 39(6): 1782–1799.
- Liu, Z., Jin, G. and Qi, Y., 2012. Estimate of leaf area index in an old-growth mixed broadleaved–Korean Pine Forest in Northeastern China. *PloS One*, 7(3): e32155.
- Louis, J. et al., 2005. Remote sensing of sunlight-induced chlorophyll fluorescence and reflectance of Scots pine in the boreal forest during spring recovery. *Remote Sensing of Environment*, 96(1): 37–48. doi:<https://doi.org/10.1016/j.rse.2005.01.013>
- Lu, X., Liu, Z., Zhao, F. and Tang, J., 2020. Comparison of total emitted solar-induced chlorophyll fluorescence (SIF) and top-of-canopy (TOC) SIF in estimating photosynthesis. *Remote Sensing of Environment*, 251: 112083.
- Lu, X. et al., 2018. Comparison of phenology estimated from reflectance-based indices and solar-induced chlorophyll fluorescence (SIF) observations in a temperate forest using GPP-based phenology as the standard. *Remote Sensing*, 10(6): 932.
- Míguez, F., Fernández-Marín, B., Becerril, J.M. and García-Plazaola, J.I., 2015. Activation of photoprotective winter photoinhibition in plants from different environments: a literature compilation and meta-analysis. *Physiologia Plantarum*, 155(4): 414–423.
- Müller, P., Li, X.-P. and Niyogi, K.K., 2001. Non-photochemical quenching. A response to excess light energy. *Plant Physiology*, 125(4): 1558–1566.
- Magney, T.S., Barnes, M.L. and Yang, X., 2020. On the covariation of chlorophyll fluorescence and photosynthesis across scales. *Geophysical Research Letters*: e2020GL091098.
- Magney, T.S. et al., 2019. Mechanistic evidence for tracking the seasonality of photosynthesis with solar-induced fluorescence. *Proceedings of the National Academy of Sciences*, 116(24): 11640–11645. doi:10.1073/pnas.1900278116
- Magney, T.S., Eitel, J.U., Huggins, D.R. and Vierling, L.A., 2016. Proximal NDVI derived phenology improves in-season predictions of wheat quantity and quality. *Agricultural and Forest Meteorology*, 217: 46–60.
- Maguire, A.J. et al., 2020. On the Functional Relationship Between Fluorescence and Photochemical Yields in Complex Evergreen Needleleaf Canopies. *Geophysical Research Letters*: e2020GL087858.
- Majasalmi, T., Rautiainen, M., Stenberg, P. and Manninen, T., 2015. Validation of

- MODIS and GEOV1 fPAR products in a boreal forest site in Finland. *Remote Sensing*, 7(2): 1359–1379.
- Majasalmi, T., Stenberg, P. and Rautiainen, M., 2017. Comparison of ground and satellite-based methods for estimating stand-level fPAR in a boreal forest. *Agricultural and Forest Meteorology*, 232: 422–432.
- Marcolla, B. and Cescatti, A., 2017. Geometry of the hemispherical radiometric footprint over plant canopies. *Theoretical and Applied Climatology*. doi:10.1007/s00704-017-2326-z
- Maxwell, K. and Johnson, G.N., 2000. Chlorophyll fluorescence—a practical guide. *Journal of Experimental Botany*, 51(345): 659–668.
- Menzel, A., 2002. Phenology: its importance to the global change community. *Climatic change*, 54(4): 379–385.
- Menzel, A. et al., 2006. European phenological response to climate change matches the warming pattern. *Global change biology*, 12(10): 1969–1976.
- Meroni, M. and Colombo, R., 2006. Leaf level detection of solar induced chlorophyll fluorescence by means of a subnanometer resolution spectroradiometer. *Remote Sensing of Environment*, 103(4): 438–448. doi:<https://doi.org/10.1016/j.rse.2006.03.016>
- Meroni, M. et al., 2009. Remote sensing of solar-induced chlorophyll fluorescence: Review of methods and applications. *Remote Sensing of Environment*, 113(10): 2037–2051. doi:10.1016/j.rse.2009.05.003
- Miao, G. et al., 2018. Sun-induced chlorophyll fluorescence, photosynthesis, and light use efficiency of a soybean field from seasonally continuous measurements. *Journal of Geophysical Research: Biogeosciences*, 123(2): 610–623. doi:doi:10.1002/2017JG004180
- Mohammed, G.H. et al., 2019. Remote sensing of solar-induced chlorophyll fluorescence (SIF) in vegetation: 50 years of progress. *Remote Sensing of Environment*, 231: 111177. doi:<https://doi.org/10.1016/j.rse.2019.04.030>
- Monteith, J., 1972. Solar radiation and productivity in tropical ecosystems. *Journal of Applied Ecology*, 9(3): 747–766.
- Moon, M. et al., 2019. Long-term continuity in land surface phenology measurements: a comparative assessment of the MODIS land cover dynamics and VIIRS land surface phenology products. *Remote Sensing of Environment*, 226: 74–92.
- Moore, C.E., Beringer, J., Evans, B., Hutley, L.B. and Tapper, N.J., 2017. Tree-grass

- phenology information improves light use efficiency modelling of gross primary productivity for an Australian tropical savanna. *Biogeosciences*, 14(1): 111–129.
- Motulsky, H. and Christopoulos, A., 2004. Fitting models to biological data using linear and nonlinear regression: a practical guide to curve fitting. Oxford University Press.
- Moya, I. et al., 2004. A new instrument for passive remote sensing: 1. Measurements of sunlight-induced chlorophyll fluorescence. *Remote Sensing of Environment*, 91(2): 186–197. doi:<https://doi.org/10.1016/j.rse.2004.02.012>
- Muller, R.N., 1978. The phenology, growth and ecosystem dynamics of *Erythronium americanum* in the northern hardwood forest. *Ecological Monographs*, 48(1): 1–20.
- Nagai, S. et al., 2012. In situ examination of the relationship between various vegetation indices and canopy phenology in an evergreen coniferous forest, Japan. *International Journal of Remote Sensing*, 33(19): 6202–6214.
- Nichol, C.J. et al., 2019. Diurnal and Seasonal Solar Induced Chlorophyll Fluorescence and Photosynthesis in a Boreal Scots Pine Canopy. *Remote Sensing*, 11(3): 273.
- Ollinger, S.V., 2011. Sources of variability in canopy reflectance and the convergent properties of plants. *New Phytologist*, 189(2): 375–394.
- Pacheco-Labrador, J. et al., 2019. Sun-induced chlorophyll fluorescence I: Instrumental considerations for proximal spectroradiometers. *Remote Sensing*, 11(8): 960.
- Pacheco-Labrador, J. and Martín, M., 2015. Characterization of a field spectroradiometer for unattended vegetation monitoring. Key sensor models and impacts on reflectance. *Sensors*, 15(2): 4154–4175.
- Pan, Y. et al., 2011. A large and persistent carbon sink in the world's forests. *Science*, 333(6045): 988–993.
- Parazoo, N.C. et al., 2020. Wide discrepancies in the magnitude and direction of modeled solar-induced chlorophyll fluorescence in response to light conditions. *Biogeosciences*, 17(13): 3733–3755. doi:10.5194/bg-17-3733-2020
- Park, J. et al., 2018. Effects of thinning intensities on tree water use, growth, and resultant water use efficiency of 50-year-old *Pinus koraiensis* forest over

- four years. *Forest Ecology and Management*, 408: 121–128.
- Paul–Limoges, E. et al., 2018. Effect of environmental conditions on sun–induced fluorescence in a mixed forest and a cropland. *Remote Sensing of Environment*, 219: 310–323. doi:<https://doi.org/10.1016/j.rse.2018.10.018>
- Peñuelas, J. and Filella, I., 2009. Phenology feedbacks on climate change. *Science*, 324(5929): 887–888.
- Piao, S. et al., 2019. Plant phenology and global climate change: Current progresses and challenges. *Global change biology*, 25(6): 1922–1940.
- Plascyk, J.A., 1975. The MK II Fraunhofer Line Discriminator (FLD–II) for Airborne and Orbital Remote Sensing of Solar–Stimulated Luminescence, 14. SPIE.
- Pontailleur, J.–Y., Hymus, G.J. and Drake, B.G., 2003. Estimation of leaf area index using ground–based remote sensed NDVI measurements: validation and comparison with two indirect techniques. *Canadian Journal of Remote Sensing*, 29(3): 381–387. doi:10.5589/m03–009
- Pontailleur, J.Y. and Genty, B., 1996. A Simple Red: Far–Red Sensor Using Gallium Arsenide Phosphide Detectors. *Functional Ecology*, 10(4): 535–540. doi:10.2307/2389947
- Porcar–Castell, A. et al., 2014. Linking chlorophyll a fluorescence to photosynthesis for remote sensing applications: mechanisms and challenges. *Journal of Experimental Botany*, 65(15): 4065–4095.
- Porcar–Castell, A., 2011. A high-resolution portrait of the annual dynamics of photochemical and non-photochemical quenching in needles of *Pinus sylvestris*. *Physiologia Plantarum*, 143(2): 139–153.
- Prentice, I.C. et al., 1992. Special paper: a global biome model based on plant physiology and dominance, soil properties and climate. *Journal of biogeography*: 117–134.
- Raczka, B. et al., 2019. Sustained non–photochemical quenching shapes the seasonal pattern of solar– induced fluorescence at a high–elevation evergreen forest. *Journal of Geophysical Research: Biogeosciences*, 0(ja). doi:10.1029/2018jg004883
- Reichstein, M. et al., 2005. On the separation of net ecosystem exchange into assimilation and ecosystem respiration: Review and improved algorithm. *Global Change Biology*, 11(9): 1424–1439.
- Renhorn, I.G., Bergström, D., Hedborg, J., Letalick, D. and Möller, S., 2016. High spatial resolution hyperspectral camera based on a linear variable filter.

- Optical Engineering, 55(11): 114105.
- Richardson, A.D., et al, 2009. Near-surface remote sensing of spatial and temporal variation in canopy phenology. . Ecological Applications(19.6): 1417–1428.
- Richardson, A.D. et al., 2013a. Climate change, phenology, and phenological control of vegetation feedbacks to the climate system. Agricultural and Forest Meteorology, 169: 156–173. doi:10.1016/j.agrformet.2012.09.012
- Richardson, A.D., Klosterman, S. and Toomey, M., 2013b. Near-surface sensor-derived phenology, Phenology: An integrative environmental science. Springer, pp. 413–430.
- Richardson, A.D. and O' Keefe, J., 2009. Phenological Differences Between Understory and Overstory. 87–117. doi:10.1007/978-1-4419-0026-5_4
- Rienstra, J.L., 1998. Transformation of filter transmission data for f-number and chief ray angle, Infrared Imaging Systems: Design, Analysis, Modeling, and Testing IX. International Society for Optics and Photonics, pp. 267–275.
- Riitters, K., Wickham, J., O' Neill, R., Jones, B. and Smith, E., 2000. Global-scale patterns of forest fragmentation. Conservation ecology, 4(2).
- Rossini, M. et al., 2010. High resolution field spectroscopy measurements for estimating gross ecosystem production in a rice field. Agricultural and Forest Meteorology, 150(9): 1283–1296. doi:<https://doi.org/10.1016/j.agrformet.2010.05.011>
- Rossini, M. et al., 2015. Red and far red Sun-induced chlorophyll fluorescence as a measure of plant photosynthesis. Geophysical research letters, 42(6): 1632–1639.
- Rousseeuw, P.J. and Croux, C., 1993. Alternatives to the median absolute deviation. Journal of the American Statistical Association, 88(424): 1273–1283.
- Ruban, A., Rees, D., Pascal, A. and Horton, P., 1992. Mechanism of Δ pH-dependent dissipation of absorbed excitation energy by photosynthetic membranes. II. The relationship between LHCII aggregation in vitro and qE in isolated thylakoids. Biochimica et Biophysica Acta (BBA)–Bioenergetics, 1102(1): 39–44.
- Ryu, Y. et al., 2010. Testing the performance of a novel spectral reflectance sensor, built with light emitting diodes (LEDs), to monitor ecosystem metabolism, structure and function. Agricultural and Forest Meteorology, 150(12): 1597–1606. doi:10.1016/j.agrformet.2010.08.009
- Ryu, Y., Berry, J.A. and Baldocchi, D.D., 2019. What is global photosynthesis?

- History, uncertainties and opportunities. *Remote Sensing of Environment*, 223: 95–114.
- Ryu, Y., Lee, G., Jeon, S., Song, Y. and Kimm, H., 2014. Monitoring multi-layer canopy spring phenology of temperate deciduous and evergreen forests using low-cost spectral sensors. *Remote Sensing of Environment*, 149: 227–238. doi:10.1016/j.rse.2014.04.015
- Schaaf, C. and Wang, Z., 2015. MCD43A4 MODIS/Terra+ Aqua BRDF/Albedo Nadir BRDF Adjusted RefDaily L3 Global 500 m V006. NASA EOSDIS Land Processes DAAC.
- Schaepman-Strub, G., Schaepman, M., Painter, T.H., Dangel, S. and Martonchik, J.V., 2006. Reflectance quantities in optical remote sensing—Definitions and case studies. *Remote Sensing of Environment*, 103(1): 27–42.
- Seiwa, K., 1999. Changes in leaf phenology are dependent on tree height in *Acer mono*, a deciduous broad-leaved tree. *Annals of botany*, 83(4): 355–361.
- Serbin, S.P., Ahl, D.E. and Gower, S.T., 2013. Spatial and temporal validation of the MODIS LAI and FPAR products across a boreal forest wildfire chronosequence. *Remote Sensing of Environment*, 133: 71–84. doi:<https://doi.org/10.1016/j.rse.2013.01.022>
- Song, Y. and Ryu, Y., 2015. Seasonal changes in vertical canopy structure in a temperate broadleaved forest in Korea. *Ecological Research*. doi:10.1007/s11284-015-1281-3
- Soudani, K. et al., 2012. Ground-based Network of NDVI measurements for tracking temporal dynamics of canopy structure and vegetation phenology in different biomes. *Remote Sensing of Environment*, 123: 234–245. doi:<https://doi.org/10.1016/j.rse.2012.03.012>
- Springer, K., Wang, R. and Gamon, J., 2017. Parallel seasonal patterns of photosynthesis, fluorescence, and reflectance indices in boreal trees. *Remote Sensing*, 9(7): 691.
- Sun, Y. et al., 2018. Overview of Solar-Induced chlorophyll Fluorescence (SIF) from the Orbiting Carbon Observatory-2: Retrieval, cross-mission comparison, and global monitoring for GPP. *Remote sensing of environment*, 209: 808–823.
- Sun, Y. et al., 2017. OCO-2 advances photosynthesis observation from space via solar-induced chlorophyll fluorescence. *Science*, 358(6360): eaam5747.
- Thurner, M. et al., 2014. Carbon stock and density of northern boreal and temperate

- forests. *Global Ecology and Biogeography*, 23(3): 297–310.
- Tomita, M. and Seiwa, K., 2004. Influence of canopy tree phenology on understorey populations of *Fagus crenata*. *Journal of Vegetation Science*, 15(3): 379. doi:10.1658/1100–9233(2004)015[0379:ioctpo]2.0.co;2
- Tucker, C.J., 1979. Red and photographic infrared linear combinations for monitoring vegetation. *Remote Sensing of Environment*, 8(2): 127–150.
- van der Tol, C., Verhoef, W., Timmermans, J., Verhoef, A. and Su, Z., 2009. An integrated model of soil–canopy spectral radiances, photosynthesis, fluorescence, temperature and energy balance. *Biogeosciences*, 6(12).
- van Gorsel, E. et al., 2009. Estimating nocturnal ecosystem respiration from the vertical turbulent flux and change in storage of CO₂. *Agricultural and forest meteorology*, 149(11): 1919–1930.
- van Gorsel, E. et al., 2008. Application of an alternative method to derive reliable estimates of nighttime respiration from eddy covariance measurements in moderately complex topography. *Agricultural and Forest Meteorology*, 148(6–7): 1174–1180.
- van Gorsel, E., Leuning, R., Cleugh, H.A., Keith, H. and Suni, T., 2007. Nocturnal carbon efflux: reconciliation of eddy covariance and chamber measurements using an alternative to the u_{*}–threshold filtering technique. *Tellus B: Chemical and Physical Meteorology*, 59(3): 397–403.
- Van Rensen, J., 1989. Herbicides interacting with photosystem II. *Herbicides and plant metabolism*: 21–36.
- Verhoeven, A., 2014. Sustained energy dissipation in winter evergreens. *New Phytologist*, 201(1): 57–65.
- Vermote, E., Justice, C., Claverie, M. and Franch, B., 2016. Preliminary analysis of the performance of the Landsat 8/OLI land surface reflectance product. *Remote Sensing of Environment*, 185: 46–56.
- Vermote, E. and Wolfe, R., 2015. MOD09GA MODIS/Terra surface reflectance daily L2G global 1km and 500m SIN grid V006 [data set]. NASA EOSDIS Land Processes DAAC. Accessed 2019–08–14 from <https://doi.org/10.5067/MODIS/MOD09GA.006>.
- Vilfan, N., Van der Tol, C., Muller, O., Rascher, U. and Verhoef, W., 2016. Fluspect–B: A model for leaf fluorescence, reflectance and transmittance spectra. *Remote Sensing of Environment*, 186: 596–615.
- Walther, S. et al., 2016. Satellite chlorophyll fluorescence measurements reveal

- large-scale decoupling of photosynthesis and greenness dynamics in boreal evergreen forests. *Global Change Biology*, 22(9): 2979–2996.
- Wang, H., Song, H., Chen, Y. and Laney, S.R., 2015. Correcting temperature dependence in miniature spectrometers used in cold polar environments. *Applied optics*, 54(11): 3162–3172.
- Wang, X. et al., 2019. No trends in spring and autumn phenology during the global warming hiatus. *Nature communications*, 10(1): 1–10.
- Webb, E.K., Pearman, G.I. and Leuning, R., 1980. Correction of flux measurements for density effects due to heat and water vapour transfer. *Quarterly Journal of the Royal Meteorological Society*, 106(447): 85–100.
- Wellburn, R., 1994. The spectral determination of chlorophylls a and b, as well as total carotenoids, using various solvents with spectrophotometers of different resolution. *Journal of plant physiology*, 144(3): 307–313.
- White, K., Pontius, J. and Schaberg, P., 2014. Remote sensing of spring phenology in northeastern forests: a comparison of methods, field metrics and sources of uncertainty. *Remote Sensing of Environment*, 148: 97–107.
- White, M.A. et al., 2009. Intercomparison, interpretation, and assessment of spring phenology in North America estimated from remote sensing for 1982–2006. *Global Change Biology*, 15(10): 2335–2359. doi:10.1111/j.1365–2486.2009.01910.x
- White, M.A., Thornton, P.E. and Running, S.W., 1997. A continental phenology model for monitoring vegetation responses to interannual climatic variability. *Global biogeochemical cycles*, 11(2): 217–234.
- Wieneke, S. et al., 2018. Linking photosynthesis and sun-induced fluorescence at sub-daily to seasonal scales. *Remote Sensing of Environment*, 219: 247–258. doi:<https://doi.org/10.1016/j.rse.2018.10.019>
- Wilczak, J.M., Oncley, S.P. and Stage, S.A., 2001. Sonic anemometer tilt correction algorithms. *Boundary-layer Meteorology*, 99(1): 127–150.
- Wohlfahrt, G. et al., 2018. Sun-induced fluorescence and gross primary productivity during a heat wave. *Scientific Reports*, 8(1): 14169. doi:10.1038/s41598–018–32602–z
- Wong, C. and Gamon, J.A., 2015. Three causes of variation in the photochemical reflectance index (PRI) in evergreen conifers. *New Phytologist*, 206(1): 187–195.
- Wong, C.Y., D'Odorico, P., Bhathena, Y., Arain, M.A. and Ensminger, I., 2019.

- Carotenoid based vegetation indices for accurate monitoring of the phenology of photosynthesis at the leaf-scale in deciduous and evergreen trees. *Remote Sensing of Environment*, 233: 111407.
- Wong, C.Y., D' Odorico, P., Arain, M.A. and Ensminger, I., 2020. Tracking the phenology of photosynthesis using carotenoid sensitive and near-infrared reflectance vegetation indices in a temperate evergreen and mixed deciduous forest. *New Phytologist*.
- Wu, G. et al., 2020. Radiance-based NIRv as a proxy for GPP of corn and soybean. *Environmental Research Letters*, 15(3): 034009.
- Xie, Y. and Wilson, A.M., 2020. Change point estimation of deciduous forest land surface phenology. *Remote Sensing of Environment*, 240: 111698.
- Yang, H. et al., 2017. Chlorophyll fluorescence tracks seasonal variations of photosynthesis from leaf to canopy in a temperate forest. *Global Change Biology*, 23(7): 2874–2886. doi:doi:10.1111/gcb.13590
- Yang, J. et al., 2018a. Amazon drought and forest response: Largely reduced forest photosynthesis but slightly increased canopy greenness during the extreme drought of 2015/2016. *Global Change Biology*, 24(5): 1919–1934. doi:doi:10.1111/gcb.14056
- Yang, K. et al., 2018b. Sun-induced chlorophyll fluorescence is more strongly related to absorbed light than to photosynthesis at half-hourly resolution in a rice paddy. *Remote Sensing of Environment*, 216: 658–673. doi:<https://doi.org/10.1016/j.rse.2018.07.008>
- Yang, P. and van der Tol, C., 2018. Linking canopy scattering of far-red sun-induced chlorophyll fluorescence with reflectance. *Remote Sensing of Environment*, 209: 456–467.
- Yang, X. et al., 2018c. FluoSpec 2—an automated field spectroscopy system to monitor canopy solar-Induced fluorescence. *Sensors*, 18(7): 2063.
- Yang, X. et al., 2015. Solar-induced chlorophyll fluorescence that correlates with canopy photosynthesis on diurnal and seasonal scales in a temperate deciduous forest. *Geophysical Research Letters*, 42(8): 2977–2987.
- Yu, H., Luedeling, E. and Xu, J., 2010. Winter and spring warming result in delayed spring phenology on the Tibetan Plateau. *Proceedings of the National Academy of Sciences*, 107(51): 22151–22156.
- Zarco-Tejada, P.J. et al., 2018. Previsual symptoms of *Xylella fastidiosa* infection revealed in spectral plant-trait alterations. *Nature Plants*, 4(7): 432–439.

- Zeng, Y. et al., 2019. A practical approach for estimating the escape ratio of near-infrared solar-induced chlorophyll fluorescence. *Remote Sensing of Environment*: 111209. doi:<https://doi.org/10.1016/j.rse.2019.05.028>
- Zhang, C. et al., 2019. Do all chlorophyll fluorescence emission wavelengths capture the spring recovery of photosynthesis in boreal evergreen foliage? *Plant, cell & environment*.
- Zhang, X. et al., 2003. Monitoring vegetation phenology using MODIS. *Remote sensing of environment*, 84(3): 471–475.
- Zhang, Y. et al., 2014. Estimation of vegetation photosynthetic capacity from space-based measurements of chlorophyll fluorescence for terrestrial biosphere models. *Global Change Biology*, 20(12): 3727–3742.
- Zhang, Y. et al., 2016a. Model-based analysis of the relationship between sun-induced chlorophyll fluorescence and gross primary production for remote sensing applications. *Remote Sensing of Environment*, 187: 145–155. doi:<https://doi.org/10.1016/j.rse.2016.10.016>
- Zhang, Y., Guanter, L., Joiner, J., Song, L. and Guan, K., 2018a. Spatially-explicit monitoring of crop photosynthetic capacity through the use of space-based chlorophyll fluorescence data. *Remote Sensing of Environment*, 210: 362–374. doi:<https://doi.org/10.1016/j.rse.2018.03.031>
- Zhang, Y. et al., 2016b. Consistency between sun-induced chlorophyll fluorescence and gross primary production of vegetation in North America. *Remote Sensing of Environment*, 183: 154–169.
- Zhang, Y. et al., 2018b. On the relationship between sub-daily instantaneous and daily total gross primary production: Implications for interpreting satellite-based SIF retrievals. *Remote Sensing of Environment*, 205: 276–289. doi:<https://doi.org/10.1016/j.rse.2017.12.009>
- Zhao, F. et al., 2014. A method to reconstruct the solar-induced canopy fluorescence spectrum from hyperspectral measurements. *Remote Sensing*, 6(10): 10171–10192.
- Zhou, X., Liu, Z., Xu, S., Zhang, W. and Wu, J., 2016. An Automated Comparative Observation System for Sun-Induced Chlorophyll Fluorescence of Vegetation Canopies. *Sensors*, 16(6): 775.
- Zhou, Y.-M. et al., 2011. Species-specific and needle age-related responses of photosynthesis in two *Pinus* species to long-term exposure to elevated CO

2 concentration. *Trees*, 25(2): 163–173.

Zuromski, L.M. et al., 2018. Solar-Induced Fluorescence Detects Interannual Variation in Gross Primary Production of Coniferous Forests in the Western United States. *Geophysical Research Letters*.

Chapter 5. Conclusion

Satellite remote sensing is a useful tools with many possibilities because it can easily monitor vegetation changes from canopy to global scale. However, to understand more accurate satellite observation values, evaluations based on observed in-situ data from the ground are required. In this dissertation, I conducted 1) developing low-cost filter-based near-surface remote sensing system to monitor vegetation phenology and SIF continuously, 2) monitoring SIF in a temperate evergreen needleleaf forest continuously, and 3) understanding the relationships between phenology from multi-layer canopies and satellite products. The developed near surface remote sensing system was low-cost, easy to use and showed reasonable performance compared to commercial spectroscopy system. As a result of continuously observed SIF and GPP in temperate evergreen needleleaf forest using near surface remote sensing system, it was confirmed that SIF and GPP showed a non-linear relationship. This result is contradictory to the linear relationship between satellite based SIF and GPP from numerous previous studies. From Chapter 4, I found that satellite-based leaf-out and full leaf dates represent understory and overstory signals in a deciduous forest site, which requires caution when using satellite based phenology data into future prediction as overstory and understory canopy show different sensitivities to air temperature. Therefore, observed data in the field by using near-surface remote sensing system could show different results compared to studies using satellite imagery and the in-situ observed data could be used to evaluate and understand outputs from satellite products.

Abstract in Korean

근접 표면 원격 센싱 시스템들을 이용한 지속적 식생 계절 및 태양 유도 엽록소 형광물질 관측

김종민

서울대학교 환경대학원 협동과정조경학

논문지도교수: 류영렬

식물 계절 및 식생의 생리학적, 구조적인 변화를 지속적으로 모니터링 하는 것은 육상생태계와 대기권 사이의 에너지, 탄소 순환 등의 피드백을 이해하는데 필수적이다. 이를 관측하기 위하여 위성에서 관측된 정규화 식생 지수 (NDVI) 태양 유도 엽록소 형광물질 (SIF)는 대중적으로 사용되고 있다. 그러나, 우주 위성 기반의 자료는 다음과 같은 한계점들이 존재한다. 1) 아직까지 고해상도의 위성 기반 SIF 자료는 없고, 2) 위성 자료들은 대기의 질 (예, 구름)에 영향을 받아, 흐린 날의 식생의 생리학적, 구조적 변화를 탐지하기 힘들다. 또한, 3) 위성 이미지는 상부 식생과 하부 식생이 혼합되어 섞인 신호를 탐지하기 때문에, 각 층의 식물 계절을 각각 연구하기에 어려움이 있다. 그러므로, 위성에서 탐지한 신호를 평가하고, 식생의 생리학적, 구조적 변화를 보다 정확히 이해하기 위해서는 근접 표면 원격 센싱 시스템을 이용한 실측 자료 기반의 연구들이 요구된다. 본 학위논문의 주 목적은 근접 표면 원격 센싱 시스템을 이용하여 식물 계절 및 SIF를 현장에서 지속적으로 실측하고, 위성 영상 기반의 연구가 갖고 있는 한계점 및 궁금증들을 해결 및 보완하는 것이다. 이 목적을 달성하기 위하여, 아래와 같은 세가지 Chapter: 1) SIF를 관측하기 위한 필터 기반의 저렴한 근접 표면 센싱 시스템 개발, 2)온대 침엽수림에서의 연속적인 SIF 관측, 3)위성 기반의 식물 계절과 실측한 다층 식생의 식물 계절 비교로 구성하고, 이를 진행하였다.

SIF는 식생의 구조적, 생리학적 변화를 이해하고, 추정하는 인자로 사용될 수 있어, SIF를 현장에서 관측하기 위한 다양한 근접 표면 원격 센싱 시스템들이 최근 제시되어 오고 있다. 그러나, 아직까지 SIF를 관측하기 위한 상업적으로 유통되는 관측 시스템은 현저히 부족하며, 분광계의 구조적 특성상 현장에서 관측 시스템을 보정 및 관리하기가 어려워 높은 질의 SIF를 취득하는 것은 매우 도전적인 분야이다. 본 학위 논문의 **Chapter 2**에서는 SIF를 현장에서 보다 손쉽게 관측하기 위한 필터 기반의 근접 표면 센싱 시스템(Smart Surface Sensing System, 4S-SIF)을 개발하였다. 센서는 대역 필터들과 포토다이오드가 결합되어 있으며, 서보 모터를 사용하여 대역 필터 및 관측 방향을 자동적으로 변경함으로써, 한 개의 포토다이오드가 3개의 파장 범위(757, 760, 770 nm)의 빛 및 태양으로부터 입사되는 광량과 식생으로 반사/방출된 광량을 관측할 수 있도록 고안되었다. 포토다이오드로부터 인식된 디지털 수치 값은 상업적으로 판매되는 초고해상도 분광계(QE Pro, Ocean Insight)와 뚜렷한 선형 관계를 보이는 것을 확인하였다 ($R^2 > 0.99$). 추가적으로, 4S-SIF에서 관측된 SIF와 초고해상도 분광계를 이용하여 추출한 SIF가 선형적인 관계를 이루는 것을 확인하였다. 식생의 생리학적 변화를 일으키는 화학 물질인 DCMU (3-(3, 4-dichlorophenyl)-1, 1-dimethylurea)을 처리했음에도 불구하고, 산출된 SIF들은 선형 관계를 보였다. 본 센서는 기존 시스템들에 비해 사용하기 쉽고 간단하며, 저렴하기 때문에 다양한 시공간적 스케일의 SIF를 관측할 수 있다는 장점이 있다.

위성 기반의 SIF를 이용하여 총일차생산성(gross primary productivity, GPP)을 추정하는 연구는 최근 탄소 순환 연구 분야에서 각광받고 있는 연구 주제이다. 그러나, SIF와 GPP의 관계는 여전히 많은 불확실성을 지니고 있는데, 이는 SIF-GPP 관계를 조절하는 식생의 구조적 및 생리학적 요인을 따로 분리하여 고찰한 연구들이 부족하기 때문이다. 본 학위 논문의 **Chapter 3**에서는 지속적으로 SIF, GPP, 흡수된 광합성유효복사량 (absorbed photosynthetically active radiation,

APAR), 그리고 클로로필과 카로티노이드의 비율 인자 (chlorophyll: carotenoid index, CCI)를 온대침엽수림에서 연속적으로 관측하였다. SIF-GPP 관계의 구체적인 메커니즘 관계를 밝히기 위하여, 광 이용 효율 (light use efficiency, LUE_p), 엽록소 형광 수득률 (chlorophyll fluorescence yield, Φ_F) 그리고 SIF 광자가 군락으로부터 방출되는 비율 (escape fraction, f_{esc})을 각각 도출하고 탐구하였다. SIF와 GPP의 관계는 뚜렷한 비 선형적인 관계를 보이는 것을 확인했으며($R^2 = 0.91$ with a hyperbolic regression function, daily), 일주기 단위에서 SIF는 APAR에 대해 선형적이었지만 GPP는 APAR에 대해 뚜렷한 포화 관계를 보이는 것을 확인하였다. 추가적으로 LUE_p 와 Φ_F 가 대기 온도에 따라 반응하는 정도가 다른 것을 확인하였다. LUE_p 는 높은 온도에서 포화되었지만, Φ_F 는 포화 패턴을 확인할 수 없었다. 또한, 군락 수준에서의 CCI와 Φ_F 가 뚜렷한 상관 관계를 보였다($R^2 = 0.84$). 이는 Φ_F 가 엽록소 색소에 영향을 LUE_p 에 비해 더 강한 관계가 있을 수 있음을 시사한다. 마지막으로, f_{esc} 가 태양광의 산란된 정도에 따라 반응을 하여, Φ_F 와 LUE_p 의 강한 상관 관계를 형성하는데 기여하는 것을 확인하였다. 이러한 발견은 온대 침엽수림에서 군락 수준의 SIF-GPP관계를 생리학적 및 구조적 측면에서 이해하고 규명하는데 큰 도움이 될 것이다.

식물 계절은 식생이 철을 따라 주기적으로 나타내는 변화를 관측하는 반응이다. 식물 계절은 육상생태계와 대기권 사이의 물질 순환을 이해하는데 매우 중요하다. 위성 기반의 NDVI는 식물 계절을 탐지하고 연구하는데 가장 대중적으로 사용된다. 그러나, 활엽수림에서의 위성 NDVI 기반의 개엽 시기 및 성숙 시기가 실제 어느 시점을 탐지하는지는 불분명하다. 실제 활엽수림은 다층 식생 구조의 삼차원으로 이루어져 있는 반면, 위성 영상은 다층 식생의 신호가 섞여 있는 이차원의 결과물이기 때문이다. 따라서, 위성 NDVI 기반의 식물 계절이 다층 식생 구조를 이루고 있는 활엽수림에서 실제 현장 관측과 비교하였을 때 어느 시점을 탐지하는지에 대한 궁금증이 남는다. 본 학위 논문의 Chapter 4에

서는 지속적으로 8년 동안 활엽수림내의 다층 식생의 식물 계절을 근접 표면 원격 센싱 시스템을 이용하여 관측하고, 위성 NDVI 기반의 식물 계절과 비교하였다. 다채널 분광계를 상부 식생의 위와 아래에 설치함으로써, 상부 식생과 하부 식생의 식물 계절을 각각 연속적으로 관측하였다. 식물 계절을 탐지하기 위하여 가장 많이 사용되는 방법인 1) 역치를 이용하는 방법과 2) 이계도함수를 이용하는 방법을 사용하여 개엽 시기 및 성숙 시기를 계산하고 이를 다층 식생의 식물 계절과 비교하였다. 본 연구 결과, 첫째로, 군락의 상층부에서 실측한 NDVI와 위성 기반의 NDVI가 강한 선형 관계를 보이는 것을 확인했다 ($R^2=0.95$ 는 MODIS 영상들 및 $R^2=0.85$ 는 Landsat8). 둘째로, 이계도함수 방법과 10%의 역치 값을 이용한 방법이 비슷한 개엽 시기를 추정하는 것을 확인하였으며, 하부 식생의 개엽 시기와 비슷한 시기임을 확인하였다. 세번째로, 이계도함수 방법과 90%의 역치 값을 이용한 방법이 비슷한 성숙 시기를 산출하였으며, 이는 상부 식생의 성숙 시기와 비슷하였다. 추가적으로 상부 식생의 개엽 시기와 하부 식생의 개엽 시기가 온도와 반응하는 정도가 뚜렷하게 차이가 나는 것을 확인할 수 있었다. 상부 식생의 개엽 시기는 적산 생장 온도 일수 (AGDD)와 강한 상관성을 보였고, 하부 식생의 개엽 시기는 AGDD와 연관성을 갖고 있을 뿐만 아니라 추위 일수(NCD)에도 민감하게 반응하는 것을 확인하였다. 이러한 결과는 위성 NDVI 기반의 개엽 시기는 하부 식생의 개엽 시기와 연관성이 높고, 성숙 시기는 상부 식생의 성숙 시기와 비슷하다는 것을 의미한다. 또한, 상부 식생과 하부 식생이 온도에 다른 민감성을 갖고 있어, 위성에서 산출된 식물 계절을 이용하여 기후변화를 이해하고자 할 때, 어떤 층의 식생이 위성 영상에 주된 영향을 미치는지 고려해야 한다는 것을 시사한다.

위성은 넓은 지역의 변화를 손쉽게 모니터링할 수 있어 많은 가능성을 갖고 있는 도구이지만, 보다 정확한 위성 관측 값을 이해하기 위해서는 현장에서 관측된 자료를 기반으로 한 검증이 요구된다. 본 학위 논문에서는 1) 근접 표면 센싱 시스템을 개발, 2) 근접 표면 센싱 시스템을 활용한 식생의 생리학적 구조적 변화의 지속적인 관측, 3) 다층 식

생 구조에서 관측되는 식물 계절 및 위성에서 추정된 식물 계절의 연관성 평가를 수행하였다. 개발한 근접 표면 센서는 상업 센서들과 비교했을 때, 가격적으로 저렴하고 손 쉽게 사용할 수 있었으며, 성능적으로도 부족함이 없었다. 근접 표면 센싱 시스템을 이용하여 SIF를 온대 침엽수림에서 지속적으로 관측한 결과, 총일차생산성과 SIF는 비선형 관계를 갖는 것을 확인하였다. 이는 많은 선행 연구들에서 발표한 위성 기반의 SIF와 GPP가 선형적인 관계를 보인다는 것과는 다소 상반된 결과이다. 다층 식생의 봄철 식물 계절을 연속적으로 관측하고, 위성 기반의 식물 계절과 비교·평가한 연구에서는 위성 기반의 개엽 시기는 하부 식생에 영향을 주로 받고, 성숙 시기는 상부 식생의 시기와 비슷한 것을 확인하였다. 즉, 근접 표면 센싱 시스템을 이용하여 현장에서 실측한 결과는 위성 영상을 활용한 연구들과는 다른 결과를 보일 수도 있으며, 위성 영상을 평가 및 이해하는데 사용될 수 있다. 따라서, 보다 정확한 식생의 구조적, 생리학적 메커니즘을 이해하기 위해서는 근접 표면 센싱을 활용한 현장에서 구축한 자료 기반의 더 많은 연구들이 필요하다는 것을 시사한다.

Keyword: 식물 계절, 정규화 식생 지수 (NDVI), 총일차생산성 (GPP), 태양 유도 엽록소 형광물질 (SIF), 근접 표면 원격 센싱 시스템, 위성, 다층 식생, 온대 침엽수림, 온대 활엽수림

Student Number : 2017-39375